5-24-2010

Surface Passivation of Colloidal II-IV Semiconductor Quantum Belts and Quantum Wires: Synthesis, Mechanism and Optical Studies

Yi-Hsin Liu
Washington University in St. Louis

Recommended Citation

Liu, Yi-Hsin, "Surface Passivation of Colloidal II-IV Semiconductor Quantum Belts and Quantum Wires: Synthesis, Mechanism and Optical Studies" (2010). *All Theses and Dissertations (ETDs)*. 851.
https://openscholarship.wustl.edu/etd/851

WASHINGTON UNIVERSITY

Department of Chemistry

Dissertation Examination Committee
William E. Buhro, Chairman
Richard A. Loomis
Sophia E. Hayes
Liviu Mirica
Patrick Gibbons
Daniel Giammer
Viktor Gruev

SURFACE PASSIVATION OF COLLOIDAL II-VI SEMICONDUCTOR QUANTUM BELTS AND QUANTUM WIRES: SYNTHESIS, MECHANISM, AND OPTICAL STUDIES

by

Yi-Hsin Liu

A dissertation presented to the
Graduate School of Arts and Science
of Washington University in
partially fulfillments for the
requirements for the degree
of Doctor of Philosophy

August 2010

Saint Louis, Missouri

ABSTRACT OF THE DISSERTATION

Surface Passivation of Colloidal II-IV Semiconductor Quantum Belts and Quantum Wires:
Synthesis, Mechanism and Optical Studies

By Yi-Hsin Liu

Doctor of Philosophy in Chemistry

Washington University in St. Louis, 2010

Professor William E. Buhro, Chairman

My research aims to study the formation mechanism of CdSe quantum belts (QBs) and the surface passivation of CdTe QW quantum wires (QWs). Investigation of QB morphology and QW passivation are fundamentally important to avoid nonradiative recombination and to increase electron-transport efficiency in semiconductor solar-cell devices. The origin of CdSe QBs is a lamellar structure of cadmium-octylamine precursor complex, with an intermediate state of stripe-like assembly of CdSe magic-sized nanoclusters. Transformation of $(CdSe)_{13}$ nanoclusters to CdSe quantum belts (QBs) is conducted by higher annealing-temperature and confirmed by their optical and structural characterization. The QBs possess a thickness of 1.5-2.0 nm with a width of 7-15 nm and length of >1 μm. Most remarkably, the QBs have a superior morphology with noticeably high quantum efficiency (QE, 30 ± 10 %), comparable to quantum rods. High QE is explained by a delocalized exciton recombination with a lower density of defect sites.

The colloidal CdTe quantum wires (QWs) are preferred for solar-cell applications due to a tunable diameter range (5-60 nm), a long length dimensionality (> 5 μm), and near-IR band-gap emission energy (1.5 eV). Successive surface passivation with Lewis acids and bases successfully passivates the QW surface. A significantly enhanced CdTe QW quantum efficiency (QE, 5-8 %) is achieved, which is two orders of magnitude larger than the previous disappointing QE (< 0.01 %). Enhanced photoluminescence (PL) emission reveals intrinsic higher and lower emission bands for CdTe QWs. Enhanced photoluminescence excitation (PLE) features consistently match previous theoretical calculations for electronic transitions. Significantly high QEs of CdSe QBs (30 ± 10 %) and CdTe QWs (5-8 %) promise colloidal 1D quantum structures suitable for bio-imaging and solar-cell applications.

Acknowledgements

I want to thank all people who directly contribute or support me to accomplish this dissertation and to earn my degree. First, I want to thank my mentor, Professor William E. Buhro, who instructs me to write good scientific papers, revises my dissertation, and helps me to find a postdoctoral position. Under his guidance, I learn how to do research and how to publish scientific results. Professor Richard A. Loomis and Professor Sophia E. Hayes have been my committee members since my second years. I want to thank them for helpful discussions and supports. I want to thanks Professor Patrick C. Gibson and Denial Giammer to read my dissertation and make some corrections and comments. I also want to thank Professor Liviu Mirica and Viktor Gruev to attend my dissertation examination from their busy schedules.

I want to thanks Dr. Fudong Wang (WEB lab) for his help in HRTEM and helpful discussions during my graduate study. I want to thank Ms. Virginia Wayman and Jessica Hoy (RAL lab) for their assists in optical measurement studies which make my research interesting and fruitful. I want to thank other WEB lab mates, especially Dr. Jianwei Sun and Dr. Rui Tang, for their pre-studies of CdTe quantum wire synthesis and CdSe quantum wire surface passivation. I also want to thank other departmental stuffs, especially Dr. Edwin Hiss and Dr. Kit Mao, for their helps in resolving many problems and in teaching training at Washington University.

I also want to thank my roommates and friends met in St. Louis. They are my local my family members who care me, tolerate me, and support me in my every single day. I finally want to thank my parents, sister and brother. They consider my situation and my absence from the family duty. They are also the support to my study in the United States. I will remember the time and the people I meet during these very special years in my life.

Yi-Hsin Liu

August, 2010

Washington University, Saint Louis, MO

TABLE OF CONTENTS

LIST OF FIGURES

Chapter 1: Colloidal Synthesis of Self-Assembled CdSe Nanoclusters in Arrays

Chapter 2: Temperature-Controlled Synthesis of CdSe Quantum Belts

Chapter 3: High Quantum Efficiency and Spectroscopic Studies of CdSe Quantum Belts

Chapter 4: Photoluminescence Enhancement and Spectroscopic Analyses of Surface Passivated CdTe Quantum Wires

LIST OF SCHEMES

Chapter 1: Colloidal Synthesis of Self-Assembled CdSe Nanoclusters in Arrays

Chapter 2: Temperature-controlled Synthesis of CdSe Quantum Belts

Chapter 4: Photoluminescence Enhancement and Spectroscopic Analyses of Surface Passivated CdTe Quantum Wires

LIST OF TABLES

Chapter 4: Photoluminescence Enhancement and Spectroscopic Analyses of Surface Passivated CdTe Quantum Wires

Chapter 1: Colloidal Synthesis of Self-Assembled CdSe Nanoclusters in Arrays

1.1 Introduction

In recent years, significant interest has arisen in molecular-like, magic-sized nanoclusters (diameter of 0.8-2.5 nm) for their strong luminescence[1-2] and ultra-stable and cage-like structures.[3] Due to the ultra-small sizes, the nanocluster dimensions are not easily determined by microscopic techniques. Optical and mass spectroscopies, as alternative techniques, are exclusively applied to resolve the size issue of nanoclusters in terms of confinement energy and mass/charge ratios. Many researchers observe predominant amounts of specific mass/charge ratios indicative of magic numbers that correspond to certain nanoclusters.[4]

The sizes of magic-sized CdSe nanoclusters are usually below 2 nm.[3] Molecule-like CdSe nanoclusters have been made under various conditions.[3-8] Absorption spectra of small-sized CdSe quantum dots (~1.25 nm diameter) were first observed upon pyrolysis of organometallic reagents in a coordinating solvent. [9] These ultra-small CdSe quantum dots covered the size range between 0.7 and 2 nm. [6, 10] Peng and coworkers later predicted stabilized quantum dots in accordance to the Gibbs-Thompson surface energy.[11] According to a surface-energy diagram, two sets of magic-sized numbers, having 29 and 66 atoms, were reported for CdSe nanoclusters.[11]

The sizes of these nanoclusters grow in time at high temperature under synthetic conditions,[10] and they attain magic closed-shell structures due to their surface energy and binding energy.[12] After this theoretical prediction, [11] more and more experimental results supported the existence of the magic-sized nanoclusters by time-of-flight (TOF) mass spectrometry and optical spectra.[4] The stabilized nanoclusters, such as $(CdSe)_{13}$, $(CdSe)_{19}$, $(CdSe)_{33}$ and $(CdSe)_{34}$, have been correlated by their size range to their absorption-wavelength windows.[13]

Magic-sized nanoclusters of similar sizes may be identified by their similar optical signatures. In 2007 and 2008, additional families of stabilized CdSe nanoclusters were made. Ouyang and coworkers reported the excitonic features of magic-sized nanocrystals at 395, 463, and 513 nm, within the size ranges of 1.7-2.2 nm.[1] Nann et al. assigned the absorption feature of 410 nm to $(CdSe)_{33}$ and $(CdSe)_{34}$ (1.4-1.6 nm diameter), and 450 nm to $(CdSe)_{45}$ and $(CdSe)_{56-64}$ (1.8-2.0 diameter).[8] However, the sizes of CdSe nanoclusters are still not precisely determined by HRTEM. A difficulty complicating HRTEM analysis is agglomeration of these nanoclusters.

Agglomeration may or may not affect the confinement energy of CdSe nanoclusters. Riehle et al. studied the superstructures of magic-sized CdSe nanoclusters self-assembled in pyridine.[2] Self-assembly of nanoparticles has also been known as oriented attachment for making small CdS, CdSe and CdTe quantum wires.[14-16] The absorption and emission energies of these ultra-small CdTe quantum wires have been reported to be close to the absorption and emission energies of their precursor nanoclusters.[16]

In this chapter, I will introduce an innovative method for synthesizing CdSe nanoclusters at room temperature. We observe size transitions during growth that shift the excitonic absorption energy. We also observe lamellar assemblies of CdSe nanoclusters and their attachment processes in vertical and lateral directions at elevated temperatures. Our new materials bridge the synthesis between non-emissive CdSe-organic hybrid molecules and colloidal nanostructures, and correlate excitonic features to magic-sized nanoclusters. Further syntheses and optical studies of quantum belts will be discussed in chapters 2 and 3.

1.2 Results

1.2.1 Formation of lamellar $CdX_2(amine)_2$ templates

Lamellar structures were observed in $CdX_2(amine)_2$ complexes.[17] Hyeon and co-workers reported lamellar structures of $CdCl_2(amine)_2$ from reaction of $CdCl_2$ and amines of different chain lengths.[18] In their results, the chain lengths of different amines directly changed spacer distances of the lamellar structures. In my research, I tried to compare the results of different cadmium salts reacting with octylamine. Two cadmium precursors of different crystal structures, $Cd(OAc)_2{\cdot}2H_2O$ and CdI_2, were used to react with octylamine (OA) at ~70 °C for at least 1 h.

In Figure 1.1 (a), two intense diffraction peaks in the XRD pattern of CdI_2 indicated a lamellar structure with slab-to-slab distance of 6.8 Å. After reacting with OA, two emerging series of diffraction peaks were attributed to new spacings. On the basis the averaged spacings from diffraction peaks of higher orders, one spacing was 22.5 ± 0.6 Å and another was 17.2 Å. Similar layer expansion was also observed in $Cd(OAc)_2$. In Figure 1.1 (b), complex diffraction peaks above 12° were due to the low-symmetry $Cd(OAc)_2$ crystal structure. After reacting with OA, low angle (<12°) diffraction peaks emerged corresponding to three other series of slab-to-slab distances. The *d*-spacing for three different distances are 26.1 ± 0.7 Å, 19.5 Å, and 8.67 Å.

The *d*-spacing (d) was composed of a thickness of one inorganic layer (t) and a height of two spacers (h). An observation of two *d*-spacing distances in the XRD patterns implied two different spacer heights (h). Spacer heights were subject to change due to ligand tilting angles (θ) or inter-penetration fraction (η) as variances in eq 1.1.

$$h = [(l + l - l{\cdot}\eta) \sin \theta] = [(2 - \eta)\, l{\cdot} \sin \theta] \qquad \textbf{(1.1)}$$

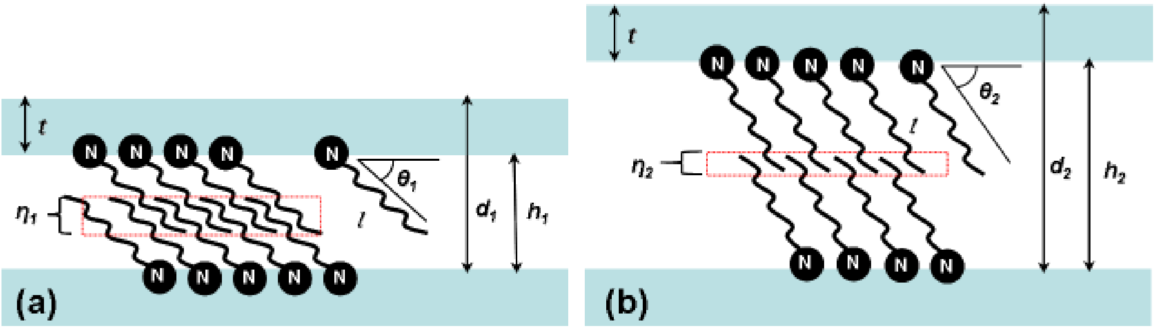

Scheme 1.1 Representation of CdX_2L_2 layer structures with different spacer heights (h). There were two variances: inter-penetration fraction (η) and tilting angle (θ) were used to estimate the spacer height.

In Scheme1.1 (a), one spacer height (h_1) was calculated as 8.0 Å by using OA length (9.7 Å)[19] and estimating θ_1 (30°) and η_1 (0.35). In Scheme 1.1 (b), another spacer height (h_2) was calculated as 14.6 Å by using OA length (9.7 Å) and estimating θ_2 (60°) and η_2 (0.26). Therefore, I proposed that the difference between spacer heights ($h_2 - h_1$, e.g. 14.6 Å – 8.0 Å) was in accordance to the difference between two *d*-spacings (d_1 - d_2, e.g. 26.1 Å – 19.5 Å) experimentally observed in the XRD patterns.

Different cadmium starting materials (CdI_2 and $Cd(OAc)_2$) were used to synthesize lamellar $CdX_2(OA)_2$ complexes. In addition, the lamellar structure was independent of the initial crystal structures of the starting materials. Due to its specific thickness and lamellar morphology, a $CdX_2(OA)_2$ template also served as an excellent host structure and a Cd precursor for magic-sized CdSe nanocluster arrays and subsequently CdSe quantum belts, as shown in this and following chapters.

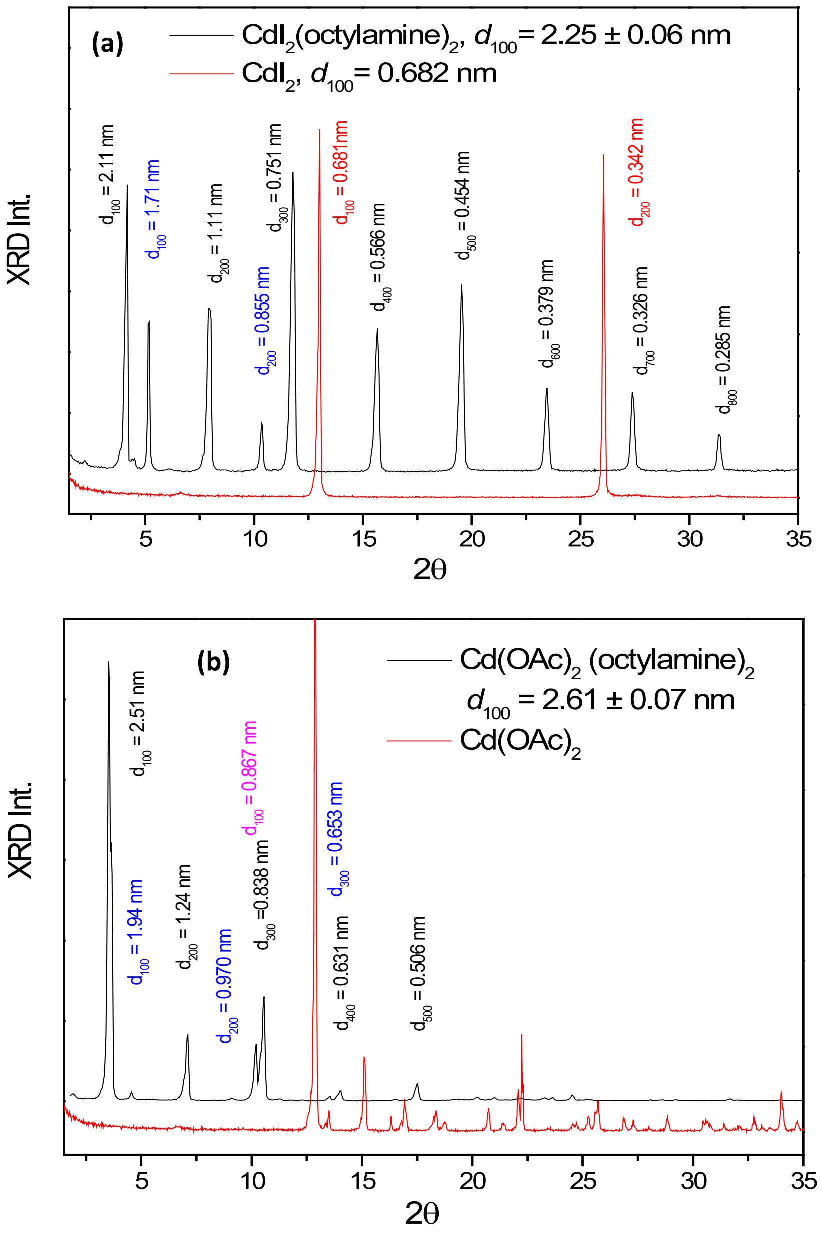

Figure 1.1 XRD patterns of cadmium salt before and after reacting with octylamine. (a) Cadmium iodide (red curve with indices) and cadmium iodide dioctylamine complex (black curve with indices, blue curves of another spacing with indices). (b) Cadmium acetate (red curve with indices) and cadmium acetate dioctylamine complex (black curve with indices, blue and magnate curves of different spacings with indices). Different color indices were used to label different *d*-spacings based on one or more repeating higher-order diffractions.

1.2.2 Synthesis of magic-sized $(CdSe)_n$ clusters

Our synthesis of CdSe nanoclusters used a modified procedure from a previous method for CdSe quantum wires.[20] Solutions for two precursors were separately prepared in the glove box. The cadmium starting material $Cd(OAc)_2(H_2O)_2$ was first dissolved in an appropriate amount of octylamine, and preheated at ~70 °C (1 h). A lamellar-structured $Cd(OAc)_2(OA)_2$ complex was formed upon the appearance of a colorless octylamine solution.

$$\mathrm{Cd(OAc)_2} \xrightarrow[\sim 70\ ^\circ\mathrm{C}\ (>1\ \text{hr.})]{\text{octylamine (OA)}} \xrightarrow[\text{R.T.}\ (>12\ \text{hrs.})]{\text{selenourea in OA}} \xrightarrow[<85\ ^\circ\mathrm{C}\ (1\ \text{hr.})]{\text{annealing}} \mathrm{(CdSe)_{13}} \qquad \mathbf{(1.2)}$$

The Se precursor solution (selenourea in OA) was prepared by dissolving selenourea in octylamine under N_2. A mild sonication was required to effectively dissolve the light-sensitive solid before it decomposed with a color change from colorless (or pink) to dark reddish-brown. The reaction began after an injection of the Se precursor solution into the $Cd(OAc)_2(OA)_2$ solution at room temperature (20-25 °C). After adding the Se precursor solution into the $Cd(OAc)_2(OA)_2$ solution, both the color and appearance were observed to change. The reaction proceeded with anion exchange (acetate to selenide), leading to formation of various sizes of CdSe nanoclusters within the same lamellar structures. The reaction also proceeded with color changes from colorless to orange-yellow, greenish-yellow (cloudy) and yellow (cloudy) mixed with some brown residues during the first hour. The color changes suggested that more than one size of CdSe nanoclusters had been made during the synthesis. After reaction at room temperature for 2 h, four intense peaks were observed in the absorption spectrum with variable initial Se/Cd precursors ratios (1.15-1.76). In Figure 1.2(a), the absorptions at 336, 363, 389, and

413 nm were assigned to (CdSe)$_{13}$, (CdSe)$_{19}$, (CdSe)$_{33}$, and (CdSe)$_{34}$, respectively.[13] Notice that excess selenium from unreacted Se precursor solution significantly interfered with the observation of product color during and after the reaction. Tri-*n*-octylphosphine (TOP) was added into each aliquot taken from the reaction to remove elemental Se prior to spectral measurements. After 2 h, the pale greenish yellow of CdSe nanocluster mixtures were precipitated into the bottom third of the reaction mixture in the presence of the colorless TOP, Se=TOP, and OA solution.

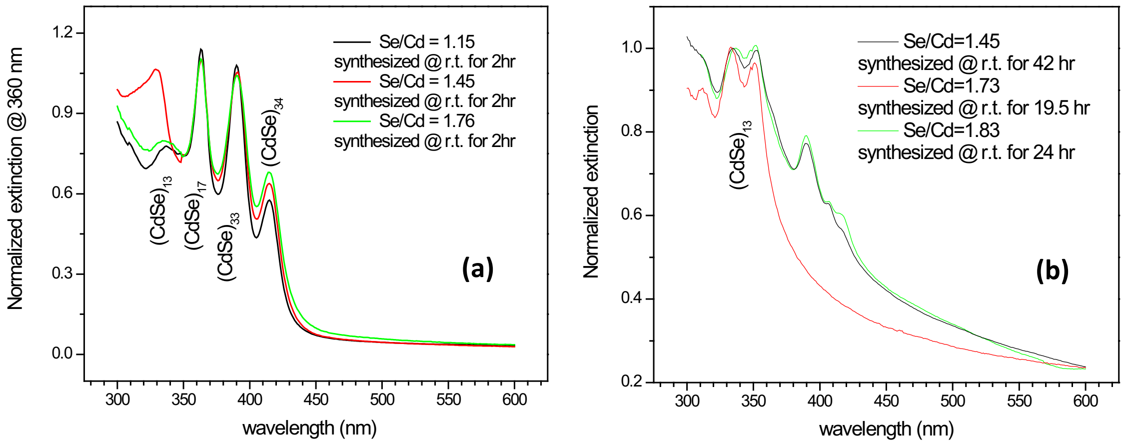

Figure 1.2 Absorption spectra of (CdSe)$_{13\text{-}34}$ nanoclusters. (a) Room temperature reaction (2 h) after the Se-OA solution was injected. (b) Room temperature reaction (20-42 h) after the Se-OA solution was injected.

The CdSe nanocluster mixture (a greenish yellow precipitate) gradually converted to (CdSe)$_{13}$ nanoclusters (a white precipitate) at room temperature. After an extended reaction time (19.5 h), the conversion to spectrally pure (CdSe)$_{13}$ was indicated by the appearance of white precipitate in the colorless TOP, Se=TOP, and OA solution. Absorption features of pure

$(CdSe)_{13}$ nanoclusters are shown in Figure 1.2 (b) as two predominant peaks at 337 and 352 nm (red curve).

In some cases, other magic-sized CdSe nanoclusters still co-existed with the $(CdSe)_{13}$ nanoclusters. An incomplete conversion was indicated by the appearance of a pale greenish white precipitate. The color was due to the absorption of $(CdSe)_{19\text{-}34}$ nanoclusters with minor intensities at 389, 407, and 415 nm (Figure 1.2*b*, black and green curves). Surprisingly, $(CdSe)_{13}$ nanoclusters were the only product made with a recipe of appropriate Se/Cd precursor ratio (1.73) after various extended reaction times (19.5-42 h). Stoichiometry played a more significant role than reaction time to convert CdSe nanocluster mixtures to spectrally pure $(CdSe)_{13}$ nanoclusters.

1.2.3 Purification of magic-sized $(CdSe)_{13}$ nanoclusters

The surfaces of the $(CdSe)_{13}$ nanoclusters were presumably passivated with both octylamine (OA) and tri-*n*-octylphosphine (TOP). Both as-made and annealed $(CdSe)_{13}$ nanoclusters were a white precipitate due to their low solubility, and were properly stored in TOP-OA mixtures under N_2 (in a glove box) for more than a year. Direct dilution of the OA-TOP-capped $(CdSe)_{13}$ nanoclusters afforded a colorless solution or suspension (Figure 1.3 b), depending on the concentration. The diluted $(CdSe)_{13}$ nanoclusters in toluene were also fairly stable prior to a purification process. Repeating a non-alcoholic purification process with toluene and centrifugation (1-2 times) was practically useful for removal of excess organic ligands and preservation of the lamellar structures of the templates (XRD pattern retention). Therefore, alcohol was *not* necessarily used in a generic purification process.

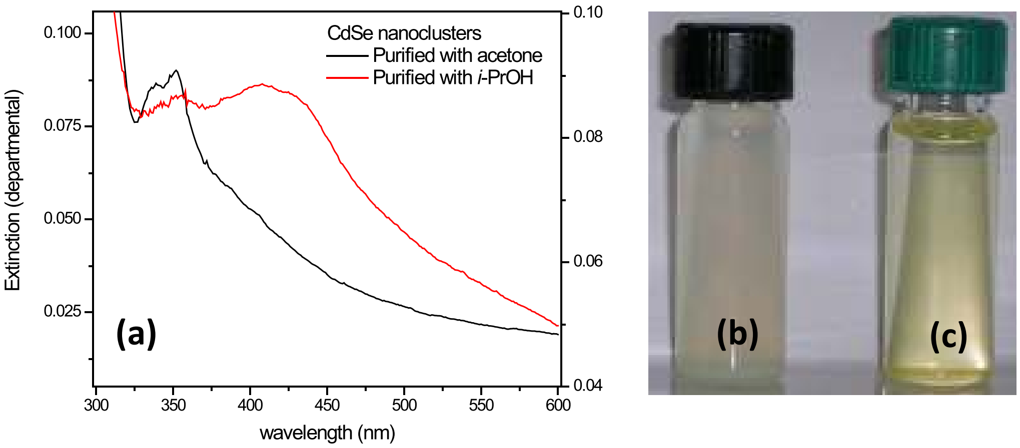

Figure 1.3 Color change of $(CdSe)_{13}$ nanoclusters corresponding to different amounts of polar solvent. (a) Absorption features of annealed $(CdSe)_{13}$ nanoclusters after purification with a very limited amount of acetone (5 drops/mL, black curve) and a little amount of *i*-propanol (20 drops/mL, red curve). Color changes of as-made $(CdSe)_{13}$ nanoclusters dissolved in toluene (white suspension as in *b*) and in large amount of acetone (80/20, v/v in toluene, yellow solution as in *c*).

Even so, a small amount of polar solvent was expected to be useful in flocculating the suspension to allow removal of byproducts and excess ligands after unbundling of $(CdSe)_{13}$ nanoclusters (see below). Methanol has been commonly used in our lab to flocculate colloidal nanostructures in a toluene solution. However, the addition of methanol caused the $(CdSe)_{13}$ nanoclusters to grow, according to the red shifts observed in absorption spectra. To avoid ligand leaching and nanocluster growth, the alternative solvent *i*-propanol or acetone was added into the toluene solution in an appropriate amount (1/20, v/v). In Figure 1.3 (a), a very limited amount of acetone (5 drops/mL solution) was used to flocculate the $(CdSe)_{13}$ nanoclusters while maintaining the appearance of a white suspension and the correct absorption features (black curve). After adding a little more *i*-propanol (20 drops/mL solution) into the $(CdSe)_{13}$ -toluene solution, emerging broad features (red curve in Figure 1.3a) were red-shifted relatively to the original features of $(CdSe)_{13}$ nanoclusters. Such a red shift occasionally occurred as a result of an inappropriate purification indicating further nanocluster growth. Random aggregation or agglomeration occurred when surface ligands were leached during the purification process.

The $(CdSe)_{13}$ nanoclusters were generally unstable in the presence of large amount of polar solvents. In Figure 1.3 (b) and (c), a color change from colorless (in toluene) to yellow (acetone/toluene = 80/20, v/v) also revealed nanocluster growth similar to that shown by the red shift in Figure 1.3 (a). The use of a large quantity of a polar solvent in the purification caused ligand leaching and size growth, and therefore a large quantity of a polar solvent (solvent/toluene > 1/20, v/v) should be avoided.

1.2.4 Annealing of magic-sized $(CdSe)_{13}$ nanoclusters

Annealing at elevated temperature was essential for stabilizing the nanostructures.[20] Prior to the annealing process, the lamellar structures were fragile. After the annealing process, the lamellar structures of $(CdSe)_{13}$ nanoclusters became more uniform by removal of unassigned diffraction peaks at both low and high angles (Figure 1.7a and b). Annealing was required prior to unbundling the lamellar structure to prevent complete disassembly of the template and release of the $(CdSe)_{13}$ nanoclusters.[20] The annealed samples were also more stable to sonication and the presence of polar solvents.

A maximum annealing temperature for $(CdSe)_{13}$ NCAs was 85 °C. The annealing process usually took 1 h with an observation of white precipitates after a TOP injection. However, when the annealing temperature was increased to higher than 85 °C, a transformation began and some $(CdSe)_{13}$ nanoclusters gradually transformed to another nanostructure. In a case of a transformation process at 85-91 °C for 2.7 h, two sharp absorptions and one strong photoluminescence peaks emerged at 423 nm, 445 nm and 450 nm, respectively. The two sharp absorption peaks were characteristic features of the light-hole and heavy-hole electronic transitions in quantum-well structures, such as quantum belts, nanoribbons and nanosheets.[18, 21-22] An observation of mixed absorption peaks indicated an incomplete morphology transformation from (CdSe)$_{13}$ NCAs into transformed CdSe quantum belt (QB) structures.

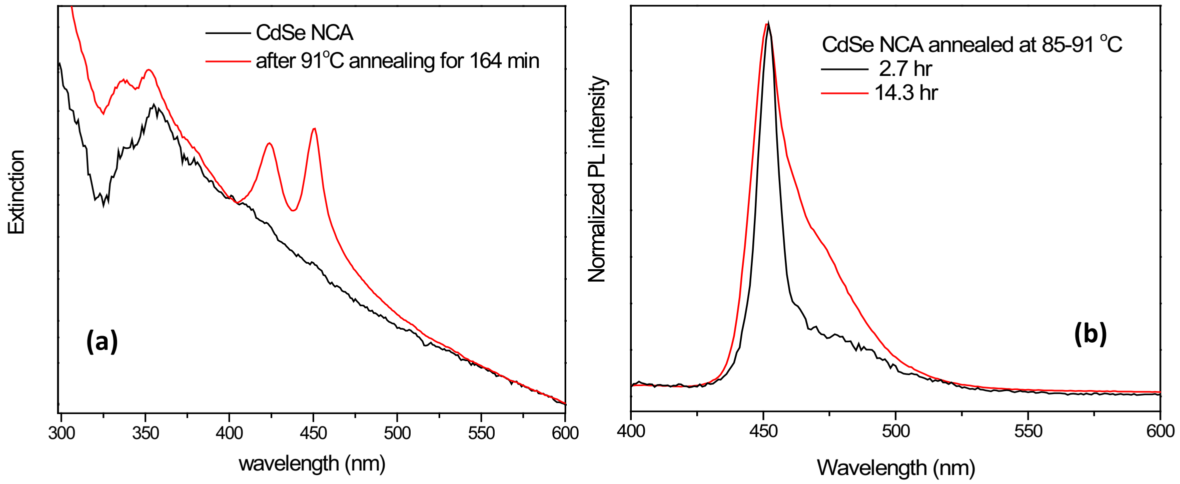

Figure 1.4 Incomplete morphology transformations from (CdSe)$_{13}$ nanoclusters to transformed CdSe QBs at lower temperature (85-91 °C). (a) Monitoring the (CdSe)$_{13}$ nanoclusters absorption at room temperature before (black curve) and after (red curve) transformation at 91 °C for 2.7 hours. (b) PL spectra of (CdSe)$_{13}$ nanoclusters transformed at 85-91 °C for 2.7 hour (black curve) and 14.3 hours (red curve), respectively.

Photoluminescence (PL) and photoluminescence excitation (PLE) spectroscopies were also employed to investigate both emission and the band-edge excitation of quantum-well structures. In Figure 1.4 (b), emission features of the transformed CdSe QB were very similar to the emission peaks of the directly synthesized CdSe QBs (1.5-2.0 nm, see Chapter 2). After transformation processes for various times (2.7 h and 14.3 h), there was no significant shift in PL emission wavelength. However, a longer transformation time (14.3 h, red curve) yielded larger proportions in longer wavelength emission (450-500 nm) than shorter transformation time (2.7 h, black curve) did. A similar phenomenon was also observed during the synthesis of CdSe QBs. The transformation time might be related to the bundling of CdSe QBs, but has not been resolved.

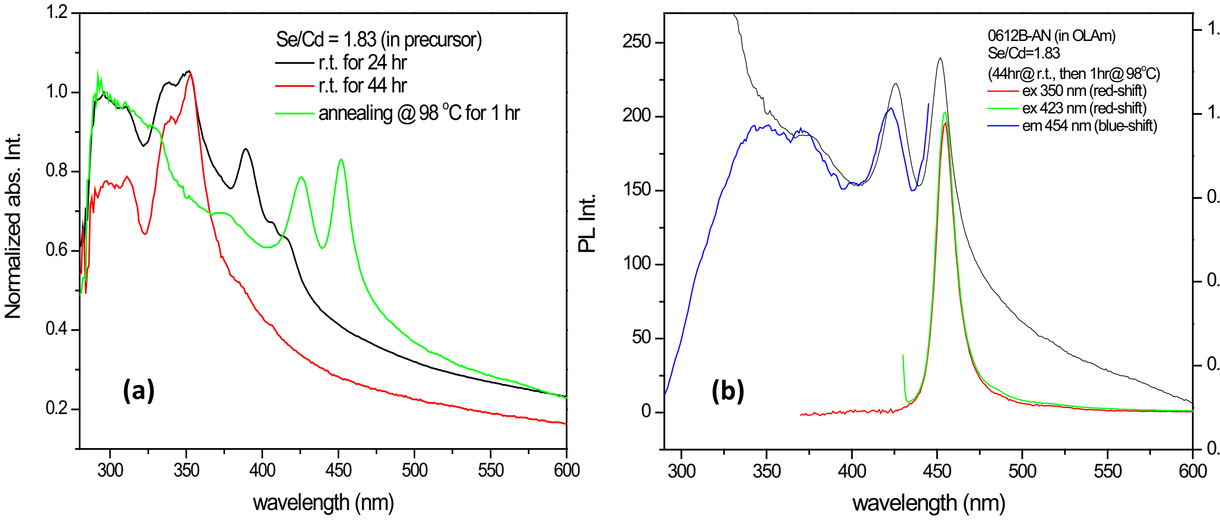

Figure 1.5 Complete morphology transformations from $(CdSe)_{13\text{-}19}$ nanoclusters to CdSe QBs at higher temperature (> 98 °C). (a) Monitoring $(CdSe)_{13\text{-}19}$ nanocluster absorption features before (black and red curves) and after 98 °C transformation (green curve). (b) Absorption (black curve), PL spectra (red and green curves) and PLE (blue curves) of the transformed CdSe QBs.

Another comprehensive morphology transformation from $(CdSe)_{13}$ nanoclusters to CdSe QBs was conducted at a higher annealing temperature (> 98 °C). In addition, the absorption, PL and PLE spectra of these transformed CdSe QBs matched those spectra of directly synthesized CdSe QBs.[23] In Figure 1.5 (a), the absorption peaks $(CdSe)_{13}$ quickly disappeared (red curve to green curve) after 1 h of transformation at 98 °C in the original solution. Three absorption features at 445, 423 and 378 nm were identified as the features of the CdSe QBs. In Figure 1.5 (b), photoluminescence excitation (PLE) spectra systematically matched the second and the third features to its absorption peaks with small blue shifts. PL emission was investigated with two excitation wavelengths at 350 and 423 nm, corresponding to the absorption of $(CdSe)_{13}$ nanoclusters and the heavy-hole transition of CdSe QBs. Peak shifting was *not* observed between these two PL emissions, except for some intensity variation. Optical characterization therefore confirmed a transformation from $(CdSe)_{13}$ NCAs to CdSe QBs after a transformation process at higher temperature (> 98 °C).

Transmission electron microscopy (TEM) provided an evidence to directly observe the morphology transformation. The images of as-made bundled CdSe NCAs and transformed CdSe QBs were compared in Figure 1.6. The multiple solid lines in Figure 1.6 (a) revealed the thickness of the as-made layer bundled $(CdSe)_{13}$ NCAs from a side view. Averaged layer-to-layer distance (*d*-spacing) was measured as 3.9 ± 0.5 nm and the thickness was 1.7 ± 0.3 nm in Figure 1.6 (a). The spacer height (h) was therefore calculated as 2.2 ± 0.7 nm (3.9 – 1.7 nm) in purified $(CdSe)_{13}$ nanoclusters. This spacer height (2.2 nm) was slightly larger than the distance assumed in both bilayer models in Scheme 1.1. The tilting angle (θ) and inter-penetration degree (η) both may significantly change the *d*-spacing (d) and spacer height (h). To prepare this TEM grid, the sample must be carefully purified with minimal amount of acetone or *i*-propanol (solvent/toluene < 1/20, v/v) to avoid collapse or unbundling of lamellar structures. Difficulty in focusing such images was caused by the residual OA and TOP present.

An annealing process at 91 °C expedited stripe attachment in the original octylamine solution. The attachment mechanism was initiated by the head-to-tail attachment along the stripes' longest dimension (*c*-axis), resulting in a belt shape. After annealing for 1.2 h (74 min), tangled belt-shape CdSe nanostructures were observed under TEM with an estimated length of at least 1.0 μm (Figure 1.6 b). Such long-axis attachment was previously observed in synthesizing colloidal nanorods, nanowires and twist ribbons of cadmium-chalcogen semiconductors.[14-16] Representative TEM images of intermediate products and the final belt morphology successfully supported the spectroscopic observation of the nanocluster-to-belts formation pathway.

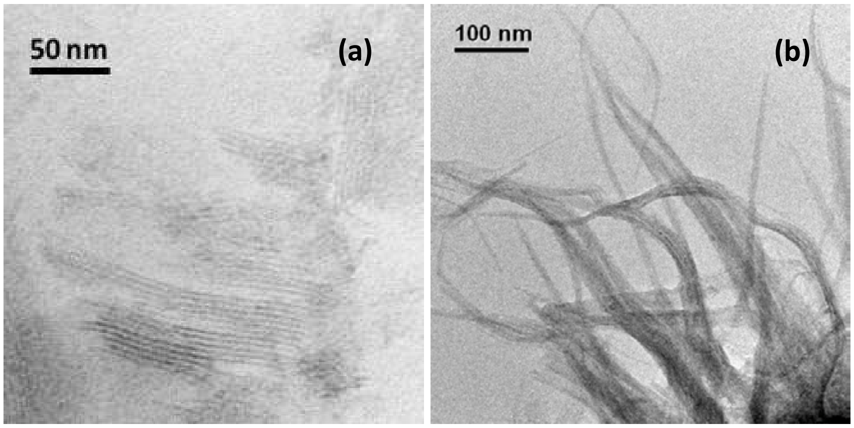

Figure 1.6 (a) A representative TEM images of as-made $(CdSe)_{13}$ nanocluster arrays (NCAs, made at room temperature). (b) A representative TEM images of transformed CdSe QBs from annealing $(CdSe)_{13}$ NCAs at 91 °C.

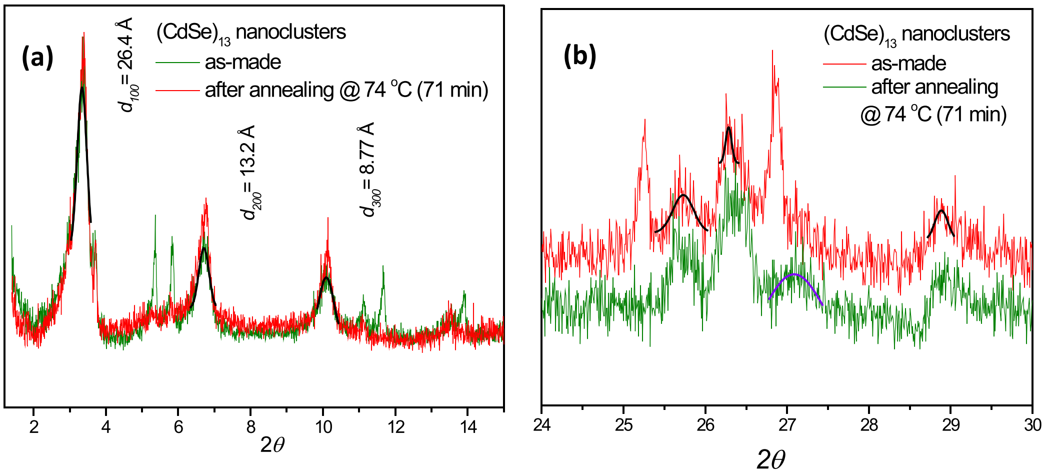

Figure 1.7 XRD patterns of CdSe nanoclusters before and after the annealing process. (a) Low-angle diffraction peaks indicated lamellar structures in both as-made and annealed $(CdSe)_{13}$

nanoclusters. (b) High-angle peaks due to diffraction from the $(CdSe)_{13}$ clusters. The full width at half maximum (FWHM) was fitted with a Gaussian profile in a bold black curve.

X-ray diffraction (XRD) also confirmed lamellar structures of $(CdSe)_{13}$ nanoclusters before and after annealing. In Figure 1.7, the $(CdSe)_{13}$ nanoclusters showed no significant difference in layer-to-layer *d*-spacings before and after annealing at 71 °C for 74 min. Several narrow diffraction peaks (unfitted green spikes) in Figure 1.7 (a) and (b) disappeared after the annealing process. According to the calculated *d*-spacing (27 ± 2 Å) from XRD and the measured thickness (17 ± 3 Å) from TEM, the spacer distance (OA and TOP) between two layers was calculated as 10 ± 5 Å (27 – 17 Å) in as-made $(CdSe)_{13}$ nanoclusters. This distance was close to the spacer height (8 Å) in bilayer model assumed in Scheme 1.1 (a).

Therefore the TEM and XRD measurements gave different spacer heights, of 2.2 ± 0.7 nm and 1.0 ± 0.5 nm, respectively. These values were experimentally distinguishable in consideration of the errors in the measurements. I speculated that the difference in spacer height is due to the different sample preparation procedures used in the two methods. The TEM sample preparation required washing with *i*-PrOH or acetone to remove sufficient organic residues to produce resolved images. XRD sample preparation required only washing with toluene, which is less disruptive to the lamellar structures. Consequently, different inter-penetration degree (η) and/or tilting angle (θ) could have resulted from two treatments, leading to the different spacer height (h).

The annealing temperature also determined the completeness of the morphological and crystallographic transformation. As shown in Figure 1.8 (b), with an annealing temperature of 98 °C, the $(CdSe)_{13}$ nanoclusters were completely transformed to CdSe QBs. Higher-angle diffraction peaks between 20-30 °C indicated a wurtzite structure for the transformed CdSe QBs.

Due to the lamellar nature of the original $(CdSe)_{13}$ NCAs , the transformed CdSe QBs persistently gave a series of low-angle diffraction peaks for a lamellar structure. In Figure 1.8 (a), the *d*-spacing (29 Å) was calculated to be 7% larger than the *d*-spacing (27 Å) in the $(CdSe)_{13}$ NCAs. Such a layer increment was explained by both layer thickness and a spacer expansion. The assumption of layer thickness expansion was based on significant lattice relaxation from a strained nanocluster to a less strained QB (2.8-4.7 % in Figure 1.8b) in the wurtzite QBs. The assumption of spacer expansion was based on ligand re-alignment after annealing, which was subject to change the tilting angle (θ) and inter-penetration degree (η).

For the transformed QBs, the first two low-angle diffraction peaks gave an estimated diffraction coherence length (l) of 15 nm as calculated from the Scherrer equation. This value (15 nm) reflected coherence in the layer-to-layer stacking dimension normal to the layers. In comparison to the interlayer *d*-spacing of 2.93 nm, the l value corresponded to coherence over 5 to 6 layers of the transformed QBs.

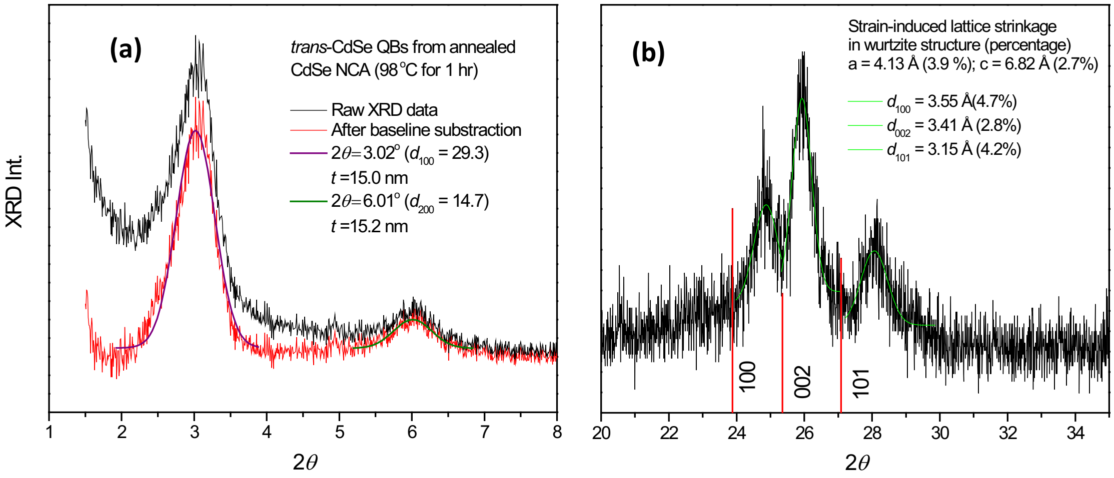

Figure 1.8 XRD patterns of transformed CdSe QBs from annealed CdSe NCAs at 98 °C. (a) Low-angle diffraction peaks indicated preservation of lamellar structures. Calculations from the Scherrer equation indicated that the coherence length (l) of the QBs was 15 nm, based on the FWHM of the first two peaks (purple and green curves) fitted with Gaussian profiles. (b) High-

angle peaks clearly indicated the strained wurtzite structure (red lines) after annealing, with lattice contraction of 2.8 – 4.7 %.

The transformation process was mainly controlled by annealing temperature, rather than by annealing time. The morphology and optical property-changes (NCA→ transformed QB), crystal-structure transformation (molecular → wurtzite, strained → less strained), and lamellar-structure retention (low-angle diffraction) reveal a topotactic structural transformation in which a substantial structural reorganization occurs while significant orientational relationships are preserved.

1.2.5 Unbundling of magic-sized $(CdSe)_{13}$ nanoclusters

After annealing up to 85 °C, $(CdSe)_{13}$ nanoclusters were chemically and structurally stable in the lamellar octylamine templates. In the presence of oleylamine, ligand exchange occurred spontaneously even at room temperature. In Figure 1.9, $(CdSe)_{13}$ nanoclusters maintained their absorption features after ligand exchange (10-12 h) and a sonication process (20-40 min) in oleylamine-toluene solution (10 %, w/w). Sonication did not significantly change the 1st absorption feature (350 nm), but caused a small red shift to the 2nd absorption feature (328 → 335 nm). A reduced extinction intensity of scattered-light tail at longer wavelengths (> 350 nm) was an indication of decreasing nanostructure dimensions. On the basis of the above two evidences, the $(CdSe)_{13}$ nanoclusters still maintained their original quantum-confinement properties, but a disruption of lamellar stacking after ligand exchange and sonication in oleylamine occurred.

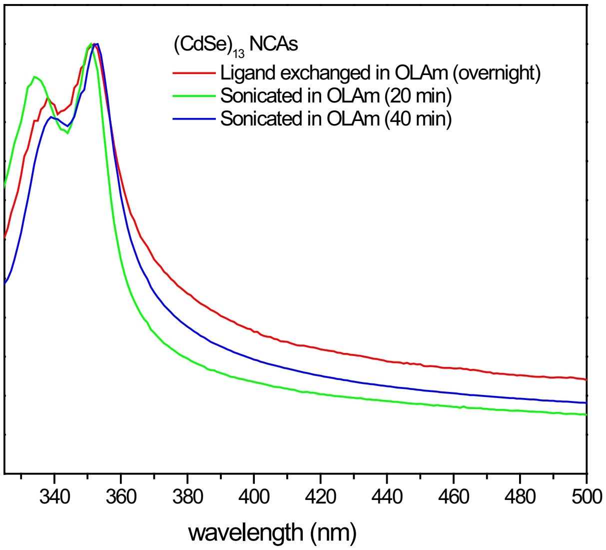

Figure 1.9 Absorption features of annealed $(CdSe)_{13}$ nanoclusters before and after sonication. (red curve) Ligand-exchanged $(CdSe)_{13}$ nanoclusters in oleylamine (OLAm)-toluene solution before sonication. Ligand exchanged $(CdSe)_{13}$ nanoclusters after sonication in oleylamine-toluene solution for 20 min (green curve) and 40 min(blue curve). The intensity was normalized to its peak maxima around 350 nm. Reduced baseline intensity at the longer wavelength indicated less scattering from the OLAm-exchanged $(CdSe)_{13}$ nanoclusters.

Furthermore, after sonication of NCAs in oleylamine solution, lamellar structures were no longer detected in TEM images. When the NCAs were not annealed prior to ligand exchange, the lamellar structures were apparently fully disassembled, leading to release of the $(CdSe)_{13}$ clusters. These free clusters are too small to be imaged by TEM. When the NCAs were annealed prior to ligand exchange, a layer unbundling occurred, leading to individual template sheets entrapping the $(CdSe)_{13}$ clusters (see below).

During the ligand exchange, the oleylamine (spacer) increased the layer-to-layer distance, which led to a gradual unbundling. With assisance of sonication, the unbundling process was expedited in 5-11 min. The ligand exchange caused a small angle shift to larger *d*-spacing, in the comparison original XRD patterns, for the residual lamellar nanostructures. In Figure 1.10, a layer-to-layer distance of 24.5 Å (t_0) in as-made CdSe NCAs, gradually increased to 37.9 Å after ligand exchange with oleylamine, and further increased to 46.4 (t*) and 45.7 Å after sonication for 20 and 40 min, respectively. The spacer incremental increase after sonication was around 2.19 nm (4.64 nm - 2.45 nm) along the interlayer direction.

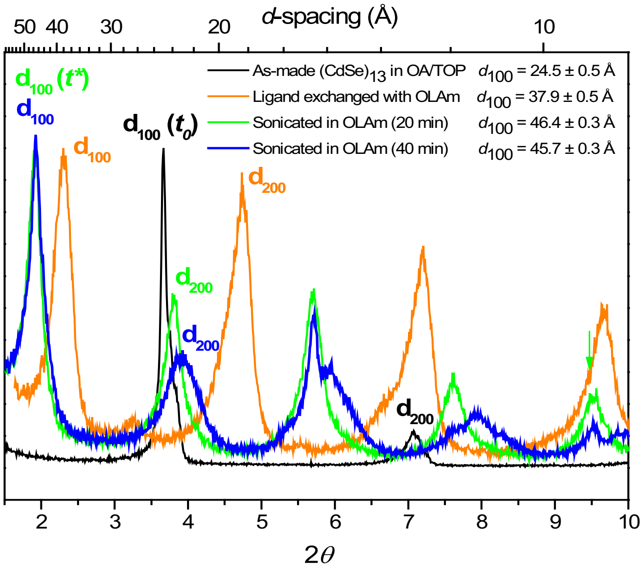

Figure 1.10 Low-angle XRD of NCAs during unbundling. As-made $(CdSe)_{13}$ NCAs precipitated from a octylamine solution with tri-n-octylphosphine (black curve). Ligand-exchanged $(CdSe)_{13}$ NCAs precipitated from a oleylamine-toluene solution (orange curve). $CdSe)_{13}$ NCAs sonicated in a oleylamine-toluene solution for 20 min (green curve). $(CdSe)_{13}$ NCAs sonicated in a oleylamine-toluene solution for 40 min (blue curve).

In addition, the low-angle reflection FWHM of as-made $(CdSe)_{13}$ nanoclusters was noticeably smaller than the FWHM after ligand exchange. According to the Scherrer equation, a sharper diffraction peak corresponded to a larger dimension for the nanostructures, while a broader diffraction to a smaller dimension. A similar conclusion was also made in the absorption spectrum from the decreasing baseline extinction (Figure 1.9).

Transmission electron microscopy (TEM) was used to reveal the morphology of unbundled $(CdSe)_{13}$ NCAs. In bundled forms, the NCAs exhibited parallel patterns orthogonal to the layer-stacking direction. Very limited information was obtained from TEM images of the bundled $(CdSe)_{13}$ NCA. Triangle shapes were most commonly observed in annealed $(CdSe)_{13}$ NCAs after unbundling. These images were very similar to the morphology of CdTe nano-sheets reported by Hyeon *et al.*[18] However, the triangle shapes were composed of several individual stripes of nanoclusters. The data suggested that the sheet-like structures contained one to a few layers that were exfoliated from the original bundled NCAs. The stripe patterns evident in the individual layers indicated that the bundled NCAs actually possessed double lamellar structures.

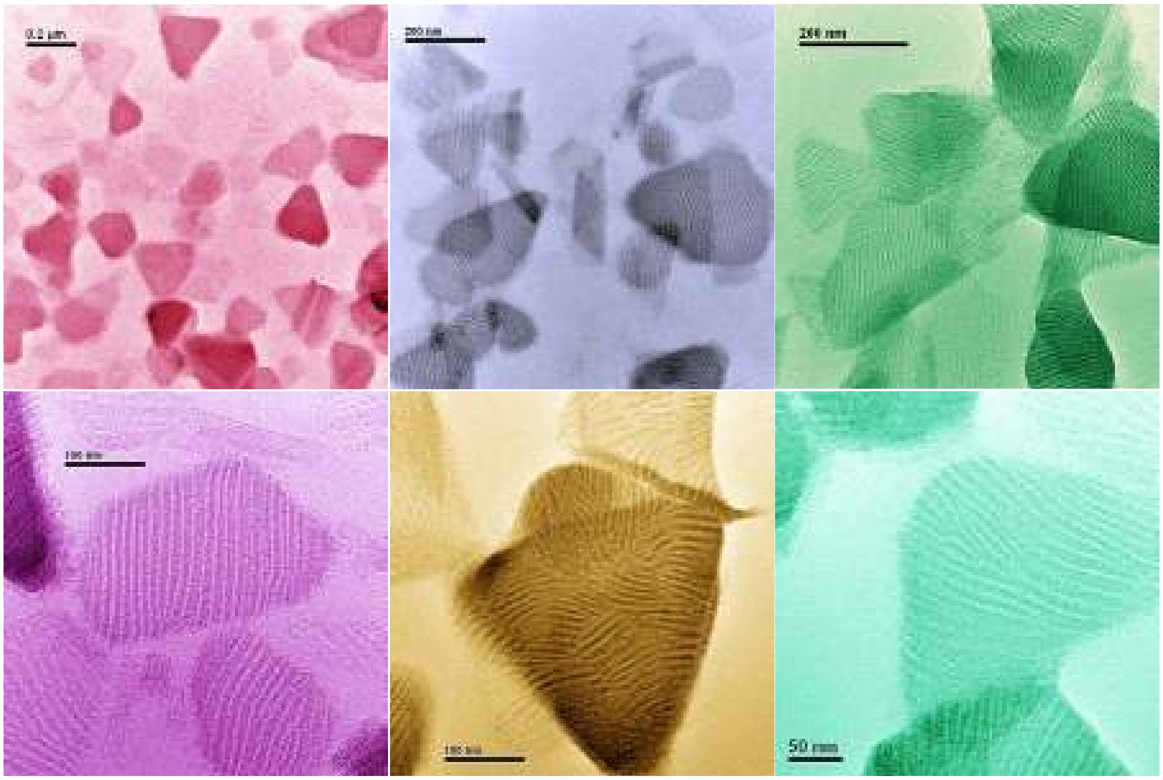

Figure 1.11 Representatives TEM images of $(CdSe)_{13}$ NCAs after unbundling. These $(CdSe)_{13}$ clusters were originally assembled into stripe stacking horizontally (side-by-side) and vertically (layer-by-layer). After unbundling, most $(CdSe)_{13}$ stripes still laid horizontally (side-by-side) in irregular nanosheets.

After the unbundling process, most of the $(CdSe)_{13}$ NCAs were still laying together in side-by-side stripes, as a pseudo-1D lamellar structure. In Figure 1.11, partial or full unbundling resulted in parallel stripes with wide faces laid upon the TEM grids horizontally. Full unbundling was evidenced by the disappearance of vertical stacking along the thickness direction for some of the sheet-like structures. However, horizontal stacking along the width direction was still maintained. At lower magnification, a single stack or a few stacks could be distinguished by image darkness. At higher magnification, multiple stripes were individually resolved in irregular or triangle shapes. The stripe thickness was 1.7 ± 0.3 nm (Figure 1.6a), the strip widths were usually 4-12 nm (Figure 1.12), and the stripe lengths were less than 200 nm (Figure 1.12). To prepare these TEM grids (Figure 1.12), two aliquots of as-made CdSe NCAs were sonicated in oleylamine for 5 min (partial unbundling) and 11 min (full unbundling), and then purified with an acetone-toluene mixture (1/20, v/v).

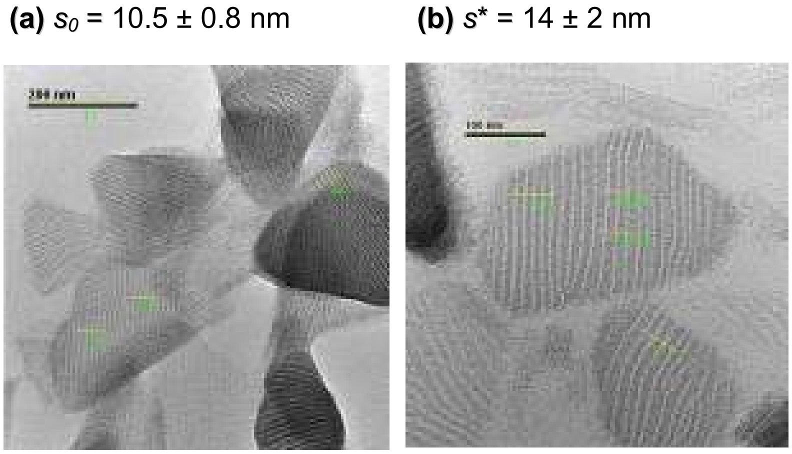
(a) $s_0 = 10.5 \pm 0.8$ nm **(b)** $s^* = 14 \pm 2$ nm

Figure 1.12 Spacer expansion of $(CdSe)_{13}$ nanocluster stripes in oleylamine-toluene solutions. The distances between two adjacent stripes were 10.5 ± 0.5 nm (s_0) in an early stage of unbundling (sonication for 5 min, *a*) and 14 ± 2 nm (s^*) after total unbundling (sonication for 11 min, *b*).

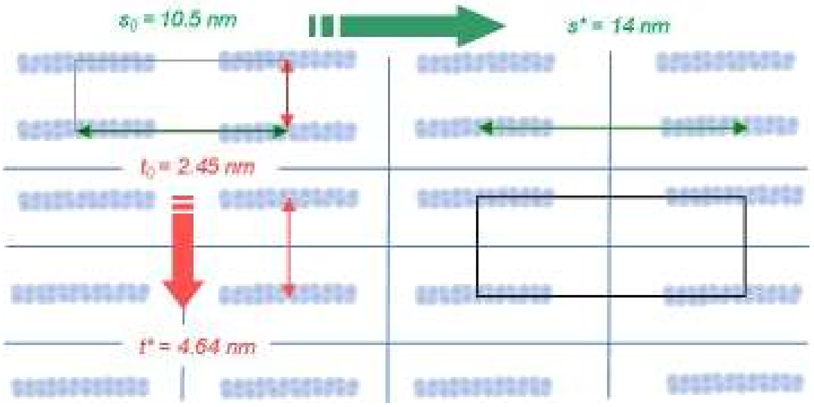

Scheme 1.2 A schematic of spacer expansions of double-lamellar CdSe NCAs in oleylamine solution. Vertical expansion (red arrows, $t_0 \rightarrow t^*$) was observed by XRD (Figure 1.10). Horizontal expansion (green arrows, $s_0 \rightarrow s^*$) was observed by TEM. The black boxes are to highlight the expansion in two dimensions.

Both vertical and horizontal expansions were observed during the unbundling process. A vertical expansion was resolved by a *d*-spacing increment of 2.19 nm (4.64 nm → 2.45 nm) from low-angle XRD data (Figure 1.10). A horizontal expansion was measured by an increment of 3.5 nm (14 nm →10.5 nm) from the TEM images taken during the unbundling process (Figure 1.12a and b). Both expansion results by XRD and TEM reveal the existence of the double-layer lamellar structure for CdSe NCAs in Scheme 1.2. Both vertical (red arrow) and horizontal expansions (green arrow) indicated a 2D ligand exchange and expansion processes with oleylamine. The expansion occurred simultaneously during the ligand exchange. The maximum vertical expansion observed by TEM was approximately of 4.64 nm. Beyond this distance, the spacers (oleylamine) no longer held the CdSe NCA slabs and the lamellar structure was disrupted. As a result of this unbundling process, CdSe NCAs were dissociated into individual layers or sheets, and lateral stripes were observed in the TEM image (Figure 1.12b).

Unbundling was an extremely useful strategy to reveal the two different dimensions of lamellar structure (thickness by XRD and width by TEM images) as well as to reveal reduced bundle sizes (FWHM in XRD patterns and scattering baseline in absorption). In addition, the lack of significant changes for the $(CdSe)_{13}$ nanocluster optical properties during the unbundling process indicated a preservation of quantum confinement, size, and electronic structure in the presence of oleylamine. According to a reduced bundling size and the similar optical properties, a molecule-like $(CdSe)_{13}$ nanocluster might be completely released from the templates after a *vigorous* sonication. These results constitute multiple innovative steps for the synthesis, annealing, purification, and unbundling processes to obtain stabilized $(CdSe)_{13}$ nanoclusters of the smallest sizes ever reported.

1.3 Discussion

1.3.1 Advances in the synthesis of CdSe Nanoclusters

Small CdSe nanoclusters have been temporarily observed as intermediates during CdSe nanoparticle synthesis.[10] Various ligands (L), such as amines, thiols, phosphines, and phosphonic acids, were used as ligands in traditional syntheses. Interestingly, the atom numbers of Cd (x) and Se (y) in a generic nanocluster formula, $[Cd_xSe_yL_z]^{n-}$, are not necessarily equivalent. An example CdSe nanocluster formula is $[Cd_{32}Se_{14}(SePh)_{36}(PPh)_4]$.[5]

For traditional syntheses of CdSe nanoclusters, both reaction temperature and time play significant roles on size growth.[24] Nanocluster growth depends on total energy (E_{tot}), including surface energy (E_{sur}) and binding energy (E_{bin}). In the literature, an existence of "magic-sized" clusters is predicted by a local minimized total energy[11] or a local maximized binding energy.[4] When nanoclusters become smaller, surface energy dominates total energy (E_{tot}) due to increasing surface areas (E_{sur}). Therefore, most small nanoclusters are unstable with very short lifetime (a few minutes),[10] until additional binding energy (E_{bin}) further stabilizes the meta-stable structures. An ultra small CdSe nanoparticle (~12 Å) has been synthesized since 1993 but its total energy was not been calculated until 2002 by Peng and coworkers.[11] According to the surface-energy diagram, two meta-stable nanoclusters were predicted. The magic numbers of the *total atoms* in the meta-stable CdSe nanoclusters were around 29 and 66.[11] These magic numbers are close to $(CdSe)_{13}$ and $(CdSe)_{33\text{-}34}$, respectively.

Meta-stable nanoclusters, such as $(CdSe)_{13}$, $(CdSe)_{19}$, $(CdSe)_{33}$, and $(CdSe)_{34}$, known as magic-sized ones, have been identified by time-of-flight (TOF) mass spectra with assigned optical absorption.[4] Theoretical structures and electronic spectra of $(CdSe)_{13}$ and $(CdSe)_{33\text{-}34}$ nanoclusters were also computed by density function theory (DFT).[25-26] Unfortunately, none of these nanoclusters can be individually made or successfully isolated from a mixture of different-sized nanoclusters without undergoing a significant spectral change.[10]

Herein we report an innovative strategy for synthesizing spectrally pure $(CdSe)_{13}$ nanoclusters. There are a few important criteria met in this synthesis for the formation of stable $(CdSe)_{13}$ nanoclusters. First, the reaction temperature is relatively low, at room temperature (20-25 °C), which leads to a slow reaction rate and prevents uncontrolled nanocluster growth. Second, a more reactive selenium precursor (selenourea) replaces the traditional Se-TBP or Se-TOP, which require high temperature to initiate the reaction. Third, an *n*-octylamine (*n*-OA) is used as a solvent and reactant. A high concentration amine solution thoroughly confines all nanoclusters inside the lamellar templates. Of the most importance, the ligated $(CdSe)_{13}$ nanoclusters can be synthesized in a large quantity with high stability under ambient conditions.

There are three structures of $(CdSe)_{13}$ nanoclusters proposed by different groups. A caged structure was first reported by Kasuya and co-workers.[4] In Figure 1.13 (a), there were 12 equivalent Se atoms on the surface and one unique Se atom inside the core structure. This near-spherical cage structure possibly minimizes surface energy (E_{suf}) which reduces the total energy (E_{tot}). In 2006, another flattened structure was proposed by Jose and coworkers. In Figure 1.13 (b), there were four different types of Se (or Cd) atoms in the structure.[25] Atom numbers of different environment of Se (or Cd) were in a ratio of 1:3:6:3, alternatively up-and-down positioned from a center of three fused hexagons. Most recently, a similar hexagon-based structure was also computed by Chung and coworkers and shown in Figure 1.13 (c).[27] A C_{3v} symmetry was accordingly assigned to this wurtzite-like structure. Further characterizations, such as ^{113}Cd or ^{77}Se NMR and infra-red spectroscopy, may be useful in distinguishing among these three proposed structures.

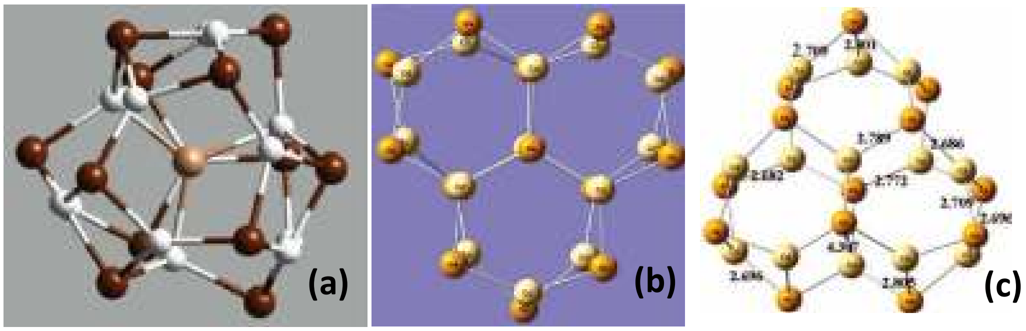

Figure 1.13 Three proposed structures of $(CdSe)_{13}$ nanoclusters. (a) A twist caged structure of $(CdSe)_{13}$ nanocluster with a Se (light brown) inside the core.[4] (b) A bilayer geometry of $(CdSe)_{13}$ nanocluster.[25] (c) Another bilayer geometry of $(CdSe)_{13}$ nanocluster with C_{3V} symmetry.[27]

Microscopic techniques, such as TEM, cannot directly identify each $(CdSe)_{13}$ nanocluster. Issues of intrinsic agglomeration and anisotropic shapes produce diameter uncertainty for the $(CdSe)_{13}$ nanoclusters. Spectroscopic tools, on the contrary, are more powerful for assigning different nanoclusters even in aggregation. In the following discussion, I will use spectroscopic data to correlate with reported diameters and magic numbers of various sized nanoclusters (diameter < 2.5 nm). Other interesting phenomena, such as self-assembly of CdSe nanoclusters, will be compared to correlate the lamellar structures to quantum-belt structures after annealing.

1.3.2 Magic Numbers in CdSe Nanoclusters

Magic numbers (n) were defined in stabilized $(CdSe)_n$ nanoclusters. Existence of various nanoclusters, such as $(CdSe)_{13}$, $(CdSe)_{19}$, $(CdSe)_{33}$ and $(CdSe)_{34}$, indicates that only specific magic numbers of (CdSe) fragments lead to stable nanostructures. Stable organometallic compounds have been predicted by Wade's rules in which skeletal electron pairs (SEP) are used to explain possible polyhedral structures.[28] Similarly, magic numbers (n) of $(CdSe)_n$ may perhaps determine total skeletal electron pairs in nanoclusters which lead to stabilized CdSe nanostructures.

Theoretical results successfully predict different magic numbers of CdSe nanoclusters. According to Kasuya et al, the $(CdSe)_5$ or $(CdSe)_6$ fragment is a basic building unit of skeletal electron pairs.[4] The fragments can link into a three-dimensional network, such as a highly symmetric $(CdSe)_{28}$-cages analogous to fullerenes. According to the spaces in the core, the $(CdSe)_{28}$-cages can accommodate at most seven pairs of (CdSe) fragments. In addition, a binding-energy calculation also leads to two most-stable nanoclusters of magic number 33 and 34.[4] The first introduction of the internal (CdSe) fragment decreased the Cd-Se binding energy due to the repulsion from an additional pair of skeleton electrons. On the contrary, a following five introductions progressively increased the binding energy until a formation of $(CdSe)_{34}$ nanoclusters. After the 7th introduction of (CdSe) pair into the core, the binding energy decreased again which implies a fully occupied cage structure with a large electron repulsion. According to this trend, 33 and 34 are the magic numbers with larger binding energies and more stabilized structures than numbers of 28-32 and 35. This also implies that the stabilized structures of $(CdSe)_{33}$-$_{34}$ are the predominate populations in the TOF-MASS spectrum.[4, 8, 10] Kasuya et al were the first and only group who used the binding energies of $(CdSe)_{28\text{-}34}$ to systematically investigate the effect of filling (CdSe) fragments into the cage-like structure.

Experimental results also confirm an existence of specific CdSe nanoclusters with magic numbers. In Figure 1.14, Cd atom numbers (n) of various CdSe nanoclusters from the literature are plotted with their sizes (or diameters in left y-axis, black curve) and absorption wavelengths (in right y-axis, red curve).[13] According to the curvature changes, different slopes are accordingly assigned to five regimes. Slope change at a regime boundary coincidentally meets the magic numbers (n) of 13, 31, 34 and 66. Two of these numbers also closely match to the magic-sized CdSe nanoclusters ($2n$ = 29 and 66) previously predicted by Peng et al.[11]

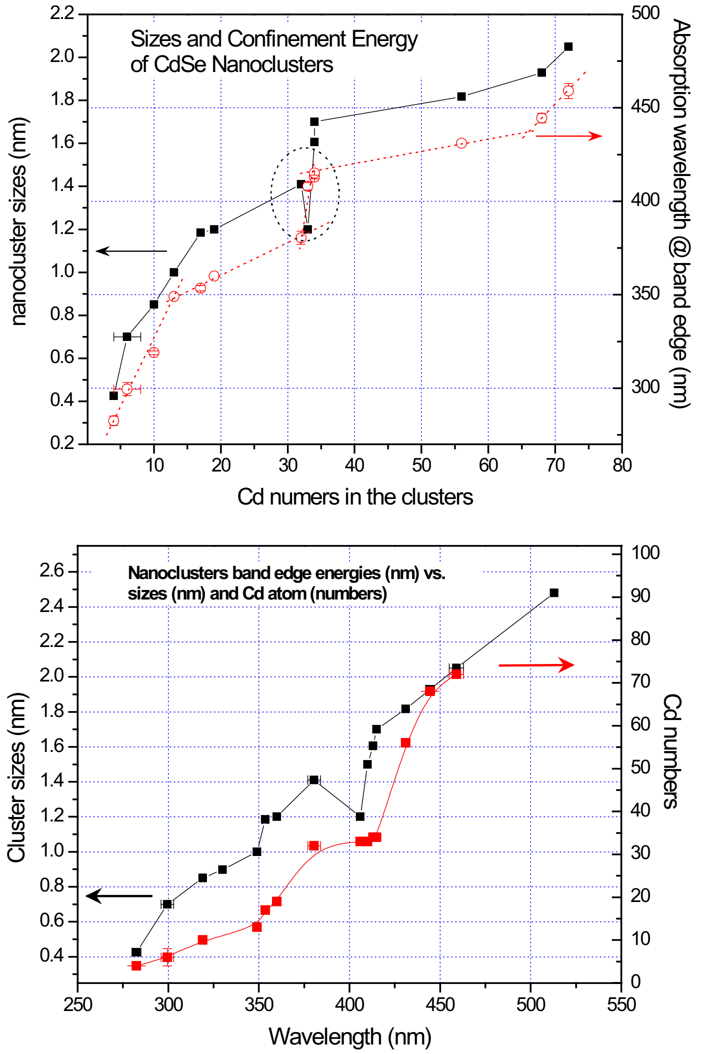

Figure 1.14 (a) Plotting of Cd numbers (*n*) versus CdSe nanocluster sizes (or diameter, nm) and absorption wavelengths (nm). (b) Plotting of CdSe nanocluster absorption wavelengths (nm) versus Cd numbers (*n*) and sizes (or diameter, nm).

To explicitly resolve size (diameter) dependence on the magic numbers, absorption wavelengths (λ) are plotted with nanocluster sizes (left-axis, black curve) and Cd atom numbers (*n*, right y-axis, red curve) in Figure 1.14 (b). Both black and red curves show two sudden slope changes round 350 nm and 410 nm, corresponding to excitonic absorption wavelengths of $(CdSe)_{13}$ and $(CdSe)_{33}$. The black curve shows direct evidence of a size contraction (or plateau) between 1.2 nm and 1.4 nm (n = 17-32), and then size expansion between 1.4 nm and 1.7 nm (n = 32-34). The red curve also shows a large wavelength increment from 380 to 415 nm that corresponds to $(CdSe)_{32-34}$ nanoclusters. A huge jump (415 – 380 nm = 35 nm) indicates strong dependence on the magic numbers between 32 and 34. This also suggests a hypothesis that larger binding energy from filling the core of the $(CdSe)_{28}$ cage-like structure may affect a total exciton energy in addition to the confinement energies from confined sizes.[4]

1.3.3 Quantum Confinement Energy (Wavelength)

Cadmium selenide nanoclusters experience very strong quantum confinement in three dimensions due to their ultra-small sizes (less than a half of CdSe Bohr radius, r_B = 5.6 nm). According to the effective mass approximation (EMA), the calculated band gap energy (E_g) was linearly proportional to the $1/d^2$ as shown in equation 1.3.[22-23]

$$E_g = E_{g,bulk} + \frac{h^2 n^2}{8d^2}\left[\frac{1}{m_e^*} + \frac{1}{m_h^*}\right] \qquad (1.3)$$

In equation 1.3, the EMA quantum confinement energy (ΔE_g) linearly depended on $1/d^2$ (d, sizes or diameter). However, a linear dependence only occurs experimentally when diameter is large ($d > 1.2$ nm, $1/d^2 < 0.7$) as shown in Figure 1.15. The results establish that small CdSe clusters are fundamentally different from the large CdSe nanocrystals.

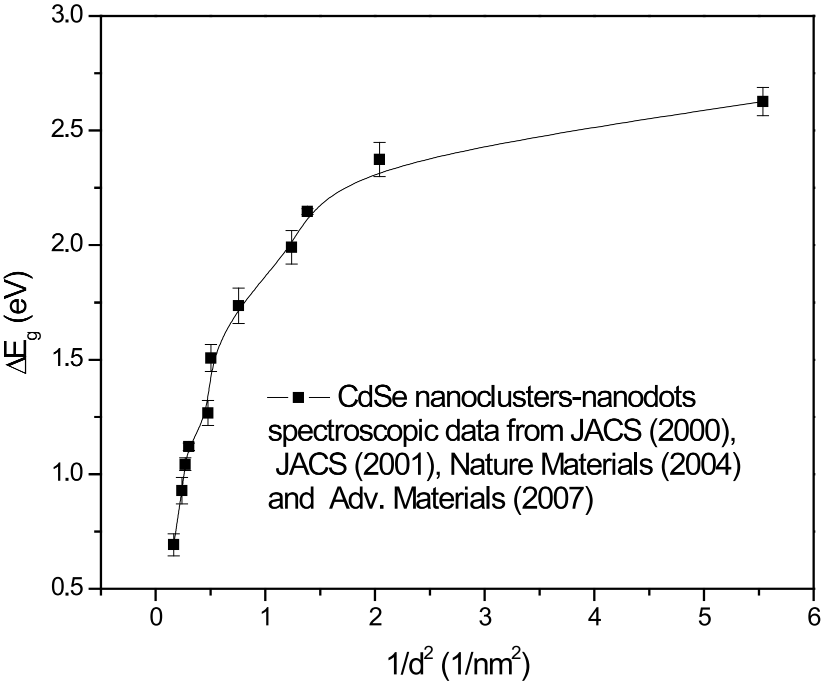

Figure 1.15 Plotting of confinement energies ($\Delta E_g = E_{,g} - E_{g,\ bulk}$) of CdSe nanoparticles (nanocrystals) versus diameters. [3-4, 6, 10]

To better understand the quantum confinement energy in small nanoclusters, more experimental results of small CdSe nanoparticles and nanoclusters are calibrated with their magic numbers and absorption wavelengths in Figure 1.16. In Figure 1.16 (a), the excitonic absorption wavelengths follow an approximately exponential growth corresponding to Cd atom numbers in CdSe nanoclusters. In Figure 1.16 (b), the excitonic absorption wavelengths follow a nearly linear relationship corresponding to diameters of CdSe nanocluster. In both figures, error bars are large for the deviating absorption features around 360 and 410 nm from the calibration curves (red exponential curve and red line). This suggests that the confinement energy encounters some minor effects from both Cd atom number and sizes when nanoclusters have magic sizes.

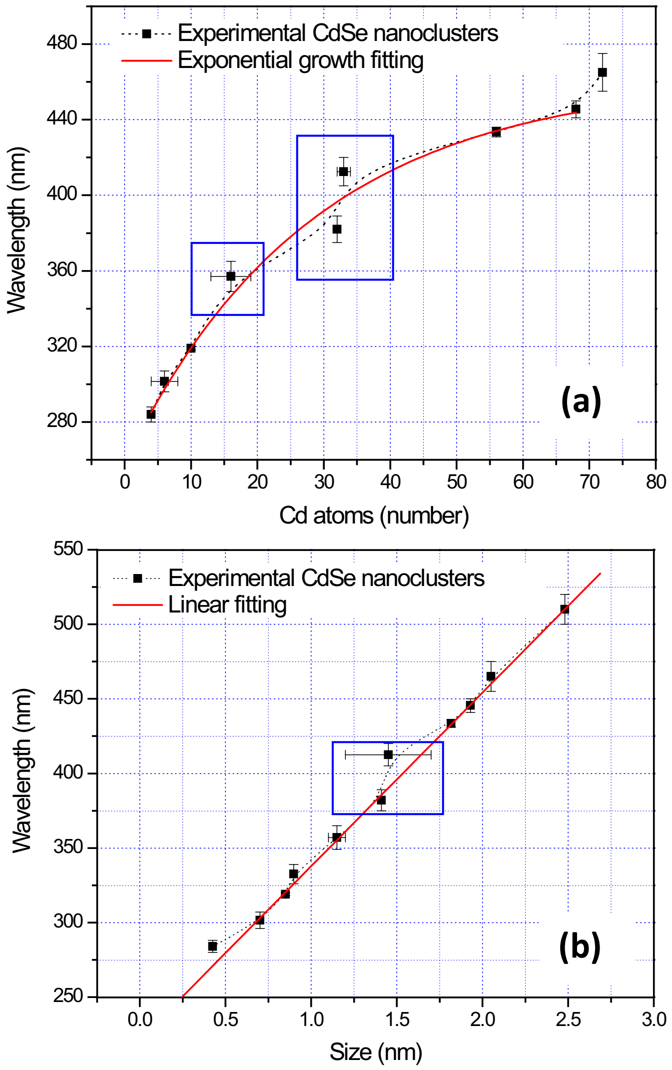

Figure 1.16 (a) Absorption wavelengths of CdSe nanoclusters follow an approximately exponential growth corresponding to the Cd numbers (4-68). (b) Absorption wavelengths of CdSe nanoclusters follow a linear relationship to their sizes regime (0.4-2.4 nm).

The $(CdSe)_{33}$ and $(CdSe)_{34}$ are representatives of the magic-sized numbers with large binding energies. When the nanoclusters grow around the sizes of the magic numbers, the $(CdSe)_{33}$ nanocluster (below the exponential calibration curve) experiences stronger quantum confinement energy than $(CdSe)_{34}$ nanocluster (above the exponential calibration curve), as shown in the blue box in Figure 1.16 (a). It may be inferred that a size contraction was responsible for the quantum confinement energy $(CdSe)_{33}$, and a size expansion for $(CdSe)_{34}$.

1.3.4 Self-assembly of Magic-Sized CdSe Nanocluster Arrays (NCA)

In 2007, Manna and coworkers reported sequential growth of magic-sized CdSe nanocrystals from small to large sizes, named as cluster families 1-6, at 80 °C.[10] Within the first 15 min, the smallest CdSe nanoclusters (cluster family 1) were identified with well-resolved absorption wavelengths at 330 and 350 nm. The earlier Kasuya work established that cluster family 1 consists of $(CdSe)_{13}$. In the next 2500 min (~42 h), cluster family 1 consecutively transformed to cluster families 2-6. In 2008, Nann and coworkers used a large quantity of 1-hexadecylamine (HDA) in synthesizing ultra stable CdSe nanoclusters (NCs) at 100 ± 5 °C.[8] After 2 days, green-emitting CdSe NCs composed of two sized species with two emission wavelengths at 495 and 450 nm were obtained. One emission at 450 nm continued to grow while another emission at 495 nm gradually disappeared in 10 days. This is the first experimental report of a spontaneous size reduction of CdSe nanoclusters.

We synthesized our magic-sized CdSe nanocluster from Cd-amine complexes. Several evidences show that Cd-amine complexes formed lamellar structures after a cadmium starting material was dissolved into amines.[17] Hyeon et al. reported the cadmium-amine complexes of a formula $CdX_2(OA)_2$ (X: halide, OA: octylamine). Strong diffraction peaks at low angle in the XRD patterns indicate repeating slabs of $CdX_2(OA)_2$ in a lamellar structure.[18] After the selenium precursor is injected, it intercalates the slabs and exchanges with the X^- anions. As a result of the CdX_2 precursors, the CdSe magic clusters are obtained and produced in the same lamellar templates.

Experimental experience suggests that lower synthesis temperature and amines facilitate growth of smaller CdSe clusters. Synthesis of CdSe NCAs was conducted in the glove box at room temperature (20-25 °C). During the synthesis of CdSe clusters, two different sizes of CdSe clusters co-existed during the reaction. Within the first few minutes after the reaction, we first observed the absorption peaks of $(CdSe)_{33\text{-}34}$ nanoclusters around 390-410 nm, and a minor peak at $(CdSe)_{19}$ around 360 nm, which gives light yellow products. The color of the mixture is not easily visualized until TOP is introduced to remove excess Se and Se-*n*-OA complex. As the reaction proceeds, the clusters become paler and the peaks of $(CdSe)_{13}$ are observed around 330-350 nm. In the following 12 h, the cluster spectrum indicates a mixture of both $(CdSe)_{13}$ and$(CdSe)_{33\text{-}34}$ clusters. After 12-44 h, the product is a spectrally pure $(CdSe)_{13}$. According to the literature, $(CdSe)_{13}$ has been assigned to diameter of ~ 1 nm while $(CdSe)_{33\text{-}34}$ has been assigned to a diameter range of 1.2-1.7 nm.[9,29] Such a size reduction is unusual for conventional CdSe nanoparticle syntheses.

Such a size reduction is likely favorable if $(CdSe)_{13}$ is more thermodynamically stable than $(CdSe)_{33\text{-}34}$ at room temperature in the amine template. At elevated temperature, there is a competition between size reduction and attachment. The size reduction may *or* may not be observed due to a possible attachment of nanoclusters to form QBs.

The NCAs maintain their original lamellar structure before and after annealing. Before the annealing step, CdSe nanoclusters are loosely located in the lamellar structures and are unstable to polar solvents. After the annealing step at elevated temperature (> 60 °C), the CdSe clusters are somehow more tightly assembled and are much more stable to polar solvents. Red shifts due to ligand leaching were barely observed for annealed CdSe nanoclusters. Sonication of the as-made NCAs destroys the lamellar structures and releases the $(CdSe)_{13}$ clusters from the arrays. In contrast, sonication of the annealed NCAs in the presence of long-chain amines causes unbundling of the lamellar structure, but not layer disintegration. Proper treatment of as-made and annealed CdSe nanoclusters is extremely important in maintaining the lamellar structure and preventing nanocluster growth as shown in Figure 1.3 (a).

1.3.5 Attachment and Morphology Transformation

In recent years, ultra-small nanostructures, such as nanowires and nanobelts, have been made by attachment of nanoclusters and nanoparticles.[18, 20-22] It has been known that CdE (E=S, Se, and Te) nanoparticles have strong dipole-dipole interactions as a primary driving force to construct larger superstructures. The mechanism to make these superstructures is reported as "oriented attachment."[20] Oriented attachment is employed to link small nanoparticles to form nanorods, nanowires, nanodisks, and nanoplatelets of various semiconductors and metal oxides. Peng's group has investigated their axial-growth in a thermodynamic model and predicted nanowires as the most stable structure after the oriented attachment of CdSe nanocrystals.[30] Under some conditions, these attached nanostructures may attach along other directions instead of the axial-growth direction. Various nanostructure morphologies, such as nanowires, nanobelts, nanoplates, nanosheets and nanoribbons have been made due to space confinement and energy preference.[18, 20-22]

We have observed a similar morphology transformation from CdSe nanocluster arrays (NCAs) to CdSe quantum belts (QBs) via a similar attachment process. The CdSe QBs can be synthesized by a one-step or a two-step method depending on the synthesis temperatures. The one-step method requires a moderate synthesis temperature (64-70 °C), and will be discussed in Chapter 2. The two-step method only requires a low synthesis temperature (room temperature, 20-25 °C) but high annealing temperature (98-110 °C). Both methods result in CdSe QBs that exhibit nearly identical absorption and emission spectra. However, an incomplete attachment sometimes occurs in the two-step method. In Figure 1.18, dark features residing in gray belt shadows are aggregated particles from randomly attached CdSe nanoclusters. This aggregation provides a direct evidence of morphology transformation from NCAs to QBs.

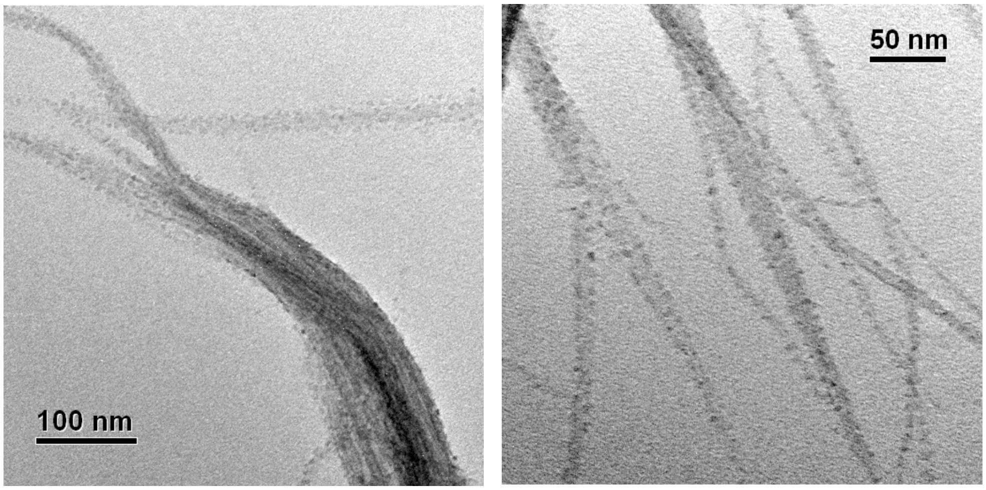

Figure 1.17 Representative TEM images of CdSe QBs made in a two-step process. Dark areas indicate possible aggregations of CdSe nanoclusters. Gray shadows are CdSe QBs. A discontinuous color change indicates an incomplete attachment of CdSe nanoclusters.

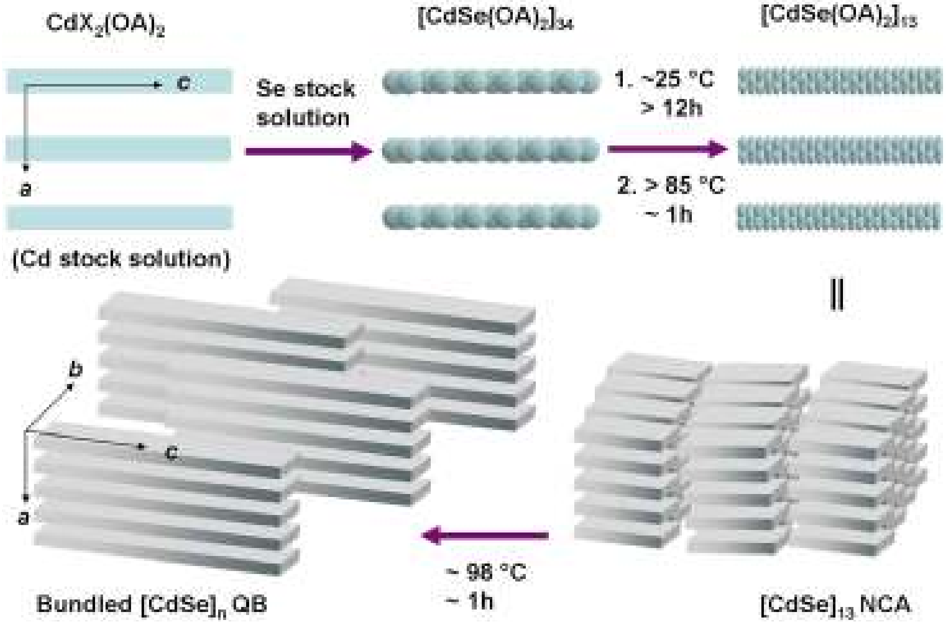

Scheme 1.3 The morphology transformation from Cd-amine complexes to CdSe nanocluster arrays (NCAs), then to CdSe quantum belts (QBs).

The attachment rate is quite slow (in days) at room temperature, but becomes much faster (in hours) at high temperature (> 98 °C). The attachment may occur in all dimensions, primarily depending on temperature and energy-preferred orientation.[30] In Scheme 1.2, we use *a*, *b*, and *c* vectors to indicate the three attachment directions. Transformation from NCAs to QBs requires attachment in *a* (thickness), *b* (width) and *c* (length) dimensions.

1.4 Conclusion

Molecular-like CdSe nanoclusters have been synthesized in amine-based templates. At room temperature (20-25 °C), $Cd(OAc)_2(OA)_2$ complexes are assembled in lamellar structures, followed by an anion exchange with a selenium precursor, and a formation of CdSe nanoclusters. Two series of magic-sized nanoclusters are characterized in situ and monitored spectroscopically during the synthesis. By tuning temperature and other conditions, nanoclusters can further attach within the lamellar structures to form solid CdSe quantum belts (QBs). Unbundling of the CdSe nanocluster arrays is possible by a ligand-exchange process with oleylamine and an expansion of the layer-to-layer distance.

1.5 Experimental

1.5.1 Materials

n-Octylamine (*n*-OA) from Aldrich (+99%, product #: O5802-500G) and Alfa Aesar (99%, product #: B24193), selenourea (99.9%, metal basis) from Alpha Aesar, $Cd(OAc)_2 \cdot 2H_2O$ (Aldrich), oleylamine (or cis-9-octadecenylamine) from Sigma-Aldrich (technical grade, 70%) and TCI (> 40.0% by GC) were used as received, and stored under N_2. Toluene from Sigma-Aldrich (CHROMASOLV®, for HPLC, ≥ 99.9%) was purged with dry N_2 for at least 1 h and stored under N_2 prior to use.

1.5.2 Synthesis of CdSe Nanocluster Arrays (NCAs).

In a typical reaction, cadmium acetate dihydate [$Cd(OAc)_2 \cdot 2H_2O$] (80 mg, 0.30 mmol) was dissolved in *n*-octylamine (*n* –OA, 6.7g, 0.052 mol) in a sealed tube. The tube was stirred and heated at 68 °C oil bath for at 1h. A colorless clear solution of Cd-amine complex was obtained (clear or pale yellow). In a glove box, selenourea (67 mg, 0.54 mmol) was used as a Se starting material dissolved in octylamine (2.8 g, 0.022 mol) in an amber vial. The solubility of selenourea was low in *n*-OA and a total dissolution required a vigorous sonication for 10-20 min. If a regular transparent vial was used to load the selenourea, it gradually decomposed under a room light and an orange or dark red solution was observed. This was an indication of formation of elemental selenium and recombination with *n*-OA to form Se-*n*-OA complex. When an amber vial was used, a colorless or pink solution indicated a fresh Se precursor solution.

The Se precursor solution was injected into the Cd precursor solution. However, in various trials the reaction stoichiometry was adjusted to provide Se/Cd ratios in the ranges of 1.73-1.82. The reaction proceeded gradually at room temperature (20-25 ^{o}C). During the first hour, the reaction experienced multiple color changes from colorless (0 min) to orange-yellow (viscous, < 15 min), yellow (cloudy, 15-120 min) to greenish-yellow (cloudy, > 120 min) with some brown residues. After reaction at room temperature for 2 h, the solution turned pale with greenish yellow precipitates, which indicated a formation of CdSe nanoclusters. Slow stirring of the sealed tube under ambient conditions for another 12-44 h resulted in a completely white precipitate. At this stage the reaction solution was pink. The white precipitate was referred to "as-made" CdSe nanoclusters, and was composed of mainly of $(CdSe)_{13}$ with minor amounts of $(CdSe)_{19}$ and $(CdSe)_{33-34}$. The relative amount of $(CdSe)_{19}$, $(CdSe)_{33-34}$ depended on the Se/Cd ratio. The optimal Se/Cd ratio for spectrally pure $(CdSe)_{13}$ was 1.73. Continued annealing of as-made CdSe nanoclusters proceeded in an oil bath at 85 ^{o}C for 1h. The white precipitate remained in the bottom one-third of the reaction volume. At this stage the reaction solution was dark red and a small amount of black or gray precipitate had separated. The solid was elemental Se that was subsequently removed by a TOP solution. The white precipitate after the annealing was referred to as "annealed" CdSe nanoclusters.

Both as-made and annealed CdSe nanoclusters were purified with a TOP-toluene solution (5-10 %, w/w) prior to other characterizations. After the TOP-toluene solution (2-3 mL) was injected, the reaction was quenched and the dark red solution quickly turned a colorless clear solution with white precipitates settled at the tube bottom. The white precipitates were centrifuged in a bench-top centrifuge for 1-3 min. The supernatant was discarded. The purification process was repeated 1-2 times by adding TOP-toluene solution or toluene. The white precipitate was referred to as "purified" CdSe nanoclusters. The purified nanoclusters were re-dissolved in the TOP-toluene solution or toluene for further characterizations.

1.5.3 Unbundling of CdSe NCAs

The unbundling process was conducted in oleylamine-toluene solution. For analysis of the "unbundled" CdSe NCAs, an aliquot (ca. 0.1 mL) from the suspension of "purified-annealed" CdSe NCAs was diluted into oleylamine-toluene (20 %, w/w, 1 mL) in air. The unbundling process took 5-7 days proceeding at room temperature, or was expedited by sonication for 5-20 min. The CdSe NCAs became a clear pale colorless solution after unbundling. The NCAs were flocculated from this dispersion by 1-2 drops of acetone (< 0.1 mL) in air and the resulting mixture was centrifuged in a bench-top centrifuge for ≥ 15 min to produce a white unbundled NCA precipitate. The supernatant was discarded. An additional portion of toluene (1 mL) and acetone (0.05 mL) was added to the precipitate, and the mixture was centrifuged as above. The supernatant was again discarded and the white NCA precipitate was re-dispersed into toluene (2 mL) to afford a clear, colorless dispersion of unbundled NCAs for TEM analysis.

1.5.4 Transformation of as-made CdSe NCAs to CdSe quantum belts

The transformation was conducted in the same synthesis solution of the as-made CdSe nanoclusters. The reaction tube containing the as-made CdSe nanoclusters before TOP purification was directly placed in an oil bath for the transformation. After the transformation process with stirring at 98 °C for 1h, the solution turned dark greenish-brown and a small amount of brownish black precipitate formed. The brownish black precipitate was identified as elemental Se by XRD. The original white precipitate became greenish yellow, which was mainly CdSe QBs. The TOP-toluene solution (5-10 %, w/w), was injected to remove excess Se precursor as well as to dissolve elemental Se from the reaction. The colorless clear supernatant was centrifuged again in a bench-top centrifuge for 1-3 min. After repeating the TOP purification and centrifugation for 1-2 times, a greenish yellow precipitate was obtained and stored under N_2 for future characterizations.

1.5.5 Absorption spectroscopy.

Most spectroscopic analyses of CdSe NCAs were conducted in toluene, oleylamine-toluene solution (10-20 %, w/w), or TOP-toluene solution (5-10 %, w/w). The CdSe NCA suspension was first centrifuged in a bench-top centrifuge for 3-5 min to produce a white NCA precipitate. The white precipitate was shaken and redispersed in the same mixture, which was followed by a subsequent centrifugation to remove excess ligands in the solution. This cycle was repeated 1-2 times with re-dispersion in the same mixture.

Absorption spectra were collected at room temperature using a Varian Cary 100 Bio UV-visible spectrophotometer. The sample absorbance was adjusted to 0.05-0.15 at 350 nm. In each UV-vis spectroscopic analysis, the same background solution, toluene or an oleylamine-toluene or a TOP-toluene solution, was used for the reference and sample. A baseline correction was also applied to account for cuvette absorption. Oleylamine has a strong, sharp absorption at 332 nm, which appeared in the spectra if the oleylamine concentrations in the sample and reference cuvettes were imbalanced, or if the baseline was inadequately corrected.

1.5.6 X-ray powder diffraction (XRD).

At least 2-3 mL of the suspension of as-made or annealed NCAs in *n*-OA (from "Synthesis of CdSe NCAs") were required to obtain an XRD pattern. The CdSe NCA sample was injected with 1-2 mL of TOP-toluene solution (5-10 %, w/w) to remove excess ligands (*n*-OA) and side products (SeTOP) prior to XRD sample preparation. The NCA suspension (3-5 mL) was centrifuged in a bench-top centrifuge for 5 min and the supernatant was discarded. Toluene (2 mL) was added to the white NCA precipitate, and the mixture was shaken a few times and then centrifuged for 5 min. Most of the supernatant was discarded and toluene (0.1 mL) was added into the precipitate. In some cases, the white precipitate turned a little green after the toluene purification. A small amount of *n*-OA (1-2 drops) was necessarily added into the precipitate slush to prevent further size growth.

The "wet" white slush was transferred (cast-coated) onto an XRD glass slide and dried in a fume hood exhausting at high face velocity. Transfer and drying were repeated for 3-5 times, which usually required 1 h to complete. XRD patterns were obtained using a Rigaku Dmax A vertical powder diffractometer with Cu Kα radiation (λ = 1.5418 Å) and Materials Data Incorporated (MDI) automation and Jade software. The step size was 0.008° and the retention time was 1 sec for both low-angle (1.5-15°) and high-angle (20-65°) measurements.

1.5.7 Transmission electron microscopy (TEM)

For analysis of bundled CdSe NCAs, an aliquot from the suspension of as-made NCAs (ca. 0.1 mL) was diluted into toluene (1 mL) in air. The mixture was shaken a few times and centrifuged in a bench-top centrifuge for 5 min. This gave a white precipitate and a nearly colorless supernatant. The supernatant was discarded, and the NCA precipitate was re-diluted into toluene (1 mL). The mixture was shaken and then centrifuged as above. The supernatant was again discarded and the white NCA precipitate was dispersed in toluene (1 mL) to yield a white dispersion for subsequent TEM analysis. For analysis of unbundled CdSe NCA, detailed unbundling and purification processes were described in "Unbundling of CdSe NCAs."

A drop of the appropriate CdSe NCA dispersion was transferred onto a carbon-coated Cu grid (Ted Pella, PELCO® 300 Mesh Grids, product #: 1GC300). The solvent on the Cu grid was evaporated in the ambient atmosphere. This process was usually repeated twice to load enough CdSe NCAs onto the grid (concentration dependent). TEM images of CdSe NCAs were collected using a JEOL 2000 FX microscope with an acceleration voltage of 200 kV. HRTEM was conducted on a JEOL-2100F using TEM grid with holey-carbon film (Ted Pella, Ultrathin Carbon Film on Holey Carbon Support Film, 400 mesh, Copper, product #: 01824).

1.6 References

1. Ouyang, J.; Zaman, M.; Yan, F.J.; Johnston, D.; Li, G.; Wu, X.; Leek, D.; Ratcliffe, C.I.; Ripmeester, J. A.; Yu K. *J. Phys. Chem. C*, **2008**, *112*, 13805-13811.
2. Riehle, F. S.; Bienert, R.; Thomann, R.; Urban, G. A. *Nano Lett.*, **2009**, *9*, 514-518.
3. Soloviev, V.N.; Eichhöfer, A.; Fenske, D.; Banin, U. *J. Am. Chem. Soc.* **2001**, *123*, 2354-2364.
4. Kasuya, A.; Sivamohan, R.; Barnakov, Y.A.; Dmitruk, I.M.; Nirasawa, T.; Romanyuk, V.R.; Kumar, V.; Mamykin, S.V.; Tohji, K.; Jeyadevan, B.; Shinoda, K; Kudo, T; Terasaki, O; Liu, Z.; Belosludov, R.V.; Sundararajan, V.; Kawazoe, Y. *Nat. Mater.* , **2004**, *3*, 99 – 102.
5. Behrens, S.; Bettenhausen, M.; Eichhöfer, A.; Fenske, D. *Angew. Chem. Int. Ed*. **1997**, *36*, 2797-2799.
6. Soloviev, V.N.; Eichhöfer, A.; Fenske, D.; Banin, U. *J. Am. Chem. Soc.* **2000**, *122*, 2673-2674.
7. Wang, H.; Tashiro, A.; Nakamura, H.; Uehara, M.; Miyazaki, M.; Watari, T.; Maeda, H. *J. Mater. Res.* **2004**, *19*, 3157-3161.
8. Kuçur, E.; Ziegler, J.; Nann, T. *Small*, **2008**, *4*, 883-887.
9. Murray, C.B.; Norris, D.J.; Bawendi, M.G. *J. Am. Chem. Soc.* **1993**, *115*, 8706-8715.
10. Kudera, S.; Zanella, M.; Cianninin, C.; Rizzo, A.; Li, Y.; Gigli, G.; Cingolani, R.; Ciccarella, G.; Spahl, W.; Parak, W.J.; Manna, Liberato *Adv. Mater.*, **2007**, *19*, 548-552.
11. Peng, Z.A.; Peng, X. *J. Am. Chem. Soc.* **2002**, *124*, 3343-3353.
12. Chen, H.S.; Kumar, R. V. *J. Phys. Chem. C*, **2009**, *113*, 31-36.
13. Sun, M.; Yang, X. *J. Phys. Chem. C*, **2009**, *113*, 8701-8709.
14. Xi, L.; Tan, W. Z. W.; Boothroyd, C.; Lam, Y. M. *Chem. Mater.* **2008**, *20*, 5444-5452.

15. Xi, L.; Lam, Y. M. *Chem. Mater.* **2009**, *21*, 3710-3718.

16. Tang, Z.; Kotov, N.; Giersig, M. *Science*, **2002**, *297*, 237-240.

17. C. C. Hines, W. M. Reichert, S. T. Griffin, A. H. Bond, P. E. Snowwhite, R. D. Rogers, *J. Mol. Struct.* **2006**, *796*, 76-85.

18. Son, J.S.; Wen, X.D.; Joo, J. Chae, J.; Baek, S.I.; Park, K.; Kim, J.H.; An, K.; Yu, J.H.; Kwon, S.G.; Choi, S.H.; Wang, Z.; Kim, Y.W.; Kuk, Y.; Hoffmann, R.; Hyeon, T. *Angew. Chem. Int. Ed.* **2009**, *48*, 6861-6864.

19. Yener, D.O.; Sindel, J.; Randall, C.A.; Adair, H.A. *Langmuir,* **2002***, 18,* 8692-8699.

20. Pradhan, N.; Xu, H.; Peng, X. *Nano Lett.* **2006**, *6*, 720-724.

21. Joo, J.; Son, J.S.; Kwon, S.G.; Yu, J.H.; Hyeon, T. *J. Am. Chem. Soc.* **2006**, *128*, 5632-5633.

22. Ithurria, S.; Dubertret, B. *J. Am. Chem. Soc.* **2008**, *130*, 16504-16505.

23. Liu, Y.H.; Wayman, V. L.; Gibbons, P. C.; Loomis, R. A.; Buhro, W. E. *Nano Lett.*, **2010**, *10*, 352–357.

24. Peng, Z.A.; Peng, X. *J. Am. Chem. Soc.* **2001**, *123*, 1389-1395.

25. Jose, R.; Zhanpeisov, N. U.; Fukumura, H.; Baba, Y.; Ishikawa, M. *J. Am. Chem. Soc.* **2006**, *128*, 629-636.

26. Killina, S.; Ivanov, S.; Tretiak, S. *J. Am. Chem. Soc.* **2009**, *131*, 7717-7726.

27. Chung, S.Y.; Lee, S.; Liu, C.; Neuhauser, D. *J. Phys. Chem. C*, **2009**, *113*, 292-301.

28. K. Wade, *Adv. Inorg. Chem. Radiochem.*, **1976**, *18*, 1.

29. Ptatschek, V. *et al. Ber. Bunsenges. Phys. Chem.* **1998**, *102*, 85-95.

30. Barnard, A.S.; Xu, H.; Li, X.; Pradhan, N.; Peng, X. *Nanotechnology*, **2006**, *17*, 5707-5714.

Chapter 2: Temperature-Controlled Synthesis of CdSe Quantum Belts

2.1 Introduction

In recent years, oriented attachment has been widely used to synthesize ultra-small one-dimensional (1D) nanowires and nanorods.[1-3] These nanowires and nanorods can be made of lower dimensional nanostructures, such as nanoclusters (0D) and nanodots (0D), and even nanorods (1D), as unit building blocks. Strong dipole-dipole interactions between each unit block drive the initial 1D assembly, enhancing the conversion to the final nanostructures. [1, 4-5] Recently, 2D nanostructures, such as nanosheets,[6-8] nanoplatets[9-10] and nanoribbons, [11] have also been prepared by similar oriented-attachment mechanisms in colloidal strategies. [12]

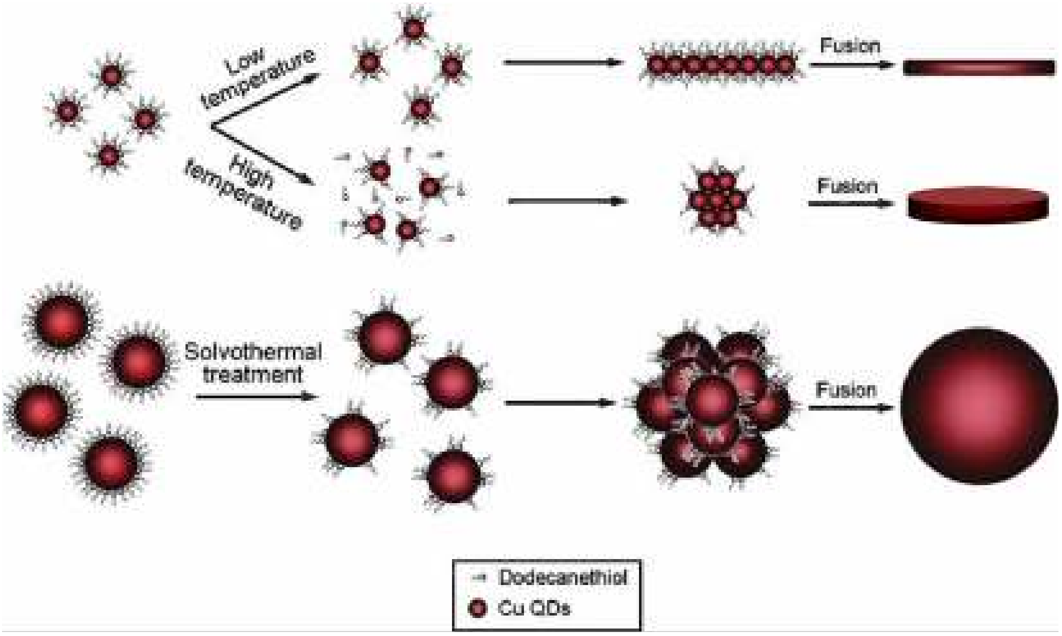

Scheme 2.1 Scheme of shape effects in the oriented attachment growth process of Cu-DT nanoseeds.[3]

Peng's and Krüger's groups both made ultra-small nanowires (2.1 and 1.6 nm) by oriented attachment.[13-14] During the early stage of their syntheses, CdSe dots were observed in pearl or necklace superstructures (pre-wires). Transformation of the pre-wires to long and solid nanowires was achieved at room temperature for several days or by annealing for a short period of time at elevated temperature. Peng also investigated a thermodynamic model of varying axial-growth direction to predict possible stable products.[12] According to the energy calculations, nanowires were predicted as the most energetically stable products by oriented attachment.

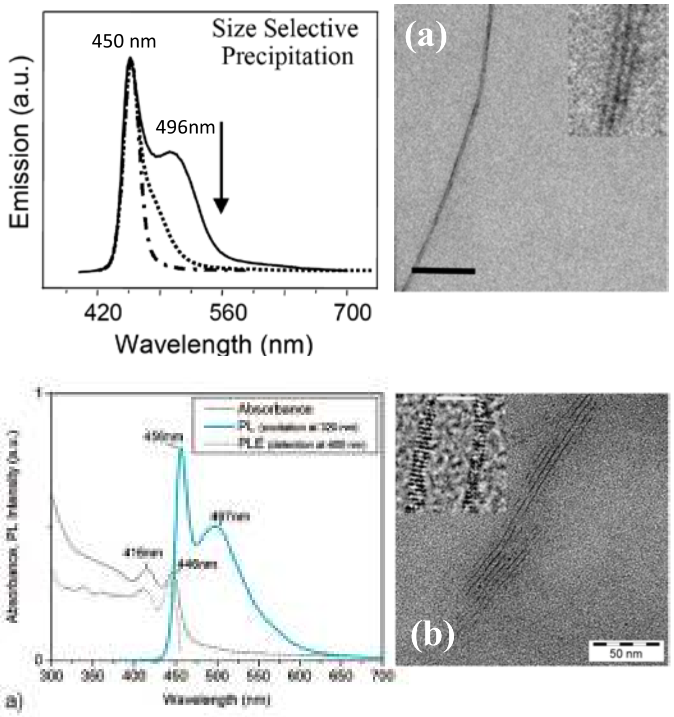

Figure 2.1 Representative TEM images and emission spectra of ultra-small CdSe nanowires (NWs). (a) NWs of 2.1-nm diameter were made by Peng and coworkers;[13] (b) NWs of 1.6-nm diameters were made by Krüger and coworkers.[14]

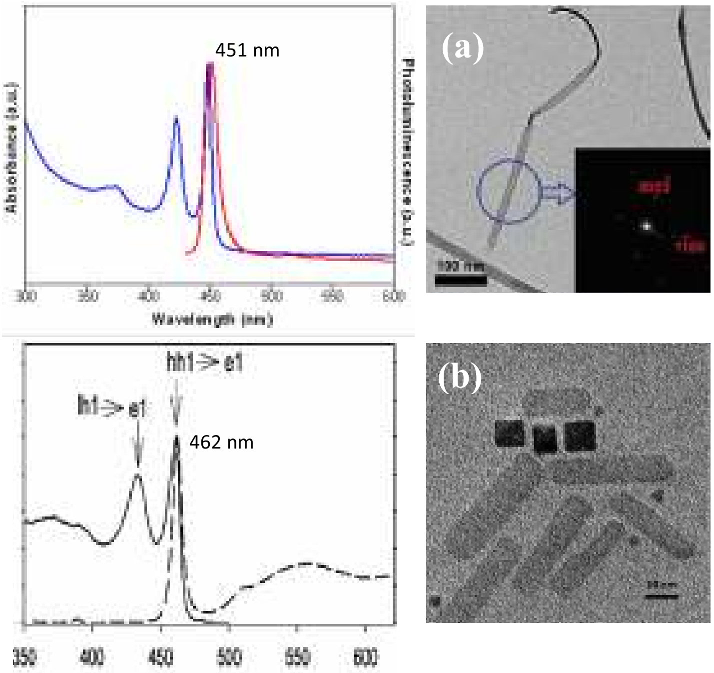

Figure 2.2 Representative TEM images and emission spectra of ultra-small CdSe quantum-well structures. (a) Nanoribbons of 1.4 nm thickness were made by Hyeon and coworkers;[11] (b) Nanoplatelets of 1.93 nm thickness were made by Ithurria and Dubertret.[10]

Attachment may also produce nanostructures of other morphologies. Hyeon's and Dubertret's group synthesized CdSe quantum-well nanostructures with thicknesses of 1.4 to 2.5 nm.[8, 10-11] Hyeon et al. reported the smallest thickness (1.4 nm) of CdSe nanoribbons and nanosheets. In their recent study, experiments showed that lamellar nanostructures existed in the early preparation stage as cadmium-amine complexes.[8]

Dubertret et al. also reported nanoplatelets with similar optical properties as shown in Figure 2. They claimed that introduction of acetate salts triggers the formation of square or rectangle shape nanoplatelets.[10] They resolved the absorption spectrum of CdSe nanoplatelets of different sizes with light-hole and heavy-hole transitions. Each transition computes to a very similar thickness, e.g. 1.93 nm. The agreement of the two thickness values confirmed attribution of the light-hole and heavy-hole transitions in quantum well nanostructures.

In this chapter, I report a facile method of synthesizing CdSe quantum belts (QBs) of two different thicknesses (averaged 1.8 and averaged 2.8 nm) at low temperature ranges (60 °C and 120 °C). [15] The morphology transformation has been observed during and after the QB synthesis. Magic-sized nanoclusters, such as $(CdSe)_{33\text{-}34}$ and $(CdSe)_{13\text{-}19}$, have been shown as intermediate precursors to grow the averaged 1.8-nm QB. More interestingly, the averaged 1.8-nm QB can further redistribute its thickness dimension and transform to the averaged 2.8-nm QB after the annealing process. In this chapter, more detail about the crystallographic and optical characterizations of CdSe QBs will be explicated with discussion.

2.2 Results

2.2.1 Synthesis of CdSe QBs.

Two types of CdSe QBs were synthesized from cadmium acetate and selenourea in *n*-octylamine by a slight modification of the procedure of Peng and coworkers.[2] The type-I CdSe QB thickness (1.5-2.0 nm, averaged 1.8 nm) were made over a wide temperature range from 45-80 °C, while the type-II CdSe QB thickness (2.5-3.0 nm, averaged 2.8 nm) were made at higher temperature around 120 °C. The type-I CdSe QBs were structurally and morphologically similar to the CdSe nanoribbons reported by Hyeon and coworkers.[1]

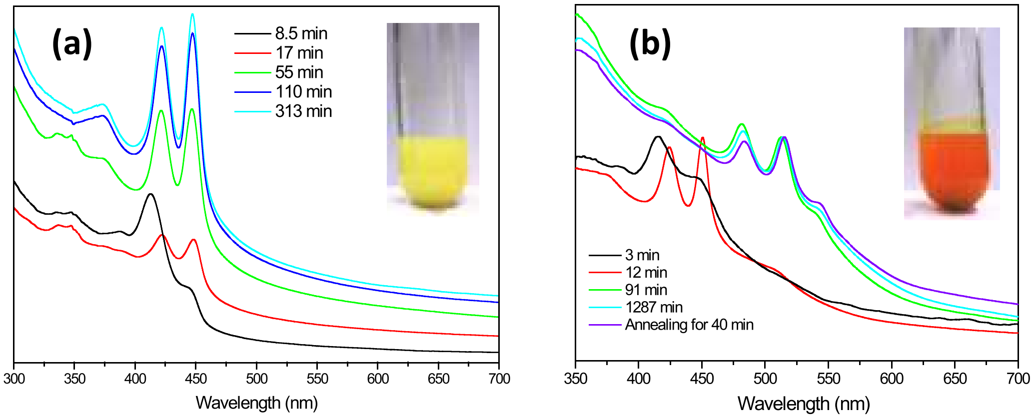

Figure 2.3 The formation of type-I and type-II CdSe QBs synthesized at (a) 68 ºC and (b) 120 ºC plus annealing at 140 ºC. The absorption peaks were monitored during the first 3-17 minutes, followed by the next 1.5 hours (55-91 min) and after 5 hours (> 313 min). Insert pictures are the final product colors after an injection of TOP-toluene solution.

In Figure 2.3 (a), several CdSe nanoclusters were identified prior to the formation of the type-I CdSe QBs. The absorption peaks at 446 nm, 412 -390 nm, 362-333 nm were assigned to electronic transition wavelengths of (CdSe)$_{64}$ (~1.9 nm), (CdSe)$_{33\text{-}34}$ (1.2-1.7 nm), (CdSe) $_{19}$ (1.0-1.2 nm), and (CdSe)$_{13}$ (1.0 nm) nanoclusters.[16] After the first 17 minutes, the (CdSe)$_{33\text{-}64}$ peaks (446 nm, 412 nm, and 390 nm) gradually disappeared with emerging peaks at 445 nm and 420 nm. Two peaks were identified as light-hole and heavy-hole transitions of CdSe QBs. This identification suggested that colorless (CdSe)$_{13\text{-}19}$ and greenish yellow (CdSe)$_{32\text{-}68}$ were intermediates for type-I CdSe QBs during the synthesis.

In Figure 2.3 (b), similar spectroscopic transitions were observed during a formation of the type-II CdSe QBs at 120 ºC. In the first 3 min, electronic-transition wavelengths of (CdSe)$_{33\text{-}68}$ (1.2-1.9 nm) nanoclusters were observed at 446-390 nm. However, the (CdSe)$_{32\text{-}68}$ nanoclusters were not very stable at 120 ºC. In the next 12 min, the light-hole and heavy-hole transitions of the "type-I CdSe QBs" emerged while the electronic transition wavelengths of $(CdSe)_{33-68}$ (1.2-1.9 nm) disappeared. The type-I CdSe QBs were not stabilized under such a condition, and gradually transformed to type-II CdSe QBs after 79 min (91 min – 12 min).

In general, the as-made type-I CdSe QBs have appreciable quantum efficiencies (QE) of 7 ± 5 %. In Figure 2.4, a broad emission emerged soon after the first 52 min (red curve). The PL peaks became sharper and stronger with increased QEs of 9.8 % and 12.9 % after 218 min (green curve) and 1105 min (orange curve), respectively. Later when a higher temperature (85 °C, 38 min) was applied, a similar QE of 11.6 % was obtained.

Photoluminescence (PL) spectra of as-synthesized type-I and type-II CdSe QBs were compared in Figure 2.5. For type-I CdSe QBs, the emission energy was around 2.75 eV (or a wavelength of 451 nm). For type-II CdSe QBs, the emission energy was around 2.40 eV (or a wavelength of 516 nm). The emission features from the ensembles of QBs were usually very narrow (FWHM $\geq$ 50 meV) with small Stokes shifts of 25 meV (451 nm – 447 nm = 4 nm) and 9 meV (516 nm – 514 nm = 2 nm) for type-I and type-II CdSe QBs, respectively. Each QB was examined with four different excitation energies but no noticeable energy shift was observed.

Several factors may significantly affect the CdSe QB PL spectrum and vary QE under different conditions. More detail about PL enhancement and surface passivation of CdSe QBs will be discussed in Chapter 3.

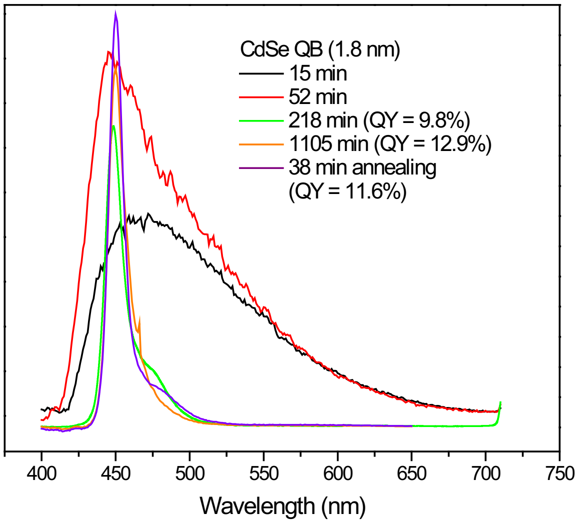

Figure 2.4 Monitoring the PL of type-I CdSe QBs during the synthesis and after annealing.

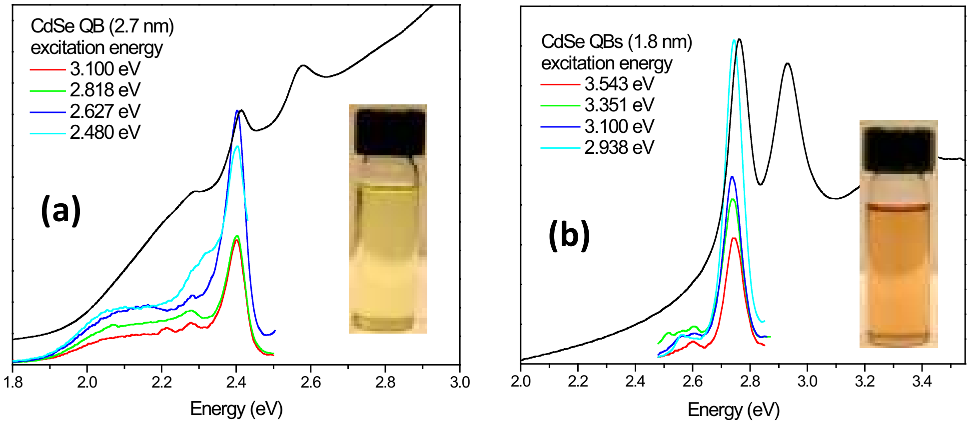

Figure 2.5 The absorption and emission properties of type-I CdSe QBs (a) and type-II CdSe QBs (b). Each sample was examined with four excitation energies above its band-gap energy.

2.2.2 Annealing of CdSe QBs

The as-made CdSe QB structure was fragile. A physical force, such as sonication waves, may quickly disassemble the QBs into smaller clusters with absorption and emission blue shifts in comparison to the as-made QBs. For a purpose of reinforced QB structures and quantum confinement property retention, an annealing process was required after synthesis. The annealing temperature was usually 20-30 °C higher than the synthesis temperature.[13] After the annealing process, another quick sonication process was applied to compare their quantum-confinement properties of the as-made and annealed QBs.

Both type-I and type-II CdSe QBs were investigated for the annealing effects. In Figure 2.6 (a), the type-I QBs were annealed at 90-110 °C for 1 h. After a sonication in toluene solution for 5 min, two emerging peaks (337 and 352 nm, fitted with black curves) were observed in the as-made QB absorption but not in the annealed QB absorption. This indicates that as-made type-I CdSe QBs gradually disassembled into $(CdSe)_{13}$ nanoclusters after the sonication process.

The type-II CdSe QB also became more stable after annealing. In Figure 2.6 (a), the type-II QBs were annealed at 140 °C for 1 h. After a sonication in toluene solution for 3 min, a blue shift of 5-6 nm was observed in the as-made CdSe QB absorption (black curve→ black dot curve), but no such a blue shift in the annealed QB absorption (red dot curve → red curve). The blue shift corresponded to a stronger quantum confinement system with a smaller dimension, which indicated shrinkage in the thickness dimension of the as-made QB after sonication. Even though an annealing helped to reinforce the nanostructures, a longer sonication time or many fold dilutions ultimately broadened the absorption peaks with blue shifts.

Peng and co-workers also reported the importance of annealing on colloidal CdSe nanostructures.[13] A similar spectral shifting was reported for pearl-like pre-wires prior to annealing. Without annealing, the pre-wires disassembled into randomly distributed nanoparticles. Therefore, an appropriate annealing was required before further surface treatment or reaction.

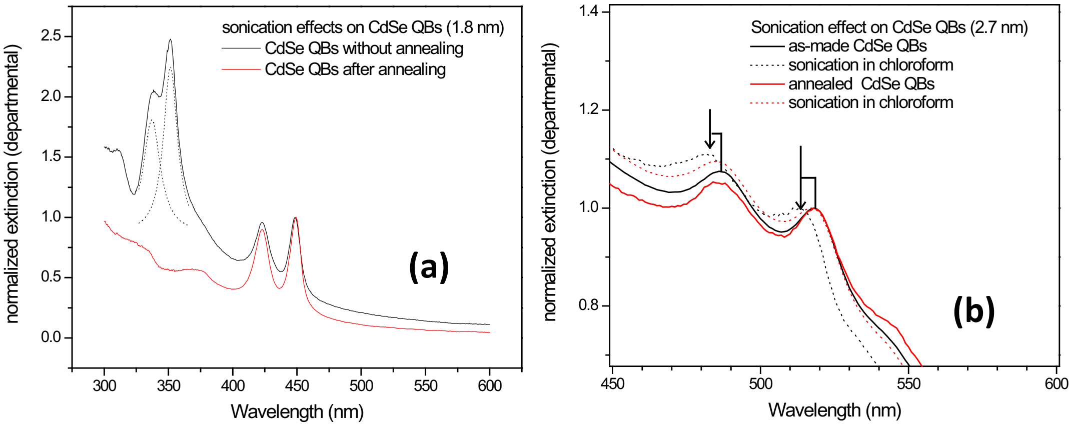

Figure 2.6 The absorption of CdSe QBs after sonication. (a) As-made (black curve) and annealed (red-curve) type-I CdSe QBs after 5-min sonication in toluene solution. (b) As-made (black curves) and annealed (red-curves) type-II CdSe QBs before (solid curves) and after (dot curves) 3-min sonication in chloroform solution.

2.2.3 Photoluminescence of CdSe QBs

Photoluminescence (PL) of CdSe QBs depends on surface passivation and ligand concentration. Adding tri-*n*-octylphosphine (TOP) into the as-made QBs unintentionally altered the surface passivation during a purification process. An unusual correlation between TOP concentration and PL intensity resulted in quantum yield (QE) changes.

The PL measurements and QE calculation were conducted at two excitation wavelengths (397 and 420 nm) in four TOP-toluene solutions (1.0-9.6 %, w/w). As a result, two types of emission wavelengths were detected, indicating band-gap emission (BGE, 448-451 nm) and longer wavelength emission (LWEs, 470-490 nm).

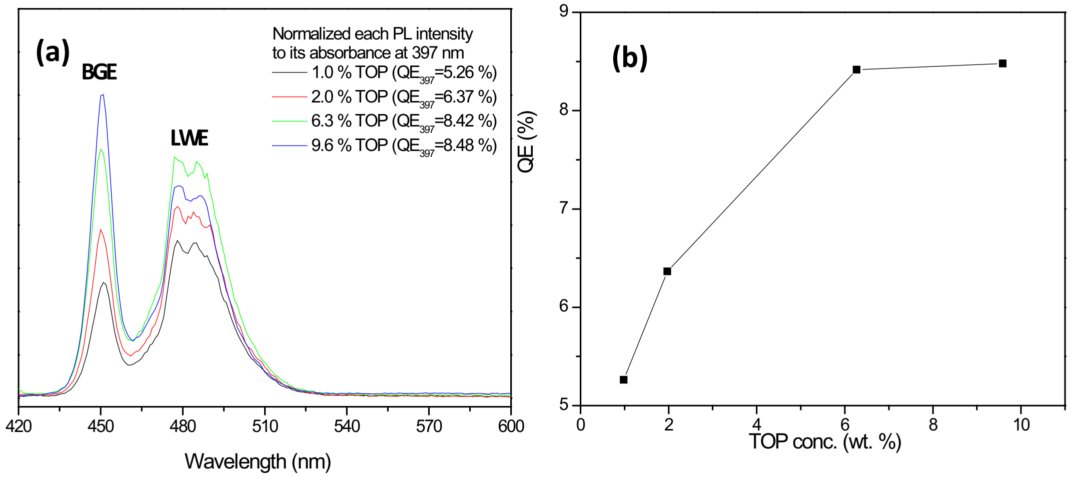

Figure 2.7 Dependence of photoluminescence (PL) and quantum efficiency (QE) on different tri-*n*-octylphosphine (TOP) concentrations in toluene. (a) Band-gap and other longer wavelength emissions were collected in 1.0 %, 2.0 %, 6.3 % and 9.6 % TOP-toluene solution. (b) A correlation of different QEs in TOP solution, accordingly from (a).

The TOP effect was demonstrated by QE changes ($\mathrm{PL}_{\mathrm{BGE}} + \mathrm{PL}_{\mathrm{LWE}}$) and PL changes ($\mathrm{PL}_{\mathrm{BGE}}/\mathrm{PL}_{\mathrm{LWE}}$ ratios). In Figure 2.7 (b), the QB QEs enhanced as the TOP concentration increased. The QE reached a plateau regime when TOP-solution 3 (6.3 %, w/w) was used. In Figure 2.7 (a), the TOP-CdSe QBs exhibited two strong emission bands, BGE and LWE. At the lowest TOP concentration (1.0 %, w/w), LWEs dominated the total PL intensity. As the TOP concentration was increased, BGE and LWE intensity were enhanced differently. TOP-solution 3 (6.3 %, w/w) seemed to be an optimal TOP concentration giving the highest BGE/LWE intensity ratios among all TOP solutions.

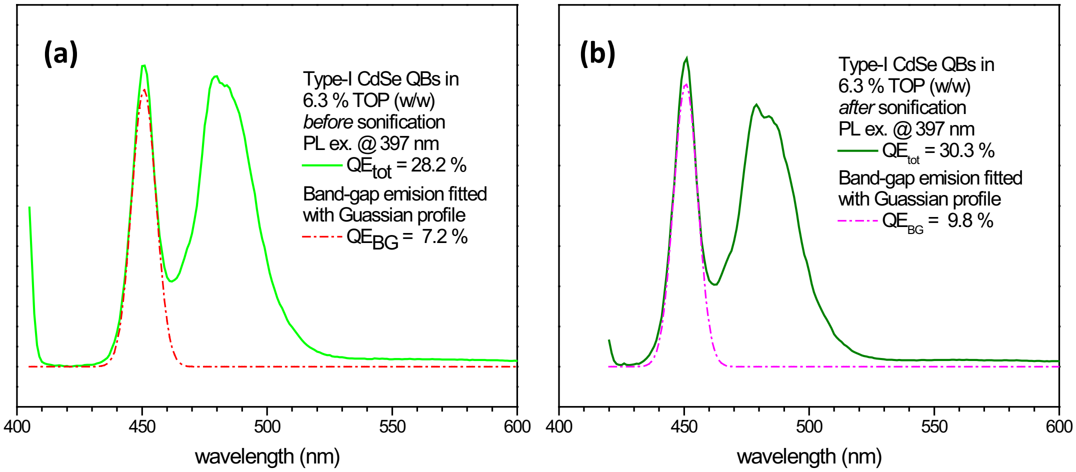

Figure 2.8 Sonication effect on type-I CdSe QBs in 6.3 % (w/w) TOP-toluene solution. (a) Photoluminescence (PL) emission before sonication. (b) PL emission after 3-min sonication. The total PL and Gaussian-fitted PL were plotted in solid and dot-dash curves, respectively.

Sonication was observed to enhance the QE from BGE. The TOP-purified type-I CdSe QBs were re-dispersed in 6.3 % (w/w) TOP-toluene solution. In Figure 2.8, the QE was initially 28.2 % after a standard purification process. In Figure 2.8 (a), the BGE QE was estimated to 7.2 % on the basis of PL intensity area under the Gaussian profile. After a 3-min mild sonication, the total QE slightly increased from 28.2 % to 30.3 % while band-gap QE also increased from 7.2 % to 9.8 %, according to the absorbance at 397 nm. Without an unlikely ligand change or unbundling process, the increment from the total QE (30.3 % - 28.2 % = 2.1 %) should directly come from the BGE enhancement (9.8 % - 7.2 % = 2.6 %), indicating a better TOP-passivated surface.

Adding TOP-purified CdSe QBs into an *n*-oleylamine (*n*-OLAm)-toluene solution changed the surface passivation and led to significantly enhanced total QE. The quantum efficiency (QE) for TOP-purified CdSe QBs was 7.34 % in Figure 2.9 (a, black curve).

After re-dissolving into *n*-oleylamine-toluene solution, the QE dramatically jumped to 28.0 %. However, such a high QE was unstable and quickly decayed to 14.8 % after a mild sonication for 10 min. Instead of sonication, annealing at high temperature (120 °C) also decreased the QE to 14.8 % which was shown in Figure 2.9 (a, green curve).

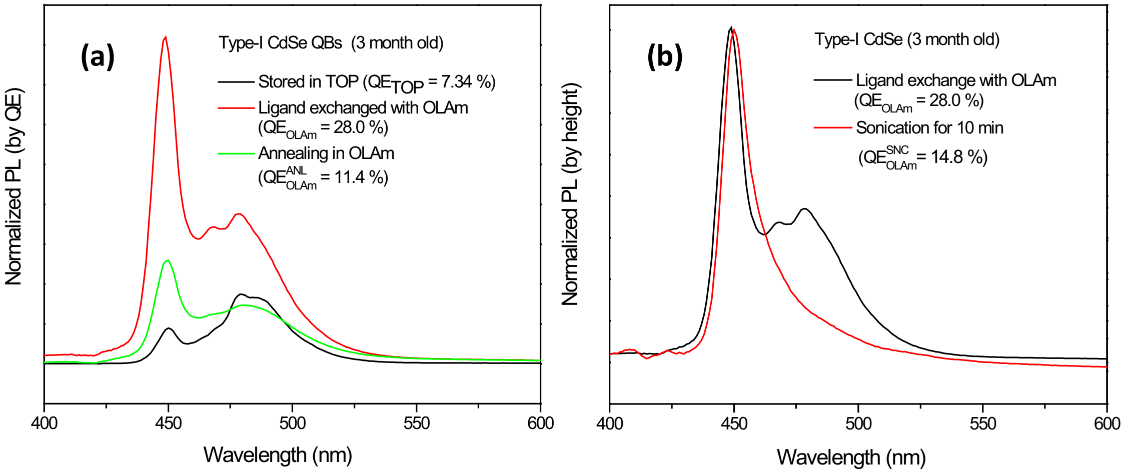

Figure 2.9 Ligand effect on type-I CdSe QB PL. (a) Quantum efficiencies (QE) for the CdSe QBs in TOP (7.34%), in *n*-oleylamine (OLAm, 28.0%) and annealed in *n*-OLAm-toluene solution (11.4 %). (b) QEs for the CdSe QBs in *n*-OLAm (28.0%) and after sonication for 10 min (14.8 %).

Sonication led to unbundling (section 2.2.5). During the unbundling process, the QE experienced first enhancement and then bleaching. In Figure 2.10, TOP-purified CdSe QBs exhibited an initial QE of 10.3 % (the first black square). Upon addition of *n*-oleylamine the QEs increased to 15 ± 5% (19 %, the first red dot) and after sonication increased further to 30 ± 10% (22-28 %, second black square and red dot). However, the optimized QE (> 20 %) was unstable, and decreased upon prolonged exposure to oleylamine (with a timescale of days), exposure to air (with a timescale of hours), and exposure to light and air (with a timescale of minutes). The optimized QB QEs were considerably larger than those previously reported for the analogous CdSe nanoribbons (1-2%).[11]

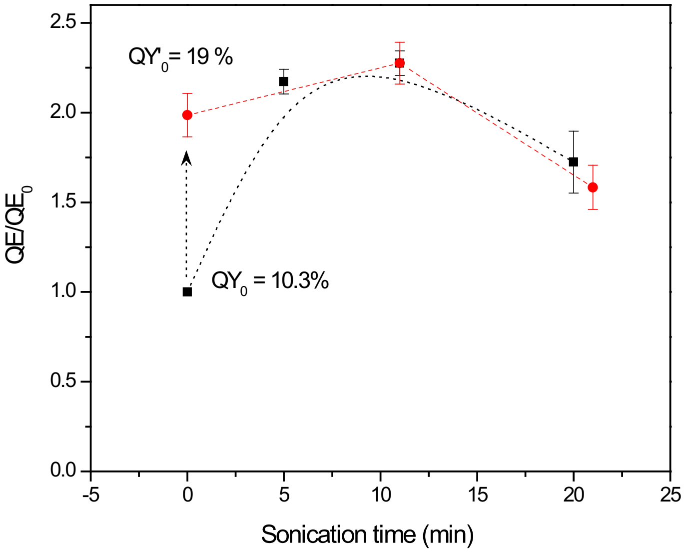

Figure 2.10 Quantum efficiency (QE) of CdSe QBs after a sonication process in oleylamine-toluene solution.

2.2.4 Morphology of CdSe QBs

The proposed belt-like morphology of the nanostructures was therefore confirmed by several forms of evidence. The HRTEM images closely resembled those of the analogous CdSe nanoribbons previously reported by Hyeon.[8, 11] In the images, the nanostructures exhibited two distinct spatial dimensions corresponding to the thicknesses (Figure 2.11c) and widths (Figure 2.11a and b) of the belts. The broad top/bottom and thin edge surfaces indexed to $\{11\bar{2}0\}$ and $\{1\bar{1}00\}$ faces, respectively, which are geometrically orthogonal. Finally, the quantum-well-like extinction spectra confirmed 1D confinement, and therefore that the nanostructures possessed only a single thin dimension. Consequently, the nanostructures were QBs.

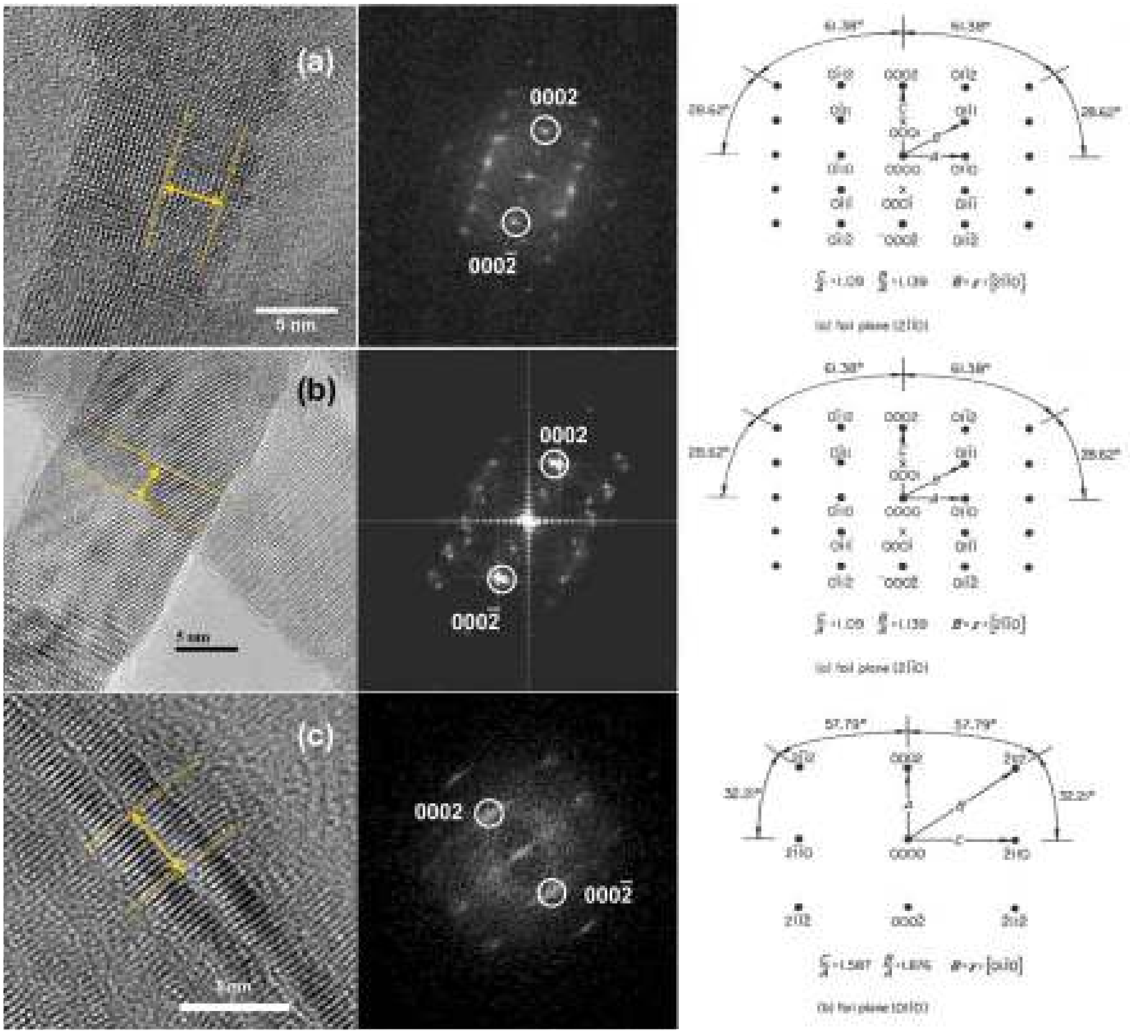

Figure 2.11 HRTEM images of CdSe QBs (left), fast Fourier transforms of the images (center), and indexed diffraction patterns for hcp structures (right).[17] Images a and b are taken normal to the broad top and bottom QB faces, and image c is focused on the thin edges of two stacked QBs. The $(11\bar{2}0)$ image plane for a and b is confirmed by the diffraction patterns in the Fourier transforms, and specifically by the near extinction of the 0001 and $000\bar{1}$ diffraction spots (the residual intensity results from double diffraction). (The $(11\bar{2}0)$ and $(2\bar{1}\bar{1}0)$ image planes are members of a crystallographically equivalent set and produce identical diffraction patterns.) The $(1\bar{1}00)$ image plane for c is also confirmed by the diffraction pattern. The long axis of the QBs therefore lies along [0001], and the width dimension lies along $[1\bar{1}00]$. (a) The yellow lines demarcate 10 lattice fringes along the $[1\bar{1}00]$ direction. (b) The yellow lines demarcate 10 lattice fringes along the [0001] direction. (c) The yellow lines demarcate 10 lattice fringes along the [0001] direction. The HRTEM lattice parameters reported in the text were calculated from these two types of spacing. The values of *c* calculated from images b and c were identical.

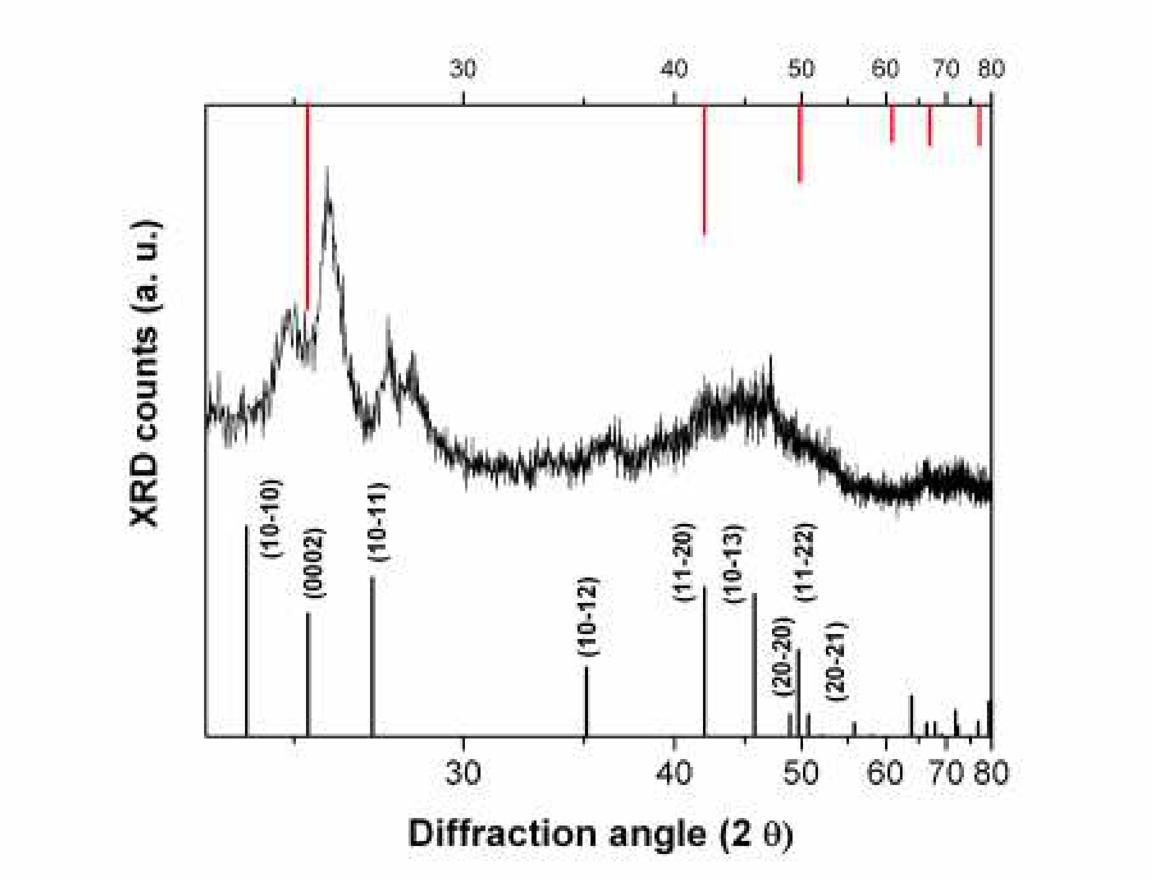

Figure 2.12 An XRD pattern of unbundled CdSe QBs (middle), with reference (stick) patterns for bulk CdSe in the wurtzite (bottom, black) and zinc blende (top, red) structures. A 2θ is used for better viewing of the low-angle reflections. The lattice contraction of 2-3% (see text) causes the shift between the QB and bulk wurtzite patterns. The comparatively sharp 0002 reflection is due to the [0002] crystallographic orientation of the long axis of the QBs, which is thus the largest dimension of the nanocrystals. The lattice parameters *a* and *c* reported in the text were calculated from the $10\bar{1}0$ and 0002 reflections.

The QBs were initially obtained in well-aligned bundles (Figure 2.11c),[8, 11, 15] which were unbundled by mild sonication in the presence of oleylamine in toluene solutions (10 %, w/w, Figure 2.9b, red curve). High-resolution TEM (HRTEM) images of the intact bundles established that the QBs had thicknesses of 1.5-2.0 nm (Figure 2.11c). TEM and HRTEM (Figure 2.11a and b) images of the unbundled QBs established their widths to be 7-15 nm, and their lengths to be 0.5-1.5 μm. XRD patterns of the QBs indexed to a wurtzite crystal structure (Figure 2.12), and Fourier transforms of and lattice spacings in HRTEM images indicated the crystallographic orientation given in Figure 2.11 (left and right columns). The wurtzite lattice parameters were determined to be $a = 4.12 \pm 0.04$ Å and 4.20 ± 0.06 Å, and $c = 6.89 \pm 0.02$ Å and 6.8 ± 0.1 Å by XRD and HRTEM lattice spacings, respectively. These values were smaller than the bulk CdSe lattice parameters ($a = 4.30$ Å, $c = 7.02$ Å) by similar amounts as in the previous report.[11]

2.2.5 Unbundling of CdSe QBs

A belt-like morphology was revealed after unbundling the CdSe QBs. The bundled nature of these CdSe QBs was different to prove because their thickness dimension preferentially laid upon a TEM grid. Therefore, the hidden width dimension required a complicated technique to tilt the sample or a facility for a microtome preparation. By manipulating the surface with long chain ligands, the unbundling process occurred and QBs with width dimension were directly observed by the TEM

Oleylamine (OLAm) unbundled the QB due to its long carbon chain and an amine group. After a mild sonication for 5-10 min, some QBs were unbundled. A single (or few stacks of) QB(s) were observed with their increased thickness dimension preferentially laid upon a TEM grid. In Figure 2.13 (b), a representative TEM image gave the layer-to-layer distance around 42-50 Å. This value is significantly larger than the averaged d_{100} (26.5 ± 0.4 Å) of the annealed CdSe QBs calculated by XRD (Figure 2.14a). During this procedure, a wider dimension (width, 7 ± 2 nm) emerged in the TEM image (Figure 2.13c), accompanying with an aggregation of nanoparticles (dark images) after a prolonged sonication time (20 min, Figure 2.13d).

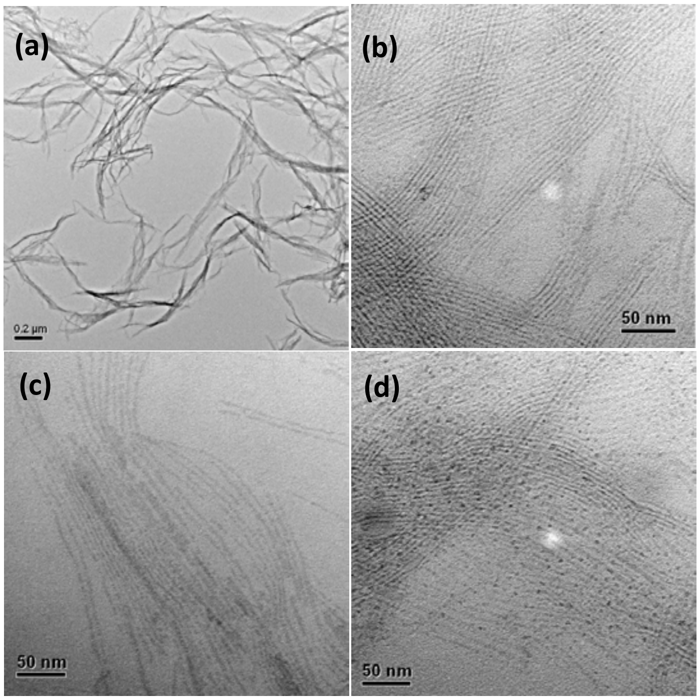

Figure 2.13 Representative TEM images of CdSe QBs upon unbundling. (a) Annealed CdSe QBs after a TOP-purification process. Then, the QBs were sonicated in an oleylamine-toluene solution for 5 min (b), 11 min (c), and 20 min (d).

A layer-to-layer (*d*-spacing) expansion was observed after ligand exchange with OLAm. Such expansions observed in TEM images varied as a result of specific purification processes for a TEM grid preparation. In the contrast, a more reliable result was obtained from XRD patterns. As-made CdSe QBs exhibited an averaged 27 ± 4 Å from two *d*-spacings, as shown in Figure 2.14 (a). OLAm-exchanged CdSe QBs exhibited an averaged 42 ± 4 Å from two *d*-spacings, as shown in Figure 2.14 (b). The increment d-spacing of 15Å (42 Å– 27 Å) principally indicated the length difference between *n*-octylamine and oleylamine.

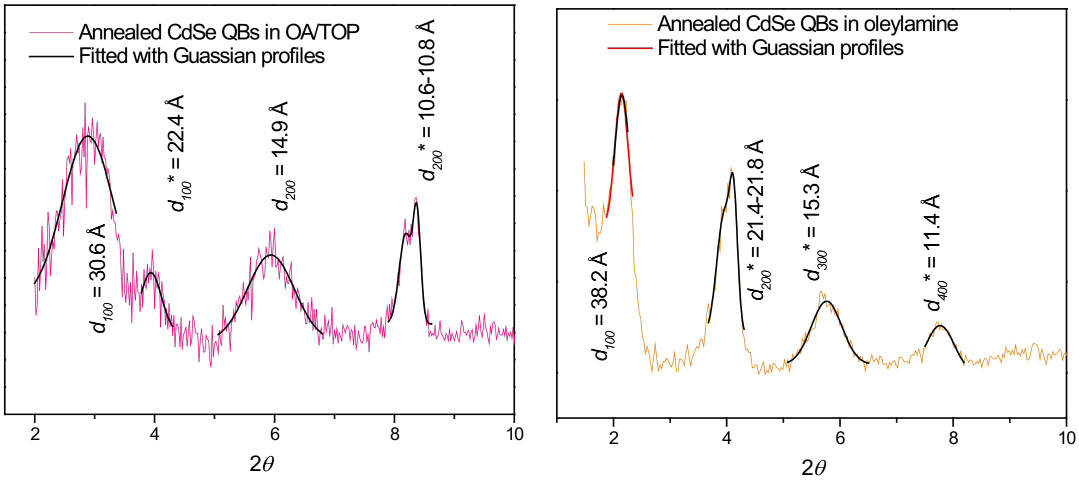

Figure 2.14 XRD of type-I the CdSe QBs before and after ligand exchanges in oleylamine. (a) Two sets of *d*-spacings, 30.6 Å and 22.4 Å, for annealed CdSe QBs purified from octylamine (OA) / tri-*n*-octylphosphine (TOP) mixture. (b) Two sets of *d*-spacings, 38.2 Å and 45.6 Å, for annealed CdSe QBs after ligand exchange in *n*-oleylamine (*n*-OLAm)-toluene solution with sonication.

1-Decanothiol (1-DT) also unbundled the CdSe QBs at higher temperature (139-150 °C). Sonication was not required for high-temperature unbundling process. In Figure 2.15, only unbundled QBs were observed in the TEM images. The thiol-passivated QBs exhibited darker edges enclosing their original belt-like shapes. In addition, a smaller length dimension was observed in the DT-annealed QBs in comparison length dimension (~1 μm) of as-made bundled QBs. Therefore, a completely unbundled CdSe QBs led to a length shrinkage and a curved surface (darker peripheral lines), implying a high surface energy for these DT-annealed QBs.

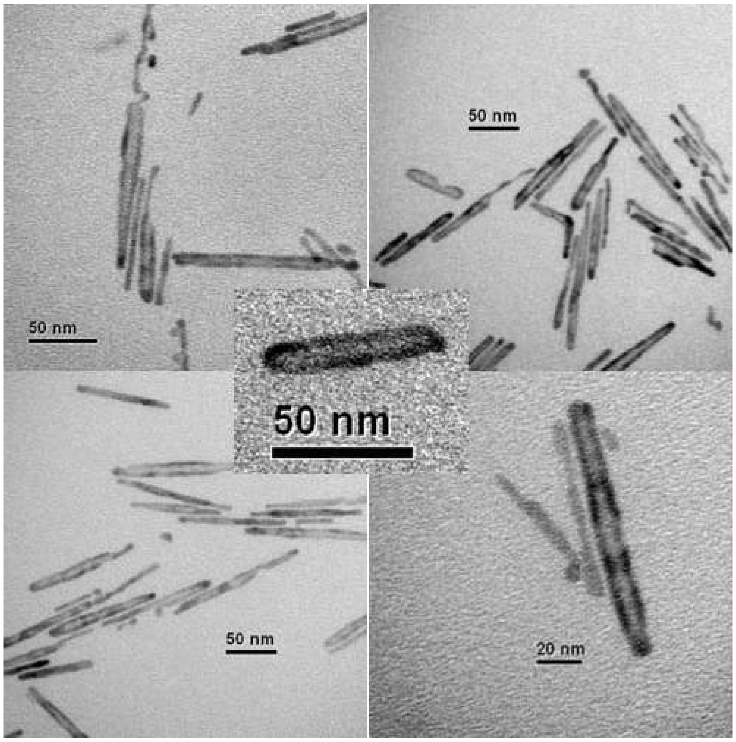

Figure 2.15 Representative TEM images of CdSe QBs upon unbundling process in hot 1-dodecanthiol-toluene solution (>140 ^{o}C).

2.3 Discussion

2.3.1 Origins of ultra-small CdSe quantum structures

Ultra-small quantum structures (dimension < 2.5 nm) are attracting increasing attention for their optical properties and synthetic methods.[18] CdSe nanoclusters, nanobelts, and nanowires of ultra-small sizes are all made under amine-based conditions at low temperature ranges (20-120 °C) [8, 11, 13, 18-19] During their syntheses, magic-sized CdSe clusters are observed as intermediates for larger size nanoparticles,[18-19] nanobelts,[8,]

[11] and even nanowires.[13] Oriented attachment is used as a model for a sequential growth within a small dimension.

The standard oriented-attachment mechanism as proposed for formation of nanowires cannot account for the formation of the QBs discussed here. In the case of nanowires, nanoparticles of a given diameter attach to give nanowires of nearly the same diameter. However, $(CdSe)_{13}$ nanoclusters were the important precursor unit here, which have a dimension of approximately 1 nm, whereas the thinner type-I belts have a thickness of approximately 2 nm. Therefore attachment of nanoclusters in the thickness dimension as well as the two lateral dimensions is necessary to account for the formation of QBs.

According to our study, CdSe nanoclusters are primary building units for CdSe quantum belts (QBs). There are three strong evidences for this growth mechanism. First, nanoclusters were spectrally observed during the synthesis of the QBs. Second, $(CdSe)_{13}$ nanoclusters can successively transform to the type-I QBs at elevated temperature (Figure 2.16a). Third, as-made type-I QB may disassemble into $(CdSe)_{13}$ nanoclusters under a vigorous sonication conditions (Figure 2.6a. black curve). Apparently, only the $(CdSe)_{13}$ nanoclusters transform into type-I QBs. Although $(CdSe)_{19}$ and $(CdSe)_{33\text{-}34}$ nanoclusters were typically observed intermediates on the pathway to $(CdSe)_{13}$ formation (Figure 2.16), a direct assembly of these larger nanoclusters into QBs, such that $(CdSe)_{13}$ was circumvented, was never observed.

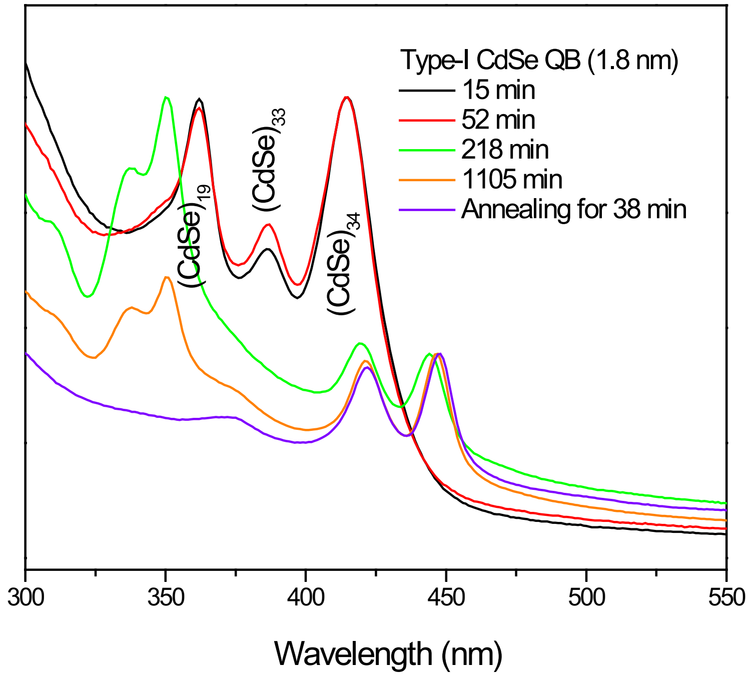

Figure 2.16 The optical transitions for type-I CdSe QBs. A spectral transformation from $(CdSe)_{19\text{-}34}$, to $(CdSe)_{13}$, and then type-I CdSe QBs.

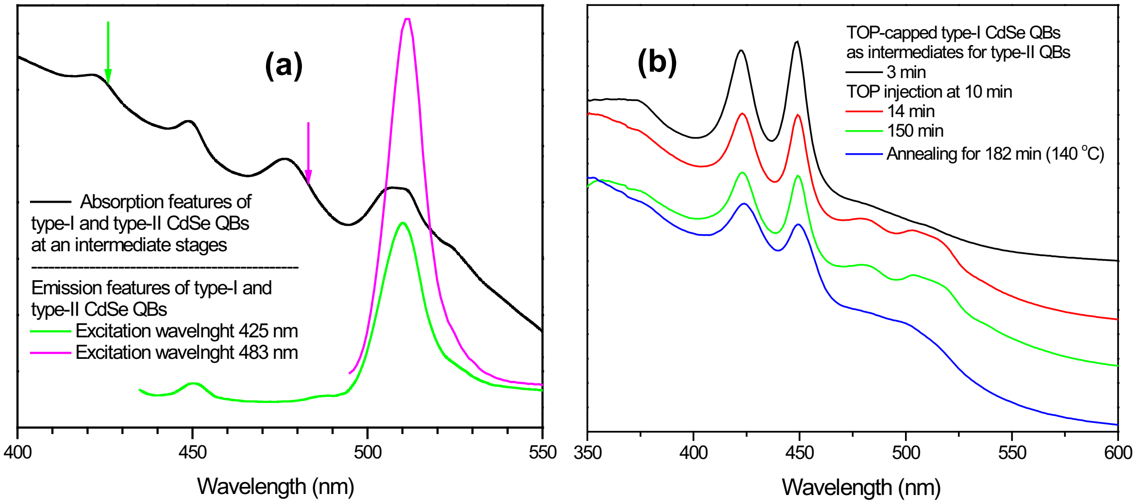

Figure 2.17 The optical property transitions for type-II CdSe QBs. (a) A spectral transformation from type-I CdSe QBs to type-II CdSe QBs. Two photoluminescence emissions indicated QBs of two thicknesses co-existing during the morphology transformation. (b) An interrupted transformation of type-I CdSe QBs in the presence of TOP.

TOP inhibited the transformation from type-I to type-II CdSe QBs. The type-II CdSe QBs (2.5-3.0 nm) were synthesized at 120 ºC and were usually annealed up to 140 ºC. At 120 ºC, nanoclusters of $(CdSe)_{64}$ and $(CdSe)_{33-34}$ and type-I QBs, were observed as the intermediates for the type-II CdSe QBs (Figure 2.3b, 12-90 min). In a controlled experiment, four sharp absorption peaks and two strong PL peaks were simultaneously observed at an intermediate stage (Figure 2.17a). However, when TOP was injected prior to this stage (10 min in Figure 2.17b), the reaction was immediately quenched. No color or spectral change after longer reaction time and annealing was observed after TOP addition. These are direct evidences of the intermediacy of type-I CdSe QBs (greenish-yellow) for type-II QBs (orange).

2.3.2 Growth mechanism of CdSe QBs

Amine templates provide an excellent host for CdSe nanocluster arrays (NCAs). At elevated temperature, multiple attachment directions lead to morphology transformations with controllable dimensions. Surprisingly, quantum belts (QBs) were not originally predicted to be the most thermodynamically stable product.[12] This indicates that the driving force for the QB formation was a little different from the conventional attachment process. I propose that this is a “Temperature-Induced Growth in Templates” (TIGHT) process for small-nanocluster attachment inside a template. Conventional oriented attachment focus on the dislocation (surface or lattice defects) which induces crystal growth via self-organization of adjacent particles, and reduction of overall surface energy after bonding.[20] However, such an attachment is not perfect and grain boundaries still exist within the non-perfect resulting crystals.

There are few differences between TIGHT and the conventional oriented-attachment process. First, the TIGHT process is a kinetic-driven process (dominated by temperature), rather than a thermodynamic-driven process (final stable products). Second, the dimension (thickness) is quantized by the magic-sized clusters, the assembly of which is temperature dependent. Third, the TIGHT process maintains the original template structure during the attachment which leads to the QB morphology. Last, the QBs made by TIGHT maintain their hierarchical structures (bundled forms) until the surface ligands are changed. The CdSe QBs made by the TIGHT process are fairly stable in the presence of amine or phosphine ligands.

2.3.3 Thickness determination

Extinction spectra from dispersions of unbundled CdSe QBs were given in Figure 2.18. These and other spectra collected from the QBs are very similar to those previously reported for CdSe nanoribbons,[11] nanoplatelets,[10] and nanosheets,[8] all of which have thicknesses comparable to the QBs studied here, and thus have only one strongly confined dimension (smaller than the exciton Bohr radius of 5.4 nm[21] for CdSe). Therefore, analogously to Ithurria and Dubertret,[10] we assigned the three absorption features (from lower to higher energy) to 1_B-1_e, 1_A-1_e, and 2_B-2_e quantum-well transitions, respectively ($A \equiv$ light hole, $B \equiv$ heavy hole, and $e \equiv$ electron).[22] (The light-hole and heavy-hole bands in hexagonal semiconductors are typically labeled A and B, respectively.[23])

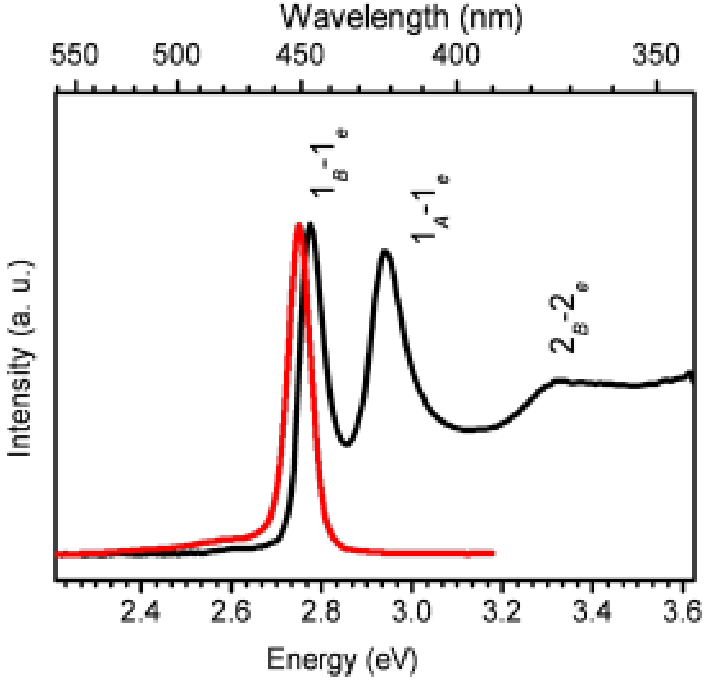

Figure 2.18 Extinction (black) and emission (red) spectra from dispersion of unbundled (b) CdSe QBs. The absorption features are assigned according to the text.

$$E_n = E_g + \frac{h^2 n^2}{8t^2}\left[\frac{1}{m_e^*} + \frac{1}{m_h^*}\right] - 4E_b^{bulk} \qquad (2.1)$$

The energies (E_ns) of wurtzite CdSe quantum-well transitions may be calculated to first order using an overly simple effective-mass-approximation, particle-in-a-box (EMA-PIB) model (eq 1),[8,21,22,24] where E_g is the bulk band gap (1.751 eV),[23] h is Planck's constant, n is a quantum number, t is the well thickness, m_e^* is the electron effective mass ($0.12m_0$),[24] m_h^* is the hole effective mass (m_B^* = $0.90m_0$, m_A^* = $0.45m_0$),[21] E_b^{bulk} is the bulk exciton binding energy (14.8 meV),[25] and m_0 is the free electron mass. This model suffers from the standard EMA assumptions of isotropic, nondegenerate bands and parabolic band shapes.[21] As written in eq 2.1 it assumes infinite-potential barriers at the quantum-well surfaces,[22] it neglects the crystal-field splitting of the A and B bands (bulk value[23] Δ_{cf} = 39 meV), and as applied here it assumes bulk values for the carrier effective masses. As such, the model is quite approximate. Even so, good fits to the energies of the first two transitions in Figure 2.18 were obtained from eq 2.1 using a well thickness of t = 1.80 nm, central to the range experimentally determined by TEM (t = 1.5-2.0 nm). The 1_B-1_e transition was calculated at 2.79 eV, and the 1_A-1_e, transition at 2.95 eV, very close to the energies experimentally observed (Figure 2.18). However, the energy calculated by eq 2.1 for the 2_B-2_e transition (6.08 eV) was far from the feature assigned to the 2_B-2_e transition in Figure 2.18, as expected due to the crudeness of the theoretical model.[21,22] Therefore, the extinction data, and their similarity to those previously reported for CdSe nanoribbons,[11] nanoplatelets,[10] and nanosheets,[8] established that the CdSe QBs exhibited the quantum-confinement effects expected of quantum wells,[10] and were thus 1D-confined systems.

According to the EMA, electrons, holes, and excitons in spherical nanoclusters experience 3-D confinement, which is stronger than the confinement imposed by larger nanoparticles (3-D), nanowires (2-D), and quantum belts (QBs, 1-D). First exciton energies of small CdSe nanoparticles, nanoclusters, and quantum belts (QBs) are plotted in Figure 1.19 in comparison with their sizes and spectral features wavelengths. Surprisingly, the confinement energies of both type-I (t = 1.5-2.0 nm) and type-II (t =

2.5-3.0 nm) QBs fall into a similar energy (or wavelength) regime as CdSe nanoclusters or nanoparticles of the same dimension. This result is likely due to the breakdown of the simple EMA model at these very small nanostructure sizes.

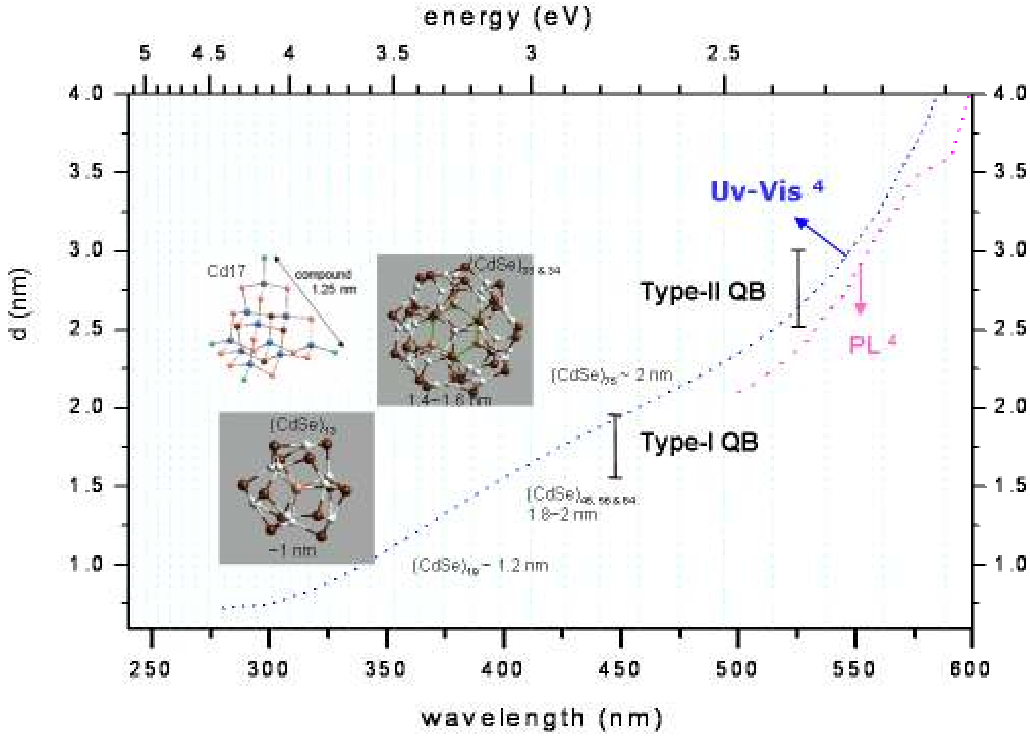

Figure 2.19 Plotting the sizes of various CdSe nanoparticles and nanoclusters (< 2.5 nm) with their absorption (blue dot line) and emission (magenta dot line) wavelengths.

2.3.4 Unbundling by ligand substitution

The unbundling process was conducted by either *n*-oleylamine (*n*-OLAm) or 1-dodecanethiol (1-DT). The purpose of engineering the unbundling process is to reveal the belt-like morphology of the QBs. Unbundling processes are conditionally modified due to reactivity and chain lengths of different ligands.

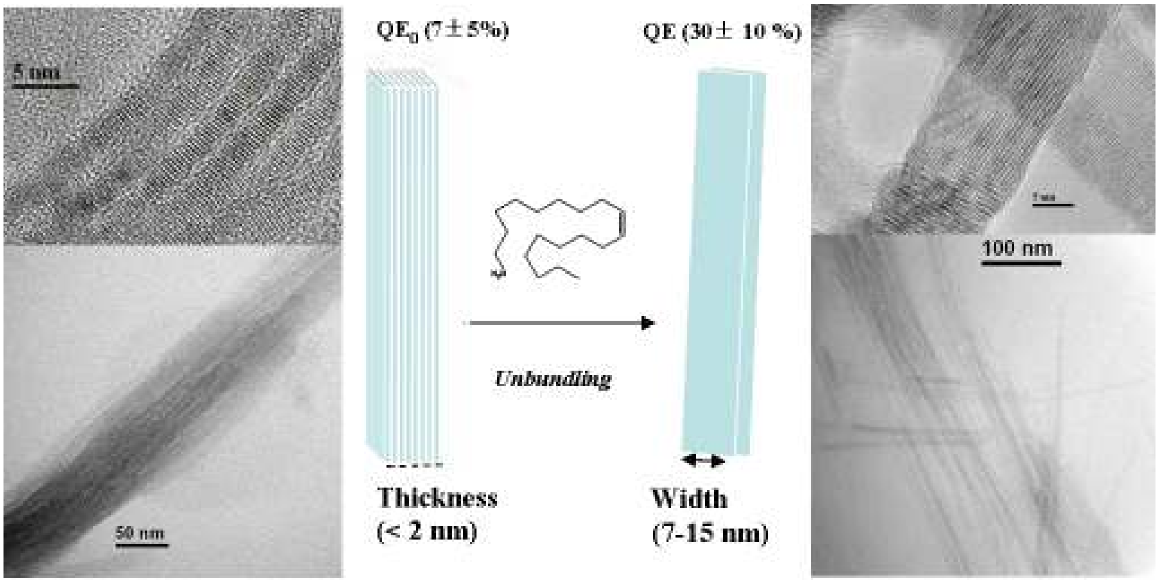

Scheme 2.2 A schematic of an unbundling process for type-I CdSe QBs in the presence of *n*-oleylamine.

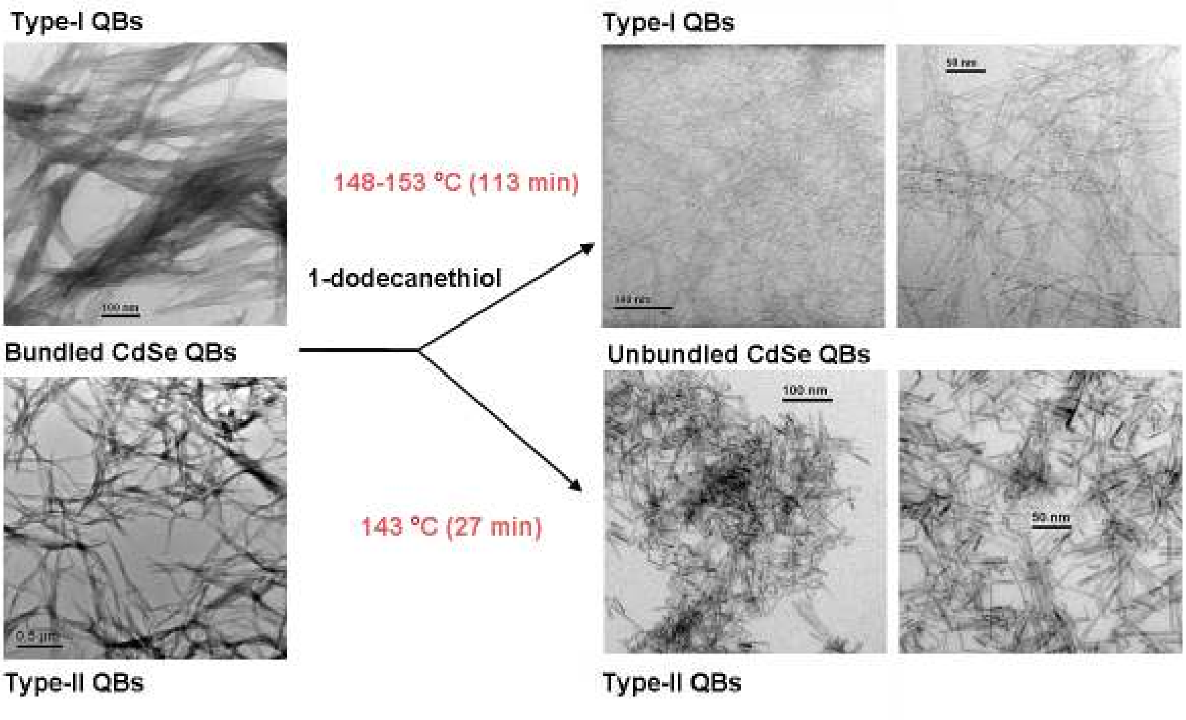

Scheme 2.3 A schematic of an unbundling process for CdSe QBs (type-I and type-II) in the presence of 1-dodecanethiol.

Sonication or high temperature expedites an unbundling process for QBs. Amine-based ligands unbundled the QBs by sonication. After unbundling, the belt-like morphology is revealed by showing the width dimension directly in TEM and HRTEM images (Scheme 2.2, right images). Unbundling also significantly increases the quantum efficiency (QE) of type-I QBs from 7 ± 5 % (as-made) to 30 ± 10 % (unbundled). The deviation in QE is due to different surface passivation and photo-bleaching in the atmosphere.

Thiol-based ligands replace surface octylamine via a strong affinity toward the QB. Under an annealing process at higher temperature (143-153 °C, Scheme 2.3), long carbon-chains repel each other and consequently unbundles the QBs. After annealing, the type-II QB images (Scheme 2.3, bottom) are clearly darker than type-I QB images (Scheme 2.3, upper), indicating a thickness difference. Unfortunately, these thiol-passivated QBs trap excitons (non-radiative recombination) and no appreciable PL or QE is observed. The unbundling by amines or thiols is employed for practical imaging of belt-like morphologies (thickness < width << length) by TEM and HRTEM.

2.4 Conclusions

CdSe quantum belts (QBs) having two discrete thicknesses are synthesized from cadmium acetate and selenourea in *n*-octylamine at different temperatures. Type-I QBs with a thickness of 1.5-2.0 nm are made from $(CdSe)_{13}$ nanoclusters. Type-II QBs with a thickness of 2.5-3.0 nm are converted from the type-I QBs. The two CdSe QB types have unique absorption features which are spectrally similar to quantum-well structures.

Unbundling processes with *n*-oleylamine or 1-dodecanethiol also directly reveals the pseudo two dimensionality of the QB morphology.

2.5 Experimental Sections

2.5.1 Materials

n-Octylamine (*n*-OA) from Aldrich (+99%, product #: O5802-500G) and Alfa Aesar (99%, product #: B24193), selenourea (99.9%, metal basis) from Alpha Aesar, $Cd(OAc)_2{\cdot}2H_2O$ (Aldrich), oleylamine (or cis-9-octadecenylamine) from TCI (> 40.0% by GC) and Sigma-Aldrich (technical grade, 70%) were used as received, and stored under N_2. 1-Dodecylamine (DDA, 98% from Alfa Aesar), tetraoctylammonium bromide (TOABr, ≥ 98% from Fluka, product #: 88000) and ethyl alcohol (EtOH) from PHRAMCO-AAPER (95%, USP grade, product #: E190) were used as received. Toluene from Sigma-Aldrich (CHROMASOLV®, for HPLC, ≥ 99.9%) was purged with dry N_2 for at least 1 h and stored under N_2 prior to use.

2.5.2 Synthesis of type-I CdSe QBs

All synthetic procedures were conducted under dry N_2. Type-I CdSe QBs were synthesized by a modification of the procedure of Peng and coworkers.[REF] A Schlenk flask was charged with $Cd(OAc)_2{\cdot}2H_2O$ (72 mg, 0.27 mmol) and *n*-OA (6.3 g, 48 mmol) and transferred to a 65-68 °C oil bath for 1 h with stirring. In a glove box, a solution of selenourea (58 mg, 0.47 mmol) in *n*-OA (1.35 g, 10.4 mmol) was prepared in a septum-capped vial. Vigorous sonication (10-15 min) was required to dissolve all the selenourea, which was accompanied by a color change from colorless to pink or reddish-brown (light-exposed). This solution was immediately injected into the Schlenk flask held at 65 °C. In various trials the reaction stoichiometry was adjusted to provide Se/Cd ratios in the range of 1.68-1.74.

The reaction proceeded with color changes from colorless (0 min) to yellow, orange (viscous), and then to greenish yellow (3-4 h). Stirring was continued (18-24 h) at 63-68 °C, followed by stirring at an elevated temperature (90-110 °C) for 1 h. The resulting CdSe QBs formed a greenish-yellow suspension mixed with a black precipitate, characterized as elemental selenium by XRD. The elemental Se was removed by injecting TOP (0.5 mL) in N_2-purged toluene (10 mL) into the flask. The suspension of bundled QBs was then stored at room temperature under N_2 for subsequent analyses.

2.5.3 Synthesis of type-II CdSe QBs

All synthetic procedures were conducted under the same general conditions used for type-I QB synthesis. Type-II CdSe QBs were synthesized by a modification of the procedure of Peng and coworkers.[13] A Schlenk flask was charged with $Cd(OAc)_2 \cdot 2H_2O$ (72 mg, 0.27 mmol) and *n*-OA (6.3 g, 48 mmol) and transferred to a 118-122 °C oil bath for 1 h with stirring. In a glove box, a solution of selenourea (58 mg, 0.47 mmol) in *n*-OA (1.35 g, 10.4 mmol) was prepared in a septum-capped vial. Vigorous sonication (10-15 min) was required to dissolve all the selenourea, which was accompanied by a color change from colorless to pink or reddish-brown (light-exposed). This solution was immediately injected into the Schlenk flask held at 118-122 °C. In various trials the reaction stoichiometry was adjusted to provide Se/Cd ratios in the range of 1.68-1.74.

The reaction proceeded with color changes from colorless (0 min) to yellow, orange (viscous, 3 min), yellow (12 min), and then back to orange (> 91 min). Stirring was continued (18-24 h) at 118-120 °C, followed by stirring at an elevated temperature (138-140 °C) for 1 h. The resulting CdSe QBs formed an orange suspension mixed with a black precipitate, characterized as elemental selenium by XRD. The elemental Se was removed by injecting TOP (0.5 mL) in N_2-purged toluene (10 mL) into the flask. The suspension of bundled QBs was then stored at room temperature under N_2 for subsequent analyses.

2.5.4 Transformation of type-I to type-II CdSe QBs

The transformation was conducted immediately after the synthesis of type-I CdSe QBs. The reaction tube containing the as-made type-I CdSe QBs (without TOP purification) was directly placed in an oil bath for the transformation. After the transformation process with stirring at 145 °C for 1 h, the solution turned dark orange and a small amount of brownish black precipitate formed. The brownish black precipitate was identified as elemental Se by XRD. The original greenish yellow precipitate became orange, which was mainly type-II CdSe QBs. A TOP-toluene solution (2-3 mL, 5-10 %, w/w), was injected to remove excess Se precursor as well as to dissolve elemental Se from the reaction. The colorless clear supernatant was centrifuged again in a bench-top centrifuge for 1-3 min. After repeating the TOP purification and centrifugation for 1-2 times, an orange precipitate was obtained and stored under N_2 for future characterizations.

2.5.5 Purification of CdSe QBs

Both as-made and annealed CdSe QBs (type-I and type-II) were purified with a TOP-toluene solution (5-10 %, w/w) prior to other characterizations. After the TOP-toluene solution (2-3 mL) was injected, the reaction was quenched and the dark red solution quickly turned a colorless clear solution with greenish-yellow (or orange) precipitates settled at the tube bottom. The precipitates were centrifuged in a bench-top centrifuge for 1-3 min. The supernatant was discarded. The purification process was repeated 1-2 times by adding TOP-toluene solution or toluene. The precipitate was referred to as “purified” CdSe QBs. The purified QBs were dispersed into the same TOP-toluene solution and placed on a bench for 2-4 days prior to further analyses.

2.5.6 Unbundling of CdSe QBs by *n*-oleylamine

This procedure includes a combination of purification, ligand exchanges, and unbundling steps. An aliquot (0.2 g) of the annealed CdSe QB suspension prepared by the synthetic procedure above was transferred to a septum-capped vial. A solution of oleylamine (1.5 mL, 10% w/w in toluene) was added, and the vial was shaken vigorously a few times and allowed to stand on the bench top for few hours. During this period most of the QBs settled to the bottom third of the vial as a cloudy suspension. The upper two thirds was clear and greenish yellow (or orange), indicating that this fraction contained some unbundled QBs. The upper, clear fraction (ca. 1 mL) was removed by pipet and set aside or discarded.

The purification procedure was repeated by adding another portion of the oleylamine solution (ca. 1 mL) to the remaining QB suspension in the vial. At this stage, the unbundling process was conducted in two different ways. The unbundling process was expedited to 5-11 min under a mild sonication. Or, as before, the vial was shaken vigorously a few times and allowed to stand on the bench top overnight. During this period the suspension of bundled QBs settled into the bottom two thirds of the vial. The upper, clear, yellow fraction (ca. 0.5 mL) was removed for subsequent TEM analysis. The resulting suspension of partially unbundled QBs was used for spectroscopic analyses on the same day to retain a high PL quantum yield. Dilution of the suspension with oleylamine solution by 10-20× (to ca. 10-20 mL) afforded a clear dispersion of unbundled QBs.

2.5.7 Unbundling of CdSe QBs by 1-decanethiol

The unbundling process was conducted in a mixture of 1-decanethiol and octylamine solution. After the first annealing, another portion of 1-decanethiol (2-3 mL) was injected into a sealed reaction tube (6-8 mL). The precipitate remained in the bottom one-fourth of the reaction volume. Continued annealing of the annealed CdSe QBs (type-I and type-II) proceeded in an oil bath at 139-153 ^{o}C for 0.5-2 h.

At this stage the reaction solution became slightly darker (yellow for type-I QBs, and orange-red for type-II QBs). A small amount of black or gray precipitate was elemental Se that was subsequently removed by a TOP solution. Both thiol-annealed CdSe QBs (type-I and type-II) were purified with a TOP-toluene solution (5-10 %, w/w) prior to other characterizations. After the TOP-toluene solution (2-3 mL) was injected, the reaction was quenched and the dark red solution quickly turned a colorless clear solution with yellow (or orange-red) precipitates settled at the tube bottom. The precipitates were centrifuged in a bench-top centrifuge for 10-15 min. The supernatant was discarded. The purification process was repeated 1-2 times by adding TOP-toluene solution or toluene. The precipitate was referred to as unbundled CdSe QBs. The resulting suspension of unbundled QBs was used for spectroscopic analyses on the same day to retain a high PL quantum yield. Dilution of the suspension with oleylamine solution by 10-20× (to ca. 10-20 mL) afforded a clear dispersion of unbundled QBs.

2.5.8 Absorption spectroscopy

Most spectroscopic analyses of CdSe QBs were conducted in toluene, oleylamine-toluene solution (10-20 %, w/w), or TOP-toluene solution (5-10 %, w/w). The CdSe QBs after purification were redispersed in the same mixture solution, on the same day to retain a high PL quantum yield. Absorption spectra were collected at room temperature using a Varian Cary 100 Bio UV-visible spectrophotometer. The sample absorbance was adjusted to 0.05-0.15 at 350 nm. In each UV-vis spectroscopic analysis, the same background solution, toluene or the mixture solution, was used for the reference and sample. A baseline correction was also applied to account for cuvette absorption. Oleylamine has a strong, sharp absorption at 332 nm, which appeared in the spectra if the oleylamine concentrations in the sample and reference cuvettes were imbalanced, or if the baseline was inadequately corrected.

2.5.9 X-ray powder diffraction (XRD).

At least 2-3 mL of the suspension of as-made or annealed QBs in *n*-OA (from "Synthesis of type-I and type-II CdSe QBs") were required to obtain an XRD pattern. The CdSe QB sample was injected with 1-2 mL of TOP-toluene solution (5-10 %, w/w) to remove excess ligands (*n*-OA) and side products (SeTOP) prior to XRD sample preparation. The QB suspension (3-5 mL) was centrifuged in a bench-top centrifuge for 5 min and the supernatant was discarded. Toluene (2 mL) was added to the QB precipitate, and the mixture was shaken a few times and then centrifuged for 5 min. Most of the supernatant was discarded and toluene (~0.1 mL) was added into the precipitate.

The slush was transferred (cast-coated) onto a glass XRD slide and dried in a fume hood exhausting at high face velocity. Transfer and drying were repeated for 3-5 times, which usually required 1 h to complete. XRD patterns were obtained using a Rigaku Dmax A vertical powder diffractometer with Cu Kα radiation ($\lambda = 1.5418$ Å) and Materials Data Incorporated (MDI) automation and Jade software. The step size was 0.008° and the retention time was 1 sec for both low-angle (1.5-15°) and high-angle (20-65°) measurements.

2.5.10 Transmission electron microscopy (TEM)

For analysis of bundled CdSe QBs, an aliquot from the suspension of as-made QBs (ca. 0.1 mL) was diluted into toluene (1 mL) in air. The mixture was shaken a few times and centrifuged in a bench-top centrifuge for 5 min. This gave a precipitate and a nearly homogeneous supernatant. The supernatant was discarded, and the QB precipitate was re-diluted into toluene (1 mL). The mixture was shaken and then centrifuged as above. The supernatant was again discarded and the QB precipitate was dispersed in toluene (1 mL) to yield a dispersion for subsequent TEM analysis. For analysis of unbundled CdSe QBs, detailed unbundling and purification processes were described in "Unbundling of CdSe QBs by *n*-oleylamine and 1-decanethiol."

A drop of the appropriate CdSe NCA dispersion was transferred onto a carbon-coated Cu grid (Ted Pella, PELCO® 300 Mesh Grids, product #: 1GC300). The solvent on the Cu grid was evaporated in the ambient atmosphere. This process was usually repeated twice to load enough CdSe QBs onto the grid (concentration dependent). TEM images of CdSe QBs were collected using a JEOL 2000 FX microscope with an acceleration voltage of 200 kV. HRTEM was conducted on a JEOL-2100F using TEM grid with holey-carbon film (Ted Pella, Ultrathin Carbon Film on Holey Carbon Support Film, 400 mesh, Copper, product #: 01824).

2.6 References

1. Tang, Z.; Kotov, N. A.; Grersig, M. Science 2002, 297, 237-240.
2. Xu, H.; Wang, W.; Zhu, W. Chem. Lett. 2006, 35, 264-265.
3. Li, R.; Luo, Z.; Papadimitrakopoulos, F. J. Am. Chem. Soc. 2006, 128, 6280-6281.
4. Shen, S.; Zhaung, J.; Xu, X.; Nisar, A.; Hu, Shi, Wang, S. Inorg. Chem. 2009, 48, 5117–5128.
5. Min, Y.; Akbulut, M.; Kristiansen, Golan, Y.; Israelachvili,J. Nature Mater. 2008, 7, 527-538.
6. Tang, Z. Y.; Zhang, Z. L.; Wang, Y.; Glotzer, S. C.; Kotov, N. A. Science 2006, 314, 274–278.
7. Oyler, K.D.; Ke, X.; Sines, I.T.; Schiffer, P.; Schaak, R. E. Chem. Mater. 2009, 21, 3655-3661.
8. Son, J.S.; Wen, X.-D.; Joo, J.; Chae, J.; Baek, S.-I.; Park, K.; Kim, J.H.; An, K.; Yu, J.H.; Kwon, S.G.; Choi, S.-H.; Wang, Z.; Kim, Y.-W.; Kuk, Young, Hoffmann, R.; Hyeon, T. Angew Chem. Int. Ed. 2009, 48, 6861-6864.
9. Yu, T.; Joo, J.; Park, Y.-I.; Hyeon, T. J. Am. Chem. Soc. 2005, 128, 1786-1787.
10. Ithurria, S.; Dubertret, B. J. Am. Chem. Soc. 2008, 130, 16504-16505.
11. Joo, J.; Son, J.S.; Kwon, S.G.; Yu, J.H.; Hyeon, T. J. Am. Chem. Soc. 2006, 128, 5632-5633.
12. Barnard, A. S.; Xu, H.; Li, X.; Pradhan, N,; Peng, X. Nanotechology, 2006, 17, 5707-5714.
13. Pradhan, N.; Xu, H.; Peng, X. Nano Lett. 2006, 6, 720-724.

14. Reihle, F. S.; Bienert, R.; Thomann, R.; Urban, G.A.; Krüger, M. Nano Lett. 2009, 9, 514-518.
15. Liu, Y.-H.; Wayman, V.L.; Gibbons, P.C.; Loomis, R.A.; Buhro, W.E. Nano Lett. 2010, 10, 352-357.
16. Sun, M.; Yang, X. J. Phys. Chem. C, 2009, 113, 8701-8709.
17. Edington, J. W. Practical electron microscopy in materials science; N. V. Philips: Eindhoven, 1976; p 310.
18. Kasuya, A.; Sivamohan, R.; Barnakov, Y.A.; Dmitruk, I.M.; Nirasawa, T.; Romanyuk, V.R.; Kumar, V.; Mamykin, S.V.; Tohji, K.; Jeyadevan, B.; Shinoda, K; Kudo, T; Terasaki, O; Liu, Z.; Belosludov, R.V.; Sundararajan, V.; Kawazoe, Y. Nat. Mater. , 2004, 3, 99–102.
19. Kuçur, E.; Ziegler, J.; Nann, T. Small, 2008, 4, 883-887.
20. Penn, R.L.; Banfield, J. F. Science, 1998, 281, 969-971.
21. Yoffe, A. D. Advances in Physics 1993, 42, 173-266; reprinted in Advances in Physics 2002, 51, 799-890.
22. Dingle, R. Festkörperprobleme 1975, XV, 21-48.
23. Semiconductors – Basic Data, 2nd Revised Edition; Madelung, O., Ed.; Springer: Berlin, 1996.
24. Wang, F.; Yu, H.; Jeong, S.; Pietryga, J. M.; Hollingsworth, J. A.; Gibbons, P. C.; Buhro, W. E. ACS Nano 2008, 2, 1903-1913.
25. Wang, F.; Yu, H.; Li, J.; Hang, Q.; Zemlyanov, D.; Gibbons, P. C.; Wang, L.-W.; Janes, D. B.; Buhro, W. E. J. Am. Chem. Soc. 2007, 129, 14327-14335.

Chapter 3: High Quantum Efficiency and Spectroscopic Studies of CdSe Quantum Belts

3.1 Introduction

PL efficiencies provide a measure of the quality of surface passivation and the scarcity of trap sites that induce nonradiative recombination. Although the ensemble PL efficiencies in CdSe QDs are now routinely >60%,[1-3] those in QRs are lower (20-30%),[4,5] and those previously reported in QWs are disappointingly low (0.1-0.3%).[6-11] Pseudo-1D semiconductor nanocrystals such as quantum wires[12-14] (QWs) and quantum rods (QRs)[12,15] are under active consideration for solar-cell applications because they can in principle transport photogenerated carriers over longer distances and with fewer hopping events than corresponding devices constructed with nanocrystal (colloidal) quantum dots (QDs).[12] However, the increased axial dimension in QRs and QWs allows excitons, electrons, and/or holes to sample a much larger nanocrystal-surface area and thus experience a higher probability for encountering a trap site. Thus, in equally passivated QDs, QRs, and QWs, losses to nonradiative recombination will be highest in the QWs and lowest in the QDs. [9]

Several research groups have demonstrated that nonradiative recombination is greatly suppressed by a core-shell structure. [16-18] Constructing an external shell layer onto the quantum dots (pseudo-0D) eliminates most of defect sites, leading to high PL efficiencies (> 85%).[19-20] However, inhomogeneous core-shell structures of quantum wires (pseudo-1D) routinely posses trap sites, leading to nonradiative recombination process with disappointing low PL efficiencies (< 0.1 %).[21] Recently, pseudo-2D platelets with controllable thicknesses exhibit significant quantum efficiencies, up to ~30 %, comparable to the quantum efficiencies of QRs.[22-23] Even so, Ithurria and Dubertret have not reported the origin of the high PL efficiencies in the quantum-well nanostructures.[22]

In this Chapter, I will report that pseudo-1D CdSe quantum belts (QBs) exhibit uniform photoluminescence (PL) with efficiencies of 30 ± 10 %, indicating a low density of surface-trap sites.[22] Epifluorescence and Au-decoration results demonstrate experimentally that nonradiative traps can be effectively minimized in CdSe QBs, establishing that pseudo-1D semiconductor nanocrystals having an extended axial dimension can exhibit photoluminescence efficiencies competitive with those of QRs, and about half of those of QDs. The results show that pseudo-1D semiconductor nanocrystals can have excellent passivation and optical properties, and effectively transport excitons and presumably charge carriers with minimal losses to non-radiative-recombination pathways.

3.2 Results

3.2.1 Photoluminescence bleaching of as-made CdSe QBs

As-made type-I CdSe QBs have initial quantum efficiencies (QE) of 7 ± 5 % in *n*-octylamine. Without an annealing process, the QBs were structurally fragile toward sonication. In addition, the PL intensities of the as-made QBs changed with time. Sequential PL measurements of the same QBs routinely gave varying PL intensities, indicating a PL bleaching process, similarly to the CdSe platelets reported by Ithurria and Dubertret.[22F] The PL bleaching process also implied surface and/or structural changes during the measurements, specifically for as-made QBs.

In Figure 3.1 (a), PLs gradually decayed in *n*-oleylamine solution during ten consecutive measurements. Each PL measurement took around 1.5 min. After ten PL measurements (15 min), both PL intensities and QEs lost 23 % from their original values. The decreasing curve was nicely fitted to a single exponential decay equation within the first 15 min. Consequently, this exponential relationship indicated a close correlation between the PL bleaching process and the measurement time, which also excluded an intensity fluctuation from the spectrometer.

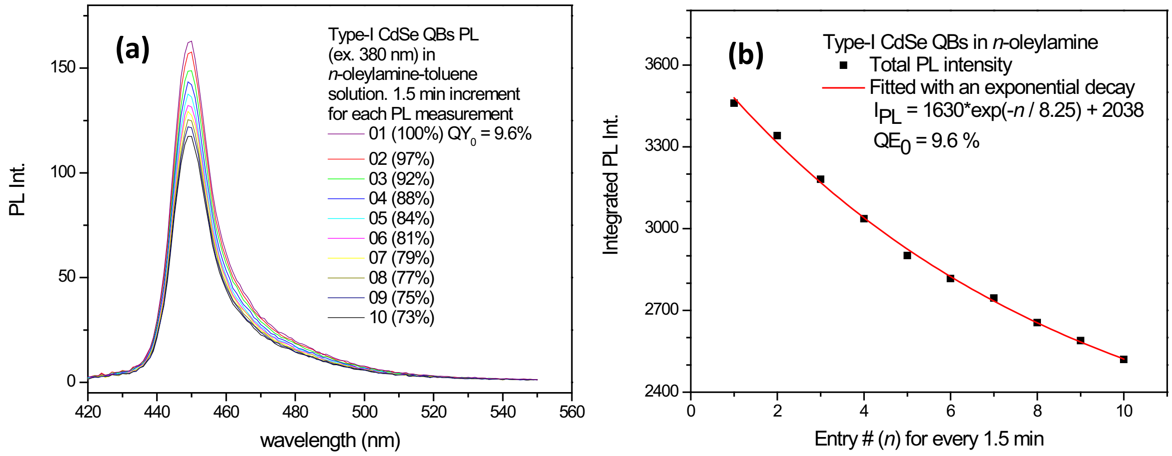

Figure 3.1 Photobleaching of as-made CdSe QBs in *n*-oleylamine solution. (a) Ten consecutive PL emissions for every 1.5 min. (b) Ten consecutive PL intensities for every 1.5 min.

A similar phenomenon was observed for as-made CdSe QBs in toluene. In Figure 3.2 (b), another ten consecutive PL measurements indicated a PL bleaching nature of CdSe QBs in toluene. Each PL measurement took around 1.5 min (90 sec). After ten PL measurements (15 min), both PL intensities and QEs lost 26 % from their original values. The decreasing curve was fitted to a single exponential decay equation within the first 15 min

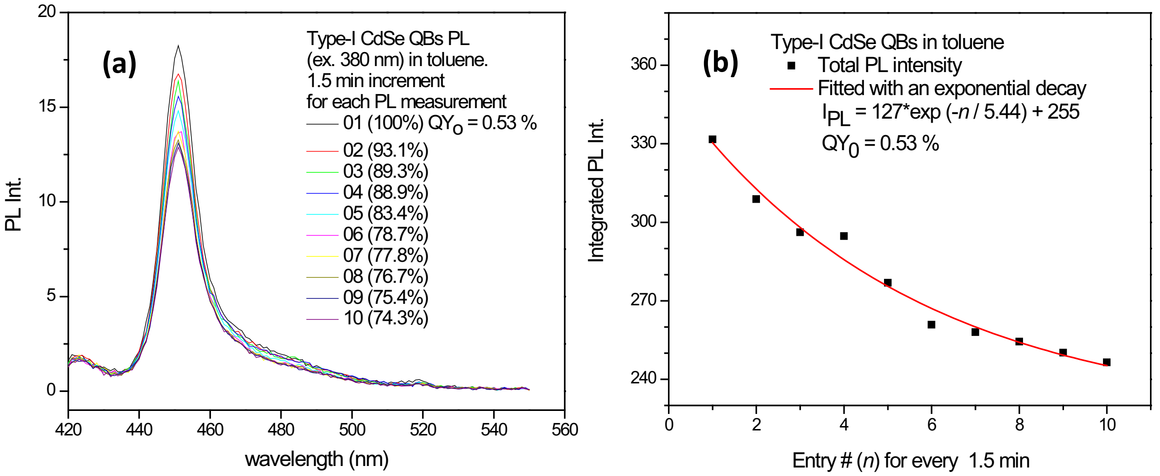

Figure 3.2 Photobleaching of as-made CdSe QBs in toluene solution. (a) Consecutive ten PL emissions after every 1.5 min. (b) Consecutive ten PL intensity after every 1.5 min.

.

Both PL decays were fitted to exponential curves as shown in eq. (3.1). Different decay constant constants (λ), mean lifetime (τ = 1/λ), half lifetime ($t_{1/2}$ = ln2 τ), A constants, and intensity constants (I_0) were obtained from two exponential decay fittings.

$$I_{PL} = A' \exp(-\lambda t) + I_O \quad (3.1)$$

From Figure 3.1(b) and 3.2 (b), a larger intensity constant (I_0) for the QBs in *n*-oleylamine (2038) indicated an intrinsic ligand enhancement of the PL compared to that of the QBs in toluene (255). The values were subtracted from the total PL intensities. The subtracted PL intensities in log scales [$\ln(I_{PL} - I_o)$] followed a linear relationship with measurement time (*t*) as shown in Figure 3.3 and consequently fitted by eq. (3.2).

$$\ln(I_{PL} - I_O) = \ln A - \lambda t \quad (3.2)$$

A longer lifetime for the QBs in *n*-oleylamine ($\tau = 741$ s, $t_{1/2} = 514$ s) indicated a higher bleaching resistance than the QBs in toluene ($\tau = 171$ s, $t_{1/2} = 119$ s).

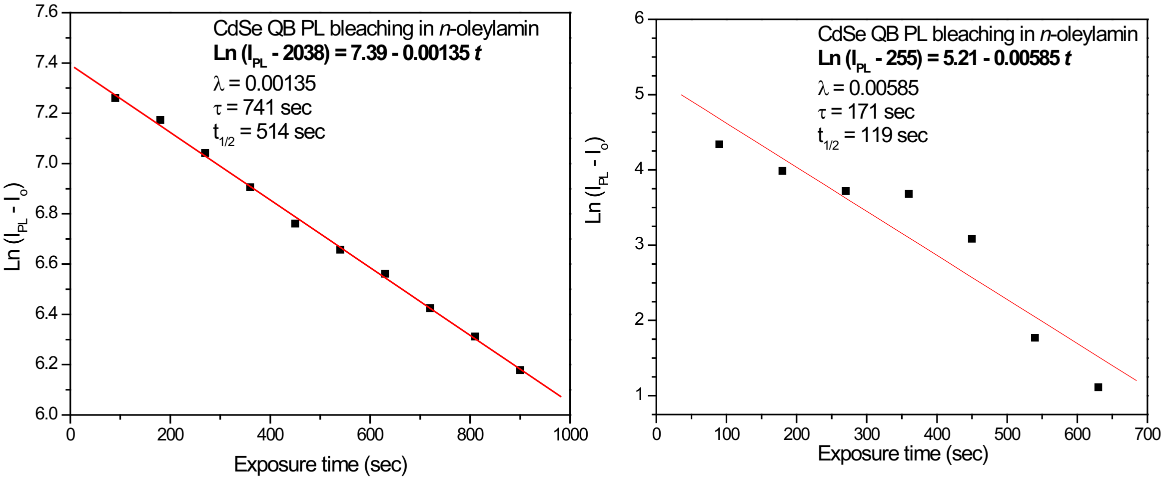

Figure 3.3 Linear plotting of PL decay of as-made CdSe QBs. (a) Ten PL measurements were conducted in *n*-olylamine-toluene solution. (b) Seven PL measurements were conducted in toluene.

In addition to the PL bleaching, we observed structural disassociation in the absorption spectra. In Chapter 2, we observed a disassembly of as-made CdSe QBs into $(CdSe)_{13}$ nanoclusters by vigorous sonication. Here a disassembly of as-made CdSe QBs into $(CdSe)_{13}$ nanoclusters was immediately observed after consecutive absorption and PL measurements (Figure 3.4). An observation of $(CdSe)_{13}$ nanoclusters explained a PL bleaching phenomenon in Figure 3.1 and 3.2. Steady transformation from emissive QBs to non-emissive $(CdSe)_{13}$ nanoclusters, reduced the PL intensity and consequently decreased the total quantum efficiency of the sample.

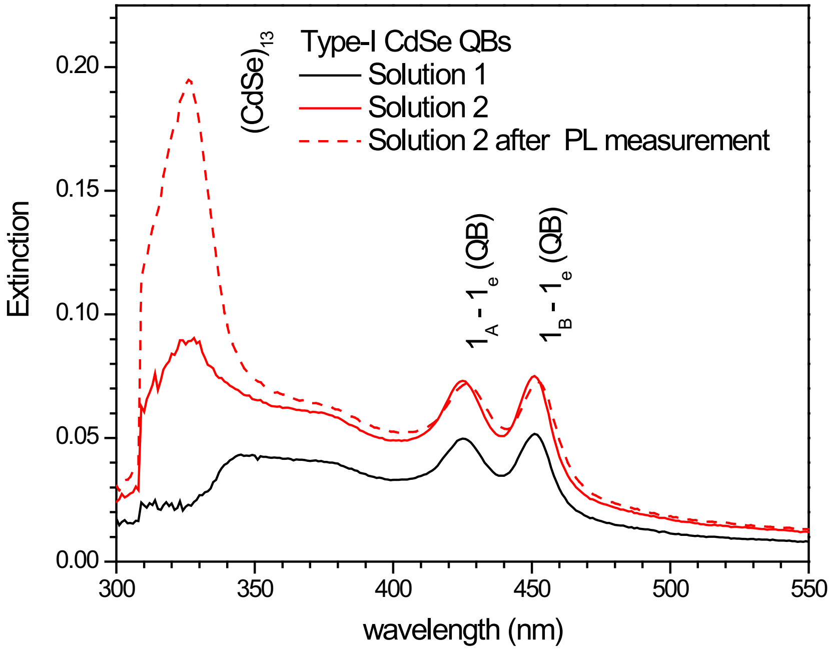

Figure 3.4 Photo-instability of as-made CdSe QBs in toluene. Solution 1 and 2 contained different amounts of TOP-purified QBs without annealing. Emerging peak at 326 nm indicated $(CdSe)_{13}$ nanocluster formation, accompanying with a small red shift to the light-hole (422 → 425 nm) and heavy hole (448 → 451 nm) transitions.

3.2.2 Epifluorescence studies of CdSe QBs

These experiments were conducted by Virginia Wayman, whom we thank. Dispersions of unbundled QBs were deposited onto glass cover slips for epifluorescence microscopy and spectroscopy. Although unbundled, we cannot assert that the resulting images and spectra were obtained entirely from single QBs. Evidence for residual bundles of a few to several QBs was observed in places. As most of the QBs were only slightly longer (0.5-1.5 μm) than the resolution spot size (0.4-0.6 μm), most appeared in the epifluorescence images as slightly elongated features (Figure 3.5a, b). The emission of the QBs did not change appreciably as a function of excitation power density (2.0-320

W/cm^2); however, the QBs began to photobleach rapidly at higher power densities (>150 W/cm^2). The emission spectra collected from various QBs were nearly identical to one another (Figure 3.5c), and comparably narrow (mean Lorentzian FWHM = 48 ± 15 meV) to the ensemble PL described above (mean Lorentzian FWHM = 50 meV). The similarity of the epifluorescence and ensemble PL spectra attests to the thickness uniformity among the QBs in the ensemble specimens.

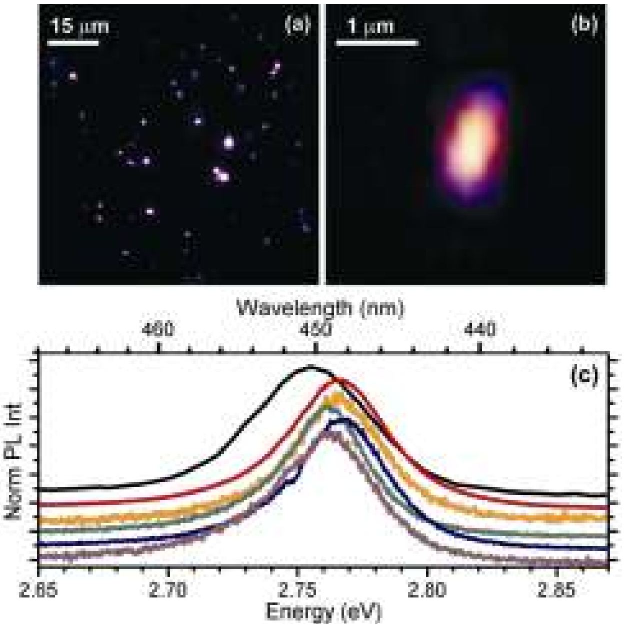

Figure 3.5 a) A wide-field PL microscopy image of unbundled CdSe QBs spin-coated onto a coverslip; (b) a PL microscopy image of a CdSe QB; (c) PL spectra recorded from individual CdSe QBs (various colors) plotted with the ensemble CdSe QD PL spectrum (black) obtained from a solvent dispersion of QBs.

The 2D delocalization of excitons within the QBs was demonstrated by position-selective excitation and epifluorescence microscopy. A long QB (*l* ~ 1.2 μm) was irradiated with a ~425 nm-diameter illumination spot overlapping the center region of the

QB (Figure 3.6a). The resulting PL image revealed intense emission with a PL-intensity profile that fit well to a Lorentzian lineshape with a FWHM of 1.0 µm centered at the point of irradiation, independent of excitation power density. The increase in the breadth of this profile over the experimental spatial resolution, 500-550 nm, is evidence for exciton delocalization, or diffusion.

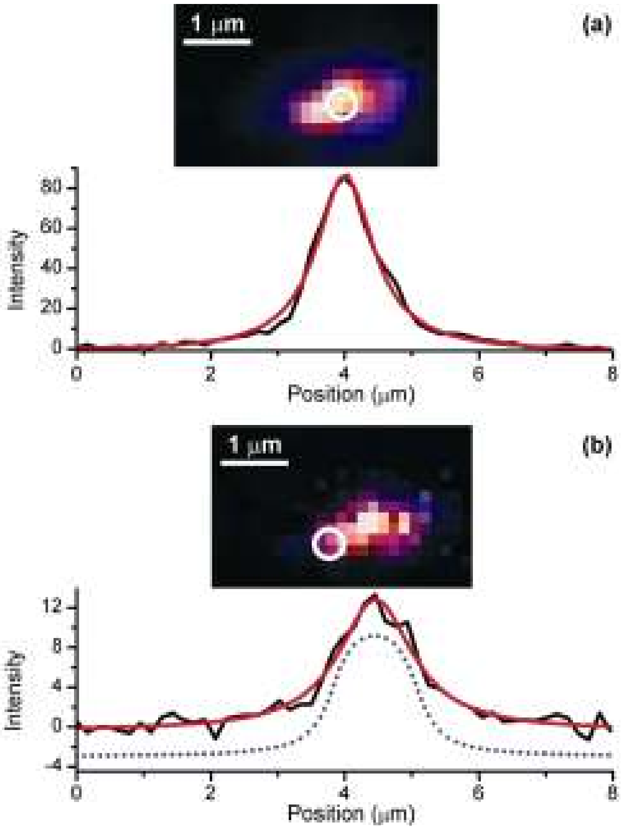

Figure 3.6 PL microscopy images of a CdSe QB illuminated at the (a) center of the QB, and (b) edge of the QB. The white circles represent the positions of the illumination spots. The PL intensity (black) along the length of each QB is shown below each image, with Lorentzian fits to the data (red). The full-widths at half maxima of the Lorentzian fits are 1.0(2) µm and 1.3(5) µm for (a) and (b), respectively. In (b), the dotted curve (blue) represents a convolution of a 1.2-µm length QB with the resolution of a 550-nm Lorentzian (see text).

The emission intensity in the PL image obtained for the same QB decreased as the center position of the irradiation spot was moved to a point just off the end of the QB (Figure 3.5b). However, the maximum PL intensity did not shift toward the end of the QB closest to the irradiation region; rather, it was still observed near the center of the QB. A Lorentzian fit to the intensity profile revealed a FWHM of ~ 1.3 μm, which is more than two times the experimental limit.

The PL-intensity profile for an equal probability of emission along the entire length of a narrow QB should appear as a convolution of the image resolution with a line representing the length of the QB. An emission simulation obtained using a Lorentzian with a FWHM = 550 nm for the image resolution and a continuous, uniform distribution of emission sites along the QB length of 1.2 μm is included in Figure 3.6 (b) as a dotted line. The agreement of the simulation and data suggests a nearly uniform probability for radiative exciton recombination along the entire length of the QB. Low-temperature studies of ZnSe quantum wells have demonstrated quasi-ballistic transport[24] of hot excitons with coherence lengths of 300-400 nm[25] and total propagation lengths of > 1 μm.[26] Accordingly, we interpret our results as indicating the effective delocalization (transport) of 2D excitons over the full span of the individual QBs.

3.2.3 Polarized emissions of CdSe QBs

These experiments were conducted by Virginia Wayman, whom we thank. In Figure 3.7, clear 180 °C oscillation and 90 ° annihilation in the QB emission intensity were seen. Corresponding emission image at selective polarization angles were also provided to illustrate how QB emission images changed with incident polarization angles. Single QW emission intensities were plotted as a function of excitation polarization angles relative to the QB growth direction. The QBs exhibited polarized emission parallel to the elongated dimension of the features, as expected for 1D nanostructures.[27-29]

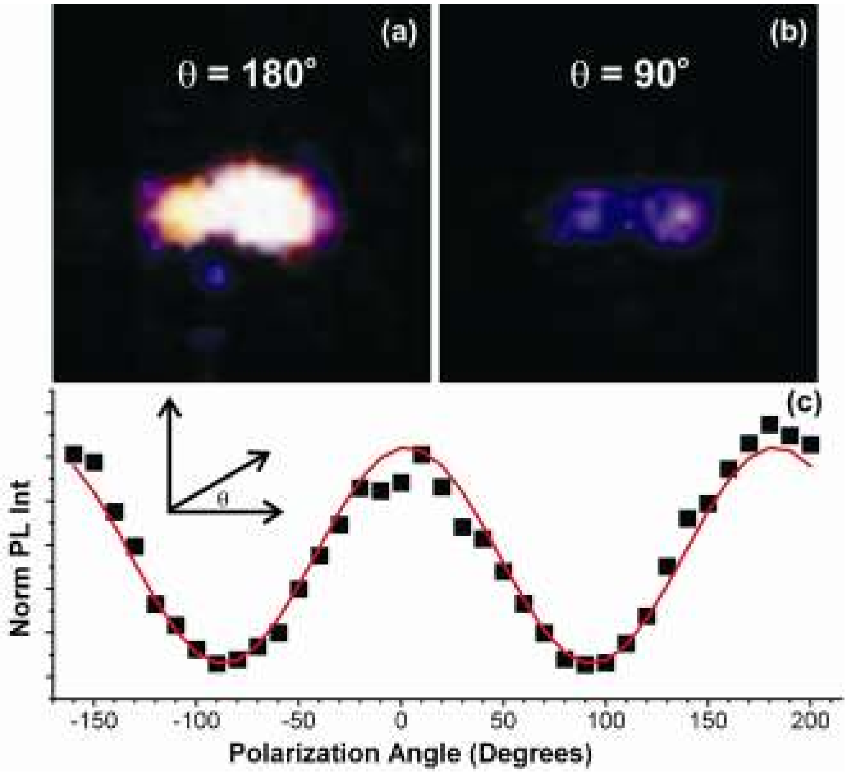

Figure 3.7 Polarization-dependent PL microscopy images of a single CdSe QB. The plot is the PL intensity vs. polarization angle (θ), the angle between the QB axis and the polarization direction. The red curve a cos2θ fit to the data. The QBs were excited at 405 nm through a Nikon Plan Apo 40x, 0.95NA objective. The polarizer was supplied by Meadowlark Optics (VL-100-UV-S).

3.2.4 Gold decoration of CdSe QBs

To account for the high PL QEs and whole-belt delocalization of photogenerated excitons, the density and distribution of surface defects in the QBs were characterized by gold decoration. The method was adapted from the procedures of Banin,[30] Mokari,[31] and coworkers, who previously demonstrated selective Au-nanoparticle deposition on the high-energy tips and surface-defect sites of CdSe QRs[30] and QWs.[31] As an historical aside, we note that analogous decoration strategies were first employed to identify the surface defects associated with Griffith cracks in glass,[32,33] and dislocations in crystals.[34-36] TEM images of the gold-decorated QBs are shown in Figure 3.8. Remarkably, the Au nanoparticles were deposited almost exclusively on the edges of the CdSe QBs, and at considerably lower densities than the corresponding decoration densities previously observed for CdSe QWs.[31] The results suggested comparatively low surface-defect populations in the QBs, with these defects, presumably in proportion to carrier-trapping sites, predominantly located within the thin belt edges.

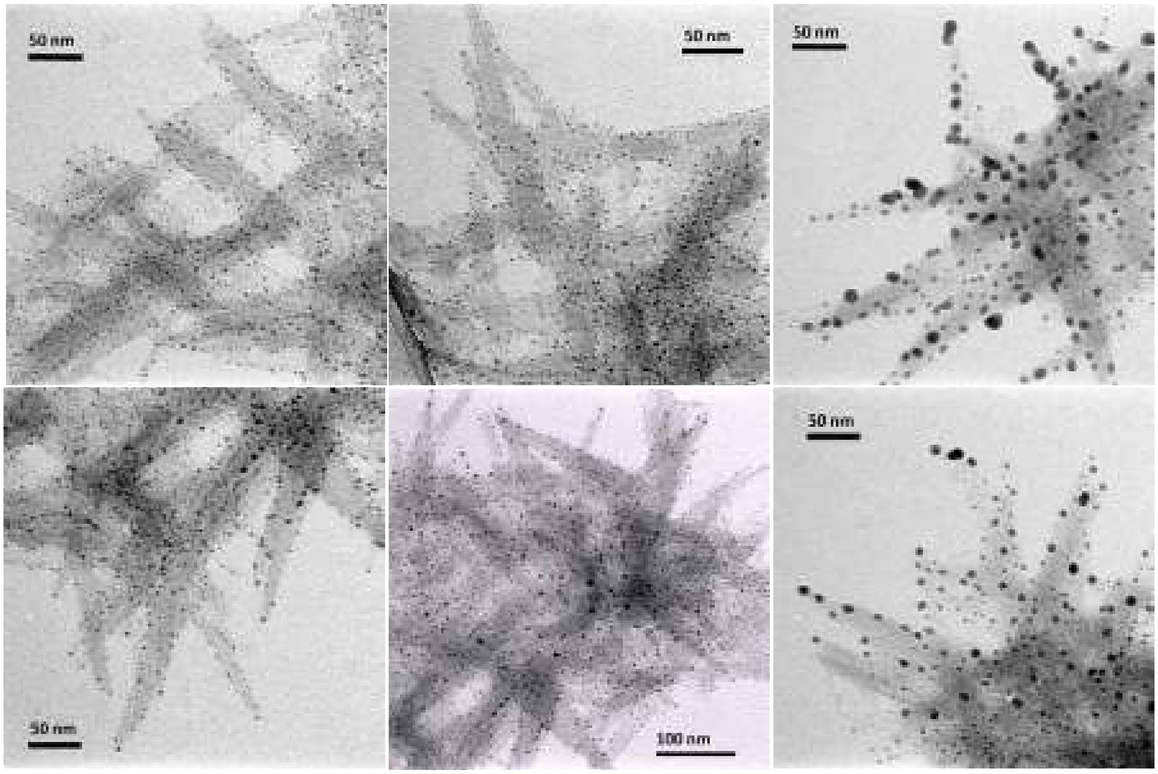

Figure 3.8 TEM images of gold-decorated CdSe QBs. Note that the Au nanoparticles are deposited primarily upon the edges of the QBs.

3.3 Discussion

The identity of the defective edge surfaces was established by the crystallographic orientation of the QBs. We confirmed here the same crystallographic orientation previously determined for the closely related CdSe nanoribbons.[37] The large-area, top and bottom QB surfaces are parallel to the nonpolar $\{11\bar{2}0\}$ wurtzite crystal faces (see Figure 3.9a). Previous theoretical studies of the amine passivation and reconstruction of $\{11\bar{2}0\}$ wurtzite CdSe facets has established them to be stable and well-passivated, with an amine ligand bonded to each surface Cd site.[38-40] The long, thin, edge surfaces are parallel to the nonpolar $\{1\bar{1}00\}$ wurtzite crystal faces. (This family of symmetrically equivalent crystal faces is more commonly identified as the $\{10\bar{1}0\}$ family,[38-40] but the $(1\bar{1}00)$ member of the family is perpendicular to the $(11\bar{2}0)$ face, as is required by the geometry of the QBs.) The $\{1\bar{1}00\}$ facets have only a slightly different surface structure than the $\{11\bar{2}0\}$ facets, and the theoretical studies suggest that they are also stable and well-passivated.[38,40] Even so, our decoration results suggest that the QB $\{1\bar{1}00\}$ edges are more prone to defects than are the $\{11\bar{2}0\}$ top and bottom surfaces.

Although they have been theoretically modeled,[38-41] we note that the precise structures of these $\{11\bar{2}0\}$ and $\{1\bar{1}00\}$ surfaces are unknown. Roughness is evident along the edges of the QBs (Figure 2.11a, b), just as thickness variations are evident in individual QBs (Figure 2.11c). The accumulation of defects on the $\{1\bar{1}00\}$ edges may be intrinsic to the edge-surface structure, or result from the growth mechanism. The important point is that the QBs are so thin relative to their width that the defective $\{1\bar{1}00\}$ surfaces occupy only about 14% of the total QB surface area, effectively minimizing the population of trapping sites. Therefore, the high PL QEs and extensive exciton delocalization in the CdSe QBs appear to be accidents of the growth morphology, and possibly the growth mechanism.

We are now able to conjecture about the differing PL behaviors of CdSe QWs and QBs. Colloidal CdSe QWs having roughly isotropic cross sections exhibit PL QEs of only 0.1-0.3%.[6-11] Furthermore, the fluorescence intermittency in CdSe QWs is predominantly localized blinking or twinkling over small length scales,[6,10,11] which demonstrates that excitons diffuse over only short distances prior to encountering trap sites. These characteristics differ significantly from the 30% QEs and whole-belt exciton delocalization observed here for CdSe QBs. The long axis for both wurtzite CdSe QWs[42,43] and QBs lies along the [0001] direction,[11] and so their side facets should be from the same crystallographic families. Manna and coworkers argue convincingly that the nearly isotropic cross section of QRs and QWs is best accommodated by a dodecahedral-prism geometry having an alternating sequence of $\{11\bar{2}0\}$ and $\{1\bar{1}00\}$ side facets of equal surface area (Figure 3.8b).[38] Therefore, the $\{1\bar{1}00\}$ surface area, which may be inherently more defective, rises from about 14% in the QBs to about 50% in the QWs. Consequently the natural population of surface-trapping sites may be several times greater in the QWs.

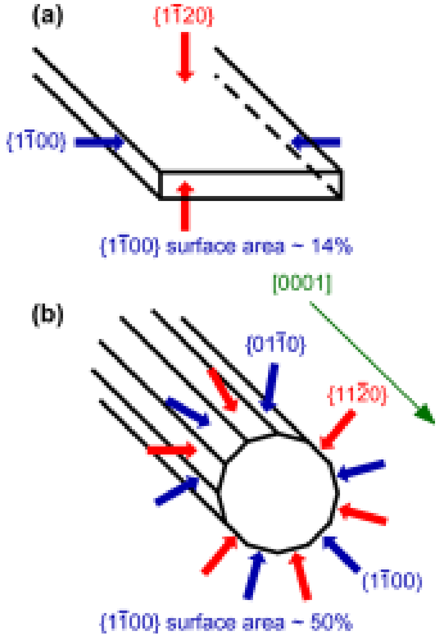

Figure 3.9 Crystallographic assignment of the surfaces (a) expressed in CdSe QBs,[1] and (b) proposed for CdSe QWs.[38] The $\{1\bar{1}00\}$ family of crystallographically equivalent faces, which is more commonly identified as the $\{10\bar{1}0\}$ family, includes the $(10\bar{1}0)$, $(1\bar{1}00)$, $(0\bar{1}10)$, $(\bar{1}010)$, $(\bar{1}100)$, and $(01\bar{1}0)$ faces. The $\{11\bar{2}0\}$ family includes the $(11\bar{2}0)$, $(2\bar{1}\bar{1}0)$, $(1\bar{2}10)$, $(\bar{1}\bar{1}20)$, $(\bar{2}110)$, and $(\bar{1}2\bar{1}0)$ faces.

Alternatively, the trap sites might be preferentially located in the edge *line junctions* between $\{11\bar{2}0\}$ and $\{1\bar{1}00\}$ surfaces rather than on the $\{1\bar{1}00\}$ edge *surfaces*. Because the decorating Au nanoparticles have dimensions of 3-5 nm, and the thickness of the CdSe QBs is ≤ 2 nm, we cannot distinguish edge surface decoration from edge line-junction decoration. However, the number of such line junctions in a dodecahedral-prismatic QW is three times that in a rectangular QB, leading to a larger relative population of surface-trapping sites in QWs than in QBs.

Their excellent properties are due to the highly anisotropic QB cross sections, and specifically to the minimization of surfaces or edges prone to trapping sites. The challenge to extending these excellent properties to QWs more generally is identifying means to diminish defective side facets or edge junctions, or devising specific passivation schemes for such surfaces or edges where trapping sites tend to accumulate.

3.4 Conclusions

We report that type-I CdSe quantum belts (QBs) having thickness of 1.5-2.0 nm exhibit uniform photoluminescence (PL) with efficiencies of ~ 30%. Epifluorescence experiments establish that the PL is polarized along the long dimension of the QBs, and that photogenerated excitons are effectively delocalized along their entire lengths at room temperature.[5,6] Images of Au-decorated QBs suggest that the high PL efficiencies and long-range exciton delocalization are due to a low density of surface trap sites, which are distributed primarily at the edges of the QBs. The results show that pseudo-1D semiconductor nanocrystals can have excellent passivation and optical properties, and effectively transport excitons and presumably charge carriers with minimal losses to non-radiative-recombination pathways.

3.5 Experimental

3.5.1 Materials

n-Octylamine (n-OA) from Aldrich (+99%, product #: O5802-500G) and Alfa Aesar (99%, product #: B24193), selenourea (99.9%, metal basis) from Alpha Aesar, $Cd(OAc)_2{\cdot}2H_2O$ (Aldrich), $AuCl_3$ (99.9%-Au, product #: 93-7907) from Strem, oleylamine (or cis-9-octadecenylamine) from TCI (> 40.0% by GC) and Sigma-Aldrich (technical grade, 70%) were used as received, and stored under N_2. 1-Dodecylamine (DDA, 98% from Alfa Aesar), tetraoctylammonium bromide (TOABr, ≥ 98% from Fluka, product #: 88000) and ethyl alcohol (EtOH) from PHRAMCO-AAPER (95%, USP grade, product #: E190) were used as received. Toluene from Sigma-Aldrich (CHROMASOLV®, for HPLC, ≥ 99.9%) was purged with dry N_2 for at least 1 h and stored under N_2 prior to use. 5,10,15,20-Tetraphenylporphyrin (TPP, free base) was made and purified according to the literature,[44-45] and stored under ambient conditions. Neutral alumina from Merck (Al_2O_3, Brockmann Grade III) was washed with chloroform and dried overnight for use in the chromatographic purification of TPP.

3.5.2 Quantum efficiency (QE) calculation

The room temperature PL quantum yields (QEs) of the CdSe QBs were obtained by comparing the integrated PL intensities of a dye standard, 5,10,15,20-tetraphenylporphyrin (TPP) having a known QY of 7.0 %. Several TPP solutions were prepared in N_2-purged toluene. The concentrations of these solutions were adjusted to produce absorbances in the range of 0.05-0.15 at the wavelength for PL excitation. The PL emission between 550 nm and 850 nm was collected and integrated to give the total TPP emission (I_{TPP}). Five different total emissions (I_{TPP}) were plotted against the corresponding absorptions (A_{TPP}) for each excitation wavelength. Each plot was fit by linear least-squares regression, and the extracted slope and intercept values were subsequently used to calculate I_{TPP} from any individual TPP absorption (A_{TPP}) within the 0.05-0.15 range, as described below. Such a calibration plot was determined concomitantly with each QB QE determination.

The QB QY (QE_{QB}) values were determined by eq 3.1 in the following way. The absorbance (A_{QB}, in the range of 0.05-0.15) and integrated PL intensity (I_{QB}) were obtained from a QB specimen, and those values were inserted into eq 3.1. A_{TPP} was set equal to A_{QB}, and the corresponding I_{TPP} was calculated from the slope and intercept obtained above. Those A_{TPP} and I_{TPP} values were inserted into eq 3.1, and the QE_{QB} calculated.

$$QE_{QB} = \left(\frac{I_{QB}}{A_{QB}}\right) \times \left(\frac{A_{TPP}}{I_{TPP}}\right) \times 7.0 \qquad (3.1)$$

QB QEs were determined at two excitation wavelengths, 397 nm (3.12 eV) and 410 nm (3.02 eV). For each specimen, these values were found to be within a few percent of one another.

3.5.3 Optical microscopy

To obtain PL images and spectra of single CdSe QBs, a small volume (ca. 2 mL) of predominantly unbundled QBs suspended in an oleylamine/toluene solvent was diluted in toluene (ca. 5 mL). The sample was sealed and stored in the dark, but some exposure to air with time likely occurred. Two to three drops of the diluted QB solution was spin-cast onto a cleaned coverslip (Fisher Scientific, No 1.5, 22-mm square). The sample was then transferred to an air-tight enclosure on the microscope stage, and measurements were performed under a steady stream of argon to minimize exposure to air. Epifluorescence microscopy experiments were conducted using an inverted Nikon Eclipse TE2000-E Microscope with a 40×, 0.95NA, Plan Apo objective. The excitation source was a 405-nm *cw* laser (CrystaLaser). Typical power densities were ≈ 120 W/cm^2 for wide-field illumination and ≈ 100 W/cm^2 when focusing to a diffraction-limited spot. PL images and spectra were obtained using a spectrophotometer (Princeton Instruments/Acton SP-2300i with a Photometrics Coolsnap ES CCD camera) mounted to the side port of the microscope. A triple-grating turret within the spectrometer enabled PL images and spectra to be acquired in an efficient manner by switching between a mirror and a 300 groove per mm grating. Images and spectra were acquired with a CCD camera exposure time of 30 ms and 1.000 s, respectively. The PL spectra were recorded using a wavelength resolution of 1.58 nm (9.67 meV). The emission energies and breadths of the emission profiles did not change over the course of the study. The PL spectra from ≈ 50 individual QBs were recorded. The possibility for clustering and the degree of bundling of multiple QBs could not be ruled out, but TEM images of these QB samples suggested a majority of the QBs were unbundled and indeed single.

3.5.4 Polarization experiments

The degree of polarization of the emission from individual QBs was measured using the same microscopy instrumentation as explained above. An aluminum wire-grid polarizer sandwiched by fused silica plates (Meadowlark Optics, VL-100-UV-S) was mounted onto a computer-controlled mechanical rotation stage (Newport Corporation, URS150). The polarizer was positioned between the exit port of the microscope and the entrance-slit of the monochromator. Images were acquired in 10-degree rotation increments, with an exposure time of 30 ms at each angle. The excitation source used (405-nm *cw* laser from CrystaLaser) was linearly polarized. Out of the 12 QBs that were studied, 11 QBs followed a strong $\cos 2\theta$ dependence with the polarization axis lying along the long-axis of the QBs.

3.5.5 Gold decoration

This method was adapted from the literature.[46] A stock solution of DDA (496 mg, 1.07 mmol) and TOABr (692 mg, 1.27 mmol) in toluene (49 g) was prepared. In a typical procedure, $AuCl_3$ (2 mg, 7 μmol) was added to the stock solution (4.4 g), and the mixture was sonicated in a bench-top ultrasonic cleaner at room temperature for 5 min, whereupon the solution color changed to light yellow. A toluene dispersion (0.46 g) of bundled CdSe QBs having an absorbance of ca. 0.05 at 372 nm was added drop-wise into the $AuCl_3$-DDA-TOABr solution (0.54 g) at -12 ºC. The addition was completed within 3 min, and the reaction was allowed to continue for an additional 3 min before quenching by addition of EtOH (0.5 mL) to flocculate the QBs. The mixture was centrifuged in a bench-top centrifuge for 5-10 min, and the supernatant was discarded. The brown precipitate of decorated QBs was retained for subsequent TEM analysis.

Under these synthetic conditions, the diameters of the deposited gold nanoparticles were found to be generally within 3-5 nm, with some localized aggregates having dimensions of up to 20 nm. In separate trials, the nanoparticle sizes were found to vary with the reaction temperature, reaction time, and $AuCl_3$ concentration in the $AuCl_3$-DDA-TOABr solution.

3.6 References

1. Qu, L.; Peng, X. *J. Am. Chem. Soc.* **2001,** *124*, 2049-2055.
2. de Mello Donegá, C.; Hickey, S. G.; Wuister, S. F.; Vanmaekelbergh, D. V.; Meijerink, A. *J. Phys. Chem. B* **2003**, *107*, 489-496.
3. Qian, L.; Bera, D.; Tseng, T.-K.; Holloway, P. H. *Appl. Phys. Lett.* **2009**, *94*, 073112.
4. Manna, L.; Scher, E. C.; Li, L.-S.; Alivisatos, A. P. *J. Am. Chem. Soc.* **2002**, *124*, 7136-7145.
5. Mokari, T.; Banin, U. *Chem. Mater.* **2003**, *15*, 3955–3960.

6. Protasenko, V.; Gordeyev, S.; Kuno, M. *J. Am. Chem. Soc.* **2007**, *129*, 13160-13171.
7. Puthussery, J.; Lan, A.; Kosel, T. H.; Kuno, M. *ACS Nano* **2008**, *2*, 357-367.
8. Kuno, M. *Phys. Chem. Chem. Phys.* **2008**, *10*, 620-639.
9. Wang, F.; Yu, H.; Li, J.; Hang, Q.; Zemlyanov, D.; Gibbons, P. C.; Wang, L.-W.; Janes, D. B.; Buhro, W. E. *J. Am. Chem. Soc.* **2007**, *129*, 14327-14335.
10. Protasenko, V.; Hull, K. L.; Kuno, M. *Adv. Mater.* **2005**, *17*, 2942-2949.
11. Glennon, J. J.; Tang, R.; Buhro, W. E.; Loomis, R. A. *Nano Lett*. **2007**, *7*, 3290-3295.
12. Kamat, P. V. *J. Phys. Chem. C* **2008**, *112*, 18737–18753.
13. Law, M.; Greene, L. E.; Johnson, J. C.; Saykally, R.; Yang, P. *Nat. Mater.* **2005**, *4*, 455-459.
14. Yuhas, B. D.; Yang, P. *J. Am. Chem. Soc*. **2009**, *131*, 3756-3761.
15. Huynh, W. U.; Dittmer, J. J.; Alivisatos, A. P. *Science* **2002**, *295*, 2425-2427.
16. Hines, M. A.; Guyot-Sionnest, P. *J. Phys. Chem.* **1996**, *100*, 468-471.
17. Peng, A.; Schlamp, M.C.; Kadavanich, A.V.; Alivisatos, A. P. *J. Am. Chem. Soc.* **1997**, *119*, 7019-7029.
18. Bussian, D.A.; Crooker, S. A.; Yin, M.; Brynda, M.; Efros, A. L.; Klimov, V.I. *Nat. Mater.* **2009**, *8*, 35-40.
19. Xie, R. G.; Kolb, U.; Li, J. X.; Basche´, T.; Mews, A. *J. Am. Chem. Soc.* **2005**, *127*, 7480.
20. Talapin, D. V.; Mekis, I.; Go¨tzinger, S.; Kornowski, A.; Benson, O.; Weller, H. *J. Phys. Chem. B* **2004**, *108*, 18826.
21. Goebl, J.A.; Black, R.W.; Puthussery, J.; Giblin, J.; Kosel, T.H.; Kuno, M. *J. Am. Chem. Soc.* **2008**, *130*, 14822-14833.

22. Ithurria, S.; Dubertret, B. *J. Am. Chem. Soc.* **2008**, *130*, 16504-16505.
23. Liu, Y.H.; Wayman, V. L.; Gibbons, P. C.; Loomis, R. A.; Buhro, W. E. *Nano Lett.*, **2010**, *10*, 352–357.
24. Kalt, H.; Zhao, H.; Dal Don, B.; Schwartz, G.; Bradford, C.; Prior, K. J. *Lumin*. **2005**, *112*, 136-141.
25. Zhao, H.; Moehl, S.; Kalt, H. *Phys. Rev. Lett.* **2002**, *89*, 097401.
26. Zhao, H.; Dal Don, B.; Moehl, S.; Kalt, H.; Ohkawa, K.; Hommel, D. *Phys. Rev. B* **2003**, *67*, 035306.
27. Hu, J.; Li, J.-s.; Yang, W.; Manna, L.; Wang, L.-W.; Alivisatos, A. P. *Science* **2001**, *292*, 2060-2063.
28. Wang, J.; Gudiksen, M. S.; Duan, X.; Cui, Y.; Lieber, C. M. *Science* **2001**, *293*, 1455-1457.
29. Venupopal, R.; Lin, P.-I; Liu, C.-C.; Chen, Y.-T. *J. Am. Chem. Soc.* **2005**, *127*, 11262-11268.
30. Mokari, T.; Rothenberg, E.; Popov, I.; Costi, R.; Banin, U. *Science* **2004**, *304*, 1787-1790.
31. Jen-la Plante, I.; Habas, S. E.; Yuhas, B. D.; Gargas, D. J.; Mokari, T. *Chem. Mater*. **2009**, *21*, 3662-3667.
32. Andrade, E. N. da C.; Tsien, L. C. *Proc. Royal Soc. London, Ser. A* **1937**, *159*, 346-354.
33. Gordon, J. E.; Marsh, D. M., Parratt, M. E. M. L. *Proc. Royal Soc. London, Ser. A* **1959**, *249*, 65-72.

34. Amelinckx, S.; Van der Worst, W.; Gevers, R.; Dekeyser, W. *Phil. Mag.* **1955**, *46*, 450-451.
35. Amelinckx, S. *Phil. Mag.* **1956**, *1*, 269-290.
36. Bartlett, J. T.; Mitchell, J. W. *Phil. Mag.* **1958**, *3*, 334-341.
37. Joo, J.; Son, J.S.; Kwon, S.G.; Yu, J.H.; Hyeon, T. *J. Am. Chem. Soc.* **2006**, *128*, 5632-5633.
38. Manna, L.; Wang, L. W.; Cingolani, R.; Alivisatos, A. P. *J. Phys. Chem. B* **2005**, *109*, 6183-6192.
39. Rempel, J. Y.; Trout, B. L.; Bawendi, M. G.; Jensen, K. F. *J. Phys. Chem. C* **2006**, *110*, 18007-18016.
40. Csik, I.; Russo, S. P.; Mulvaney, P. *J. Phys. Chem. C* **2008**, *112*, 20413-20417.
41. Son, J. S.; Wen, x.-D.; Joo, J.; Chae, J.; Baek, S.-i.; Park, K.; Kim, J. H.; An, K.; Yu, J. H.; Kwon, S. G.; Choi, S.-H.; Wang, Z.; Kim, Y.-W.; Kuk, Y.; Hoffman, R.; Hyeon, T. *Angew. Chem. Int. Ed.* **2009**, *48*, 1-5.
42. Yu, H.; Li, J.; Loomis, R. A.; Gibbons, P. C.; Wang, L.-W.; Buhro, W. E. *J. Am. Chem. Soc.* **2003**, *125*, 16168-16169.
43. Wang, F.; Dong, A.; Sun, J.; Tang, R.; Yu, H.; Buhro, W. E. *Inorg. Chem.* **2006**, *45*, 7511-7521.
44. Adler, A. D.; Longo, F. R.; Váradi, V. *Inorg. Synth.* **1976**, *16*, 213.
45. Barnett, G. H.; Hudson, M. F.; Smith, K. M. *J. Chem. Soc.; Perkin Trans. I*, **1975**, 1401-1403.
46. Mokari, T.; Sztrum, C. G.; Salant, A.; Rabani, E.; Banin, U. *Nat. Mater.* **2005**, *4*, 855-863.

Chapter 4: Photoluminescence Enhancement and Spectroscopic Analyses of Surface Passivated CdTe Quantum Wires

4.1 Introduction

Cadmium telluride (CdTe) has been extensively studied for photovoltaic (PV) technology with a bulk band gap of 1.5 eV at room temperature.[1] In addition, CdTe nanostructures, such as quantum wires (QWs), are actively considered for solar-cell[2-3] and biological imaging applications,[4-5] due to their tunable sizes and additional near-infrared absorption and emission.

Since a high-quality synthesis of colloidal CdTe quantum wires (QWs) grown by the solution-liquid-solid (SLS) method,[6] their optical transitions have been predicted by high-level electronic-structure calculations and their diameter dependences have been quantitatively correlated.[7] However, one issue underlying practical applications was the disappointingly low (0.1-2 %) PL quantum efficiency (QE), due to nonradiative recombination from defect sites on the QW surfaces.[8] Core-shell structures have been successfully applied to enhance photoluminescence and to suppress blinking of various colloidal quantum dots (QDs) and quantum rods (QRs).[9-11] Inhomogeneous core-shell structures of quantum wires (QWs) routinely possess trap sites, and the prevalence of such defect sites can be quickly assessed by using photoluminescence (PL) spectroscopy. A reliable and strong PL signal and consequently high PL efficiency is an indication of a well-passivated surface.

According to the literature,[12-13] ZnS shells have passivated CdTe QDs for higher quantum efficiency (QE). Interestingly, a growth of thin layer of $\mathrm{CdTe}_{1-x}(\mathrm{SR})_x$ (R = alkyl) shell successfully protect the "luminescent cores" after a post-modification with alkyl thiols.[14] An adsorption of zinc ions also enhances the PL of luminescent CdTe QDs, following a Langmuir binding model. Herein we develop a combined strategy with sequential depositions of molecular thiol and zinc shells onto the CdTe QW surface. The strategy produces luminescent CdTe QWs, nearly 100-fold brighter than the as-made CdTe QWs, after multiple consecutive steps.

Engineering passivating processes resolves unreliable PL measurements and short shelf-life issues of the air-sensitive QWs. After successful surface passivation, more spectroscopic analyses, such as PL, PLE, epifluoroscence and lifetime measurements, are conducted to experimentally reveal the electronic transitions in the CdTe QW systems. The development of this methodology may lead to successful passivation of other colloidal semiconductor nanostructures in the future.

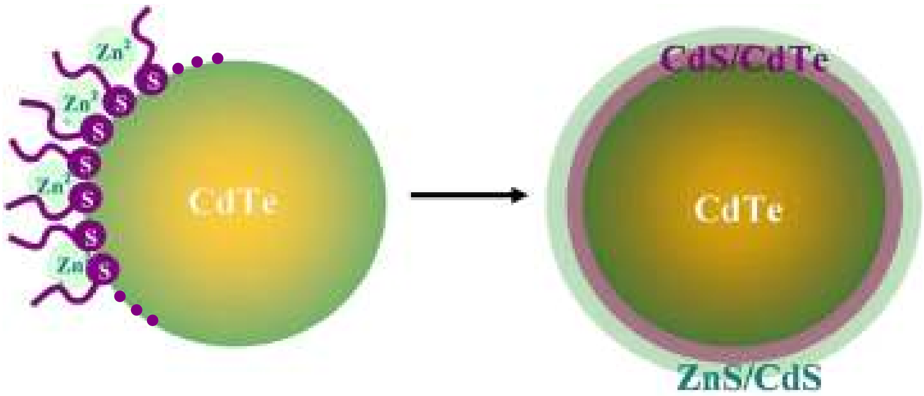

Scheme 4.1 A proposed strategy to make "molecular shells" via absorption of thiol and a zinc complex onto CdTe QW surface.

4.2 Results

4.2.1 Thiol passivation of CdTe QWs

Various alkyl thiols were used to conduct surface passivation of CdTe QWs. Investigation of dual-functionalized thiols was inspired by the possibility of tunable functionality for QW applications. However, either the chain length or additional functionality somehow affected the QW surface passivation. Three dual-functional thiols, 11-mercaptoundecanoic acid (MUA), 11-mercaptoundecanol (MUO) and 1, 6-hexanedithiol (HDT), were studied. In Figure 4.1, low PL intensity and asymmetric PL features indicated significant population of trap sites on CdTe QW passivated with these thiols. The unsuccessful passivation was proposed in following assumptions.

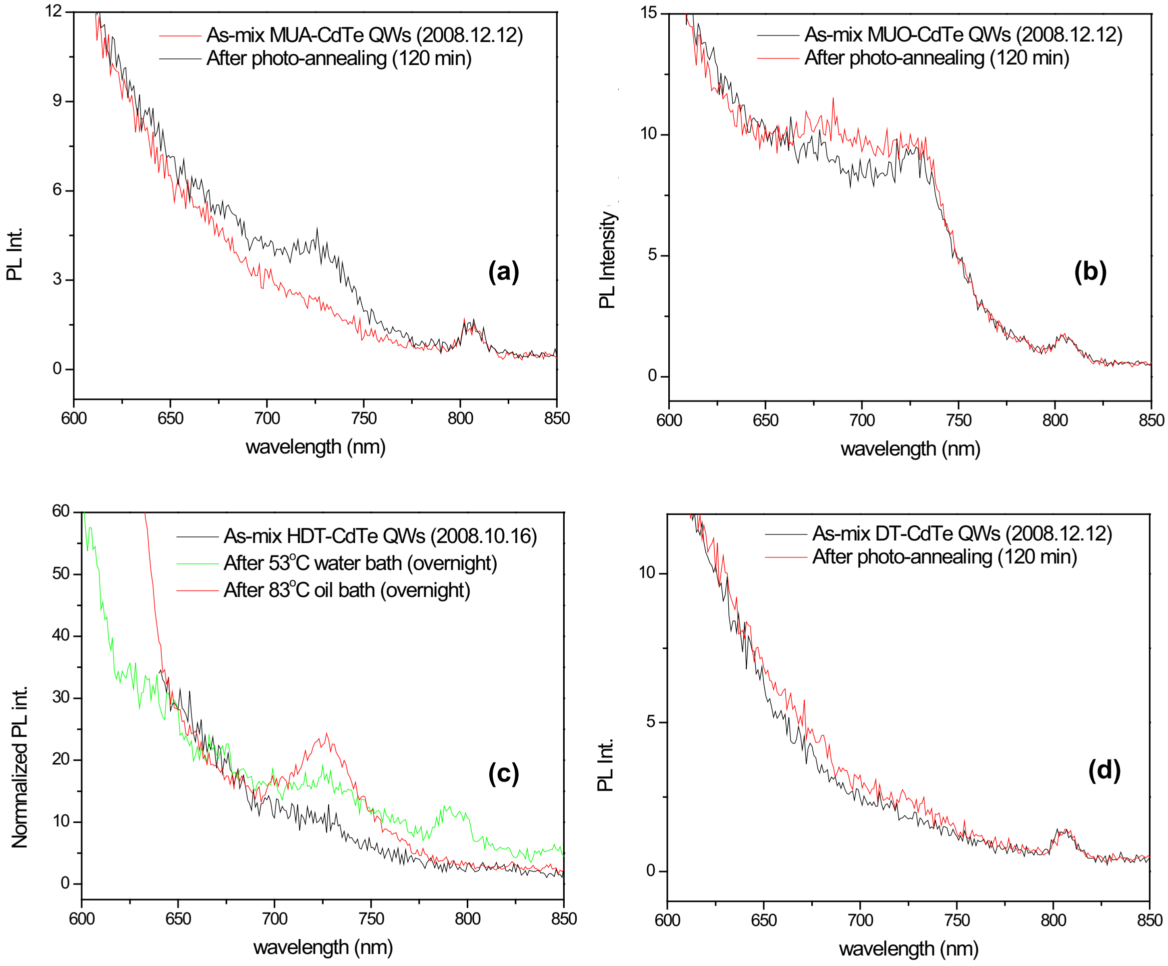

Figure 4.1 PLs of passivated CdTe QWs with different thiols. (a) 11-mercaptoundecanoic acid (MUA); (b)11-mercaptoundecanol (MUO); (c)1,6-hexanedithiol (HDT); (d) 1-dodecanethiol (DT). All PL spectrum were conducted by the departmental fluorimeter.

First, dual-functional thiols created a passivation competition for two functional groups. Carboxylic or alcohol groups possibly bind to the surface, competing with the thiol group (-SH) for surface-ligand exchange. Second, surface exchange may require the displacement of bulky TOPO or alkylphosphonate ligands, which small thiols are better able to do. Ethanethiol (ET) and aminoethanethiol hydrochloride (AET·HCl), were used to resolve our assumptions for poor PL enhancement by long carbon-chain thiols. The PL enhancement was observed by a sequence order of ethanethiol (ET) > AET·HCl >> HDT > MUO ~ MUA > DT. According to this sequence, dual-functional thiols should be *not* considered for surface passivation, regardless of their carbon-chain lengths.

Experiments suggested ethanethiol (ET) was one of the most efficient ligands to passivate CdTe QWs. The PL enhancement results strongly depended on time allowed for the ligand-exchange process, which usually required 1-2 days to maximize. In Fig 4.2 (a), as-made CdTe QWs usually showed very weak or no PL in toluene. The disappointingly low PL was due to a non-radiative recombination from surface trapping sites. Adding ethanethiol (ET) into CdTe QW toluene solution scarcely improved PL emission around 735 nm initially. According to Akamatsu *et al*, the surface ligands of CdTe QDs could be exchanged by excess ethanethiol in solution,[14] leading to substantial passivation of the surface trapping sites.

PL enhancement by ET proceeded slowly at room temperature for CdTe QWs. After a short exposure (0.5-2 h) to a 100-W tungsten-lamp, the enhancement was expedited with an observation of QW precipitation from the solution, consistent with a ligand exchange (Figure 4.2c). The dispersion of the precipitate gave asymmetric PL features with an estimated quantum efficient (QE) of 0.5-1%, as shown by the orange curve in Figure 4.2 (a). The total PL feature was fitted with two Lorentzian profiles at 726 nm and 681 nm, respectively, in addition to one broad Lorentzian profile for background scattering (centered at 552 nm).

The PL emission at 726 nm was assigned to the band-gap emission (BGE, PL_B) of the thiolate-CdTe QWs. The origin of the shorter-wavelength emission (SWE, PL_S) at 681 nm is still unresolved. A recent study correlated the SWE to an indirect band-gap recombination of different confinement domains between crystal alternation of wurtzite (WZ) and zinc blende (ZB) in quantum wire structures.[15] After the thiolate-exchanged QWs were allowed to stand on the bench overnight (12 h) in the dark, the QE was optimized at an estimated 1-1.5 %. Well-resolved PLE structures were observed in both photo-annealed and optimized thiolate-exchanged CdTe QWs in Figure 4.2 (b). No significant shift was observed in absorption and PLE spectra after the overnight optimization period.

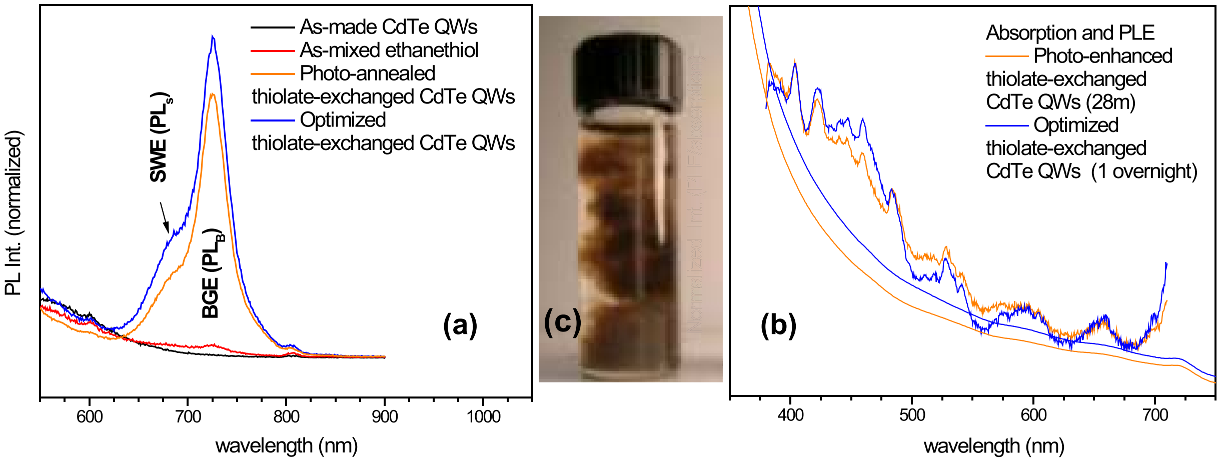

Figure 4.2 Monitoring PL enhancements of thiolate-exchanged CdTe QWs. (a) as-made CdTe QWs in toluene solution (black curve); after adding ethanethiol (red curve); then after 28-min photo-annealing process (orange curve); then after one dark-overnight optimization (blue curve). (b) Comparison of the PLE resolved features and absorption smoother curves of the photo-annealed thiolate-exchanged CdTe QW sample (orange curves) and the optimized sample after one dark-overnight (blue curves). (c) Thiolate-exchanged CdTe QWs during the photo-annealing.

Storage of the QWs in a thiol containing solution preserved the PL enhancement. Solutions of a sufficient high thiol concentration substantially maintained the PL intensity from a few days to a few weeks. In Figure 4.3, an ethanethiol (EtSH) different concentration was individually added to an as-made CdTe QW solution. The initial quantum efficiency (QE) of the thiolate-exchanged CdTe QWs was around 0.4% (the 1st red cross-circle point), and was around 1.1% after photo-annealing (the 2nd red cross-circle and the 1st black cross-square). We noticed that the solution of higher thiol concentration (containing 36.7 w/w % thiol in the solution, S/Cd = 1230) maintained appreciable QE (~1%) for at least two weeks, but in the less-concentrated thiol solution (containing 22.1 w/w % thiol in the solution, S/Cd = 1050) the QE decreased gradually to 0.3 % three weeks after photo-annealing. These results indicated that excess ethanethiol consistently passivated the CdTe QWs and maintained longer QE shelf lives.

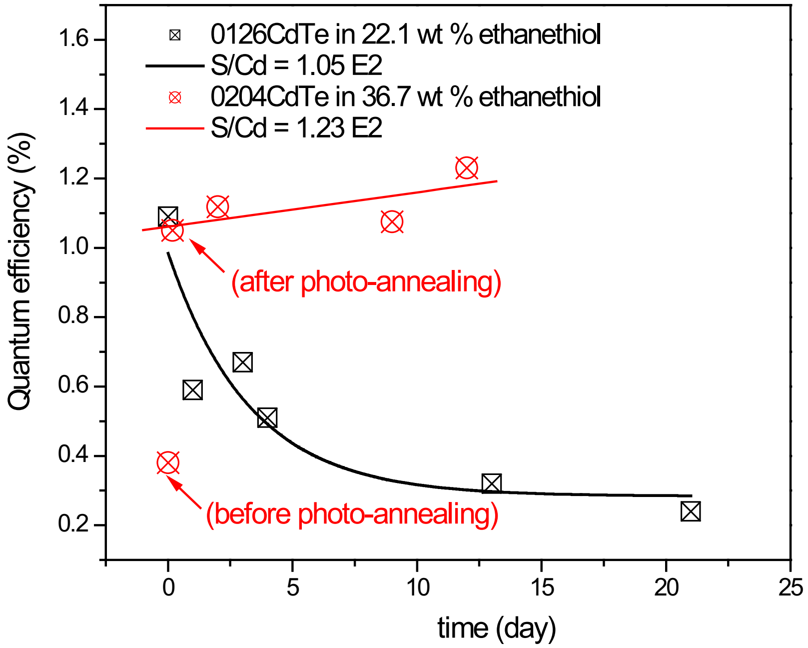

Figure 4.3 Monitoring thiolate-CdTe QWs stored in different thiol concentrations after photo-enhancement. QE for thiolate-CdTe QW was ~0.4 % prior to annealing. The mole ratio was calculated based on the masses of 97% ethanethiol in the passivation and 99.9% cadmium oxide for the QW synthesis.

4.2.2 Zinc-complex passivation of CdTe QWs and isotherm adsorption

Zinc compounds were also reported for PL enhancement of CdTe QDs.[16] In Figure 4.4 (a), two zinc precursors, $ZnCl_2$ and zinc neo-decanoate (ZND), were individually dissolved in *i*-propanol (*i*-PrOH). In a control experiment, *i*-PrOH immediately quenched the PL of the CdTe QWs (black curve). When $ZnCl_2$/*i*-PrOH was accordingly added into a CdTe QW solution, the CdTe QW PL was still quenched (red curve). When zinc neo-decanoate (ZND)/*i*-PrOH was added, a small PL feature was observed (green curve). In Figure 4.4 (a), a band-gap emission (PL_B) and a shorter wavelength emission (PL_S) were observed after ZND was added (green curve). This result indicated that ZND partially passivated the CdTe QW surface in *i*-propanol, but $ZnCl_2$ did not.

ZND enhancement of CdTe QWs was conducted at three ZND concentrations. In Figure 4.4 (b), both PL and PLE intensities corresponded to the ZND concentration. The final ZND concentration was 0.22 mol/L in the first sample (black curve) and 0.31 mol/L in the second sample (red curve). The red curve (higher ZND concentration) showed more intense and resolved PLE features than the black curve (lower ZND concentration). This indicated that a higher ZND concentration in the solution led to a better ZND-passivated QW surface. As a result, resolved electronic transitions were observed by PLE spectroscopy. In a control experiment, adding small amounts of *i*-propanol with ZND consistently quenched most of the PL/PLE intensity and the PLE structure (green curve). Therefore, usage of any *i*-propanol should be avoided.

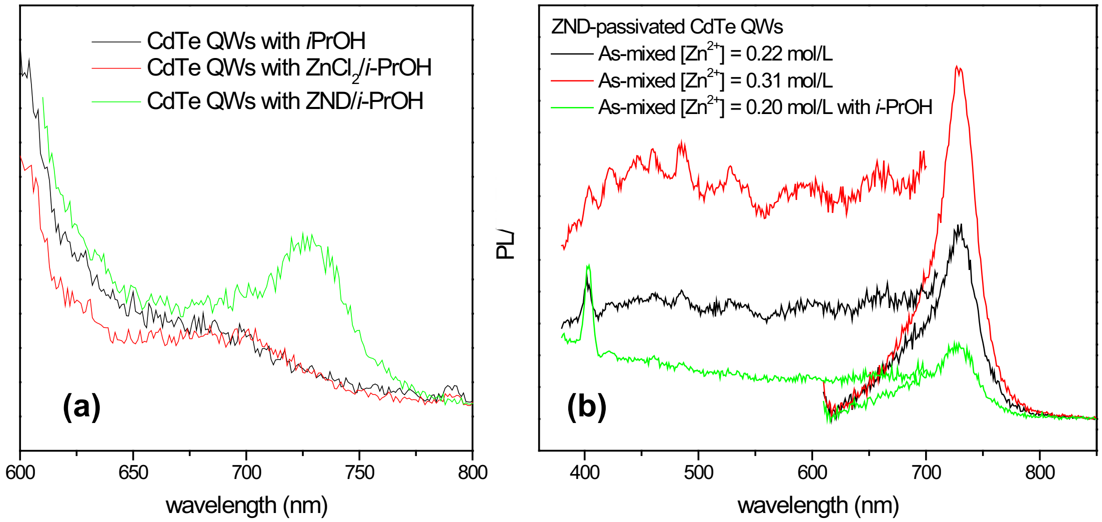

Figure 4.4 PL and PLE enhancement of Zn-passivated CdTe QWs. (a) PL of CdTe QW toluene solution with *i*-PrOH (black curve); with ZnCl$_2$/*i*-PrOH (red curve); with ZND/*i*-PrOH (green curve). (b) PL and PLE of ZND-passivated CdTe QWs (black curve, 0.22 mol/L of Zn^{2+}); with more ZND (red curve, 0.31 mol/L of Zn^{2+}); with ZND/*i*-PrOH (green curve, 0.20 mol/L of Zn^{2+}).

Diethyl zinc (ZnEt$_2$) has been previously used for making CdE/ZnE (E=S, Se, Te) core/shell structures due to its high solubility and reactivity.[9] ZnEt$_2$ is an air-sensitive volatile liquid, which requires careful handling in a glove box. The ZnEt$_2$ solution was prepared with TOP in toluene (abbreviated as ZTT), and transferred to a schlenk flask prior to use. To our surprise, ZTT initially suppressed CdTe QW PL (black curve→ red curve in Figure 4.5a). After photo-annealing for 29 min, the original PL intensity was retrieved. Photo-annealing assisted a surface reconstruction by ligands and the zinc complex, which led to a better passivated surface. After photo-annealing, the PL intensity continued to enhance on the bench top during the following three days. This phenomenon indicated that this slow process dominated the PL enhancement during the meantime. In Fig 4.5 (b), the optimized ZTT-passivated CdTe QWs showed a PLE spectrum with electronic transitions more resolved than its absorption spectrum with similar electronic transitions. The decrease in PLE intensity at shorter wavelengths was due to background absorption from TOP telluride which has large absorption cross-section at the excitation wavelengths below 500 nm.

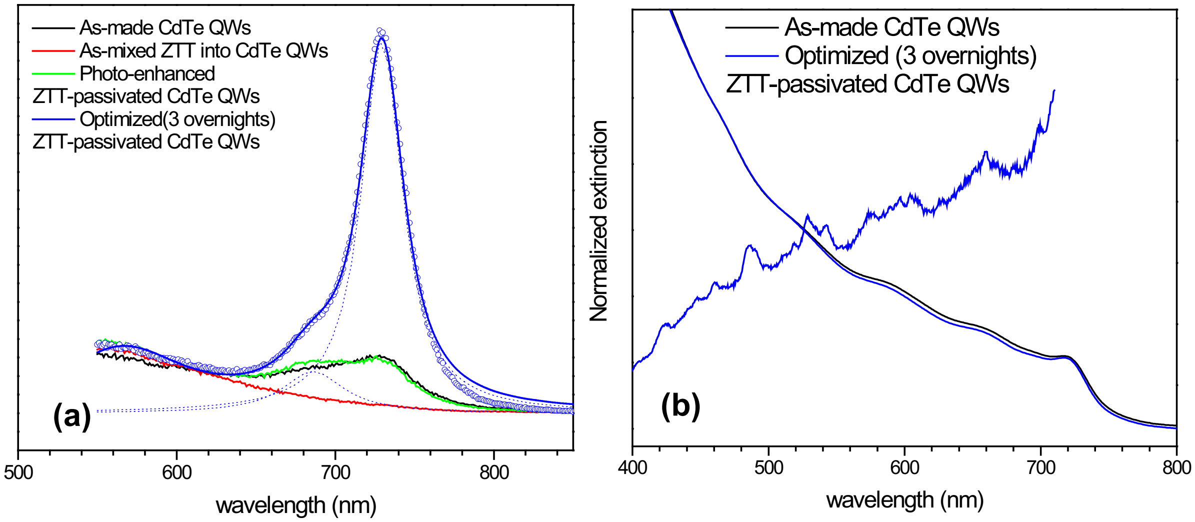

Figure 4.5 PL enhancements of ZTT-passivated CdTe QWs. (a) PL spectra of as-made CdTe QW (black curve); after adding ZTT complex (red curve); then after 29-min photo-annealing (green curve); then optimized after three overnights in the dark (blue curve). (b) Comparison of the extinction and the PLE of the as-made CdTe QW (black) and the optimized ZTT-passivated CdTe QWs (blue curve).

Multiple PL emission features were enhanced by the ZnEt$_2$/TOP/toluene (ZTT) solution. In Fig 4.6 (a), asymmetric PL was composed of band-gap emission (PL$_B$) and shorter wavelength emission (PL$_S$), which were not equally enhanced after ZTT enhancement. The dotted curves are Lorentzian profile fittings for the PL$_B$ and PL$_S$ emissions. Even though the total PL (= PL$_B$ + PL$_S$) intensity was slightly increased after the ZTT enhancement, the PL$_S$ intensity was nearly unchanged. It indicated that enhanced total PL intensity actually came from the enhanced PL$_B$ emission. In a sample that stood 18 h on a bench top, a small intensity reduction and a red-shift (735 nm – 731 nm = 4 nm) were observed. The small intensity reduction might be due to O_2 quenching during 18 h standing in the air. A further verification was conducted after N_2 purging.

ZTT enhancement gave a slightly different total PL emission after N_2 purging. The N_2 purging was repeated twice after the ZTT solution was added. A sample of ZTT-enhanced CdTe QWs that had stood overnight was first purged with N_2 for 2 min. By comparing the intensity scale in Figure 4.6 (a) and (b), the N_2-purged sample (green curve in b) gained 70% more intensity than the sample without N_2-purging (green curve in a). In addition, the total PL shape of the N_2-purged sample became even more symmetrical. The shorter-wavelength emission peak (PL_S), centered between 697-701 nm, disappeared. Instead, an unidentified emission peak (PL_X, centered at 722-725 nm) red shifted close to the band-gap emission (PL_B) was formed. Repeating the cycle of aging the sample on the bench top and N_2-purging continued to increase the PL intensity. According to the results, we also believed that N_2-purging was one of essential strategies to maintain high PL intensity and good line shapes for ZTT-passivated CdTe QWs.

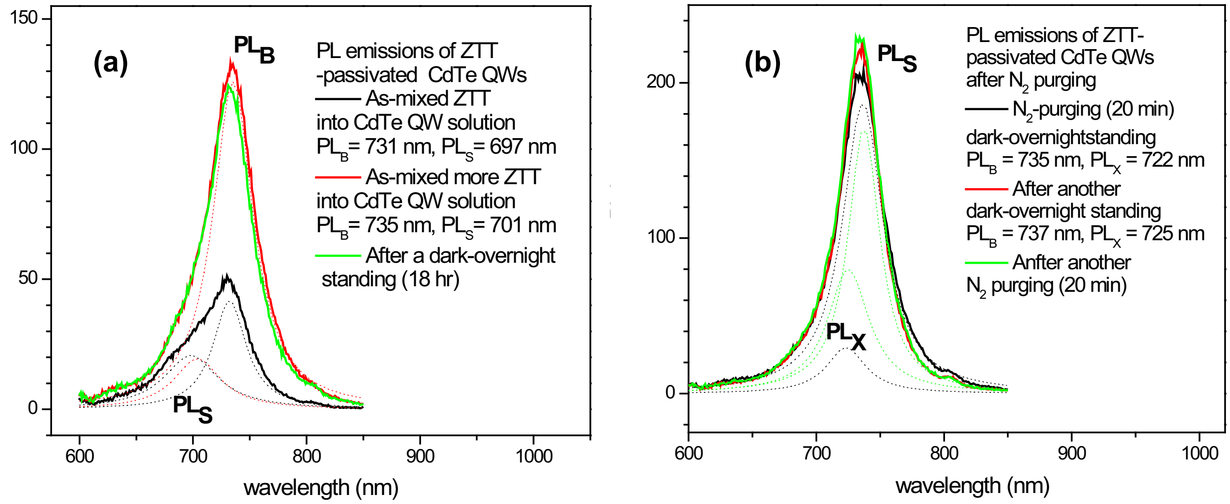

Figure 4.6 PL enhancement of ZTT-CdTe QWs. (a) after adding ZTT complex (black curve); after adding *more* ZTT complex (red curve); then after 18 h dark-overnight standing (green curve). (b) Dark-overnight sample after N_2-purging (black curve); then after another dark-overnight standing (red curve); after another N_2 purging (green).

The literature reports that metal ions dramatically affect the PL of CdTe QDs.[16] Fe^{2+}, Fe^{3+}, Mn^{2+} and Co^{2+} suppress the PL of CdTe QDs, but Zn^{2+} and Mg^{2+} enhance it. In general, ion adsorption is a complex process that involves chemical steps and ligand rearrangements. In addition, studies at the solid/liquid interface have proved particularly valuable in improving our knowledge of the chemical physics of surfaces. We use two models, Langmuir and BET isotherms, to analyze the zinc adsorption on the CdTe QW surface.

Both models were originally used to describe the gas isotherm at the solid interface, as shown in Scheme 4.2. By applying Langmuir and BET equations to liquid-phase adsorption, one may simply substitute liquid-phase concentration (C) for partial pressure of the adsorbates (P) in the classical Langmuir and BET equations. The results computed by two models for Zn adsorption on the CdTe QWs will be considered. We are herein interested in two questions: how the PL responded to the zinc-complex adsorption, and what kind of interaction occurred between the adsorbed complex and the surface.

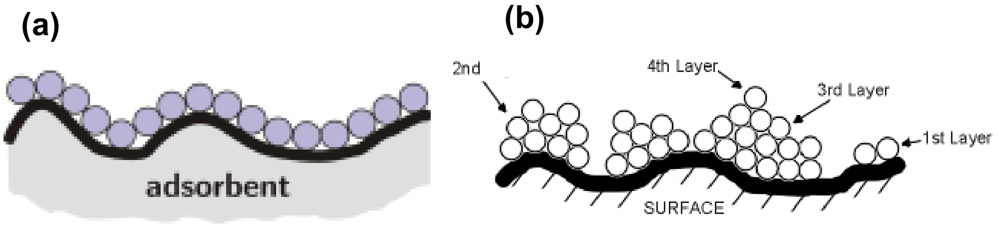

Scheme 4.2 Schematics of (a) Langmuir (monolayer) and (b) BET (multilayer) adsorbates at the interface.

Zinc neodecanoate (ZND) was used to conduct the adsorption study with CdTe QWs. Zinc complex solution was freshly prepared by dissolving zinc in N_2-purged toluene. By varying zinc concentrations, photoluminescence of thiolate-passivated CdTe QW showed a strong dependence on zinc complex concentration (Figure 4.7). This behavior was similar to a Langmuir adsorption isotherm (Figure 4.8). By equating gas partial pressure (*P*) to zinc complex concentration (*C*), similar Langmuir equation for solid/liquid isotherm was obtained (eq 4.1).[16]

$$\frac{C}{I} = \left(\frac{1}{KI_{\max}}\right) + \left(\frac{1}{I_{\max}}\right)C \qquad (4.1)$$

In this formula, *K* is the equilibrium constant, and *C* the complex concentration. *I* and I_{max} represent the PL intensity obtained at a given complex concentration, and the maximum intensity, respectively.

A Langmuir isotherm represents monolayer coverage or adsorption of molecules on a solid surface in response to gas pressure or concentration of a medium above the solid surface at a fixed temperature.[17] The assumptions for Langmuir adsorption are:

1. Adsorption occurs on specific sites and all adsorption sites are identical;
2. The energy for adsorption is independent of how many of the surrounding sites are occupied;
3. Only one adsorbate occupies each site and once all sites are occupied, further adsorption ceases.

The first two assumptions were not entirely valid here because surface trapping sites on CdTe QWs were not likely identical. In addition, varying steric effects and an uneven distribution of the trap sites may produce unequal adsorption energies. Therefore, a single equilibrium constant obtained from an over-simplified Langmuir model would likely not be specific to any single trap-site adsorption. PL efficiency as a function of ZND concentration is shown in Figure 4.7. A non-linear relationship was found. The quantum efficiency based on the total and band-gap emissions are plotted separately.

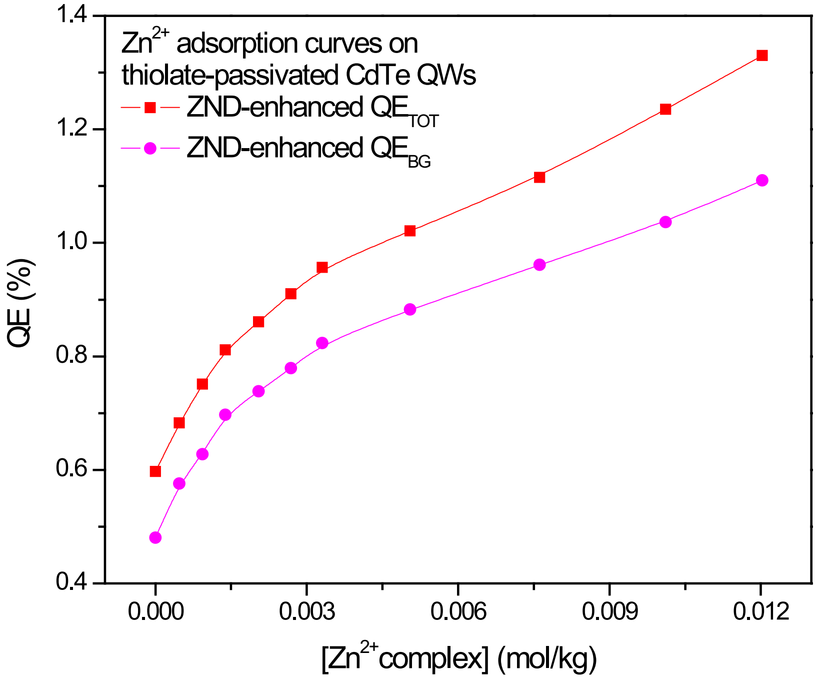

Figure 4.7 Zn adsorption isotherm curves. Enhanced QE_{TOT} and QE_{BG} were individually plotted with zinc complex concentration (*C*).

The data in Figure 4.7 were analyzed by eq 4.2, which is a revised form of eq 4.1 Equation 4.2 replaces intensities (I and I_{max}) with quantum efficiencies (QE and QE_{max}), which are proportional quantities. Figure 4.8 plots ZND concentration over QE vs. ZND concentration. According to eq 4.2, a linear plot is expected for Langmuir surface adsorption of ZND onto the CdTe QWs.

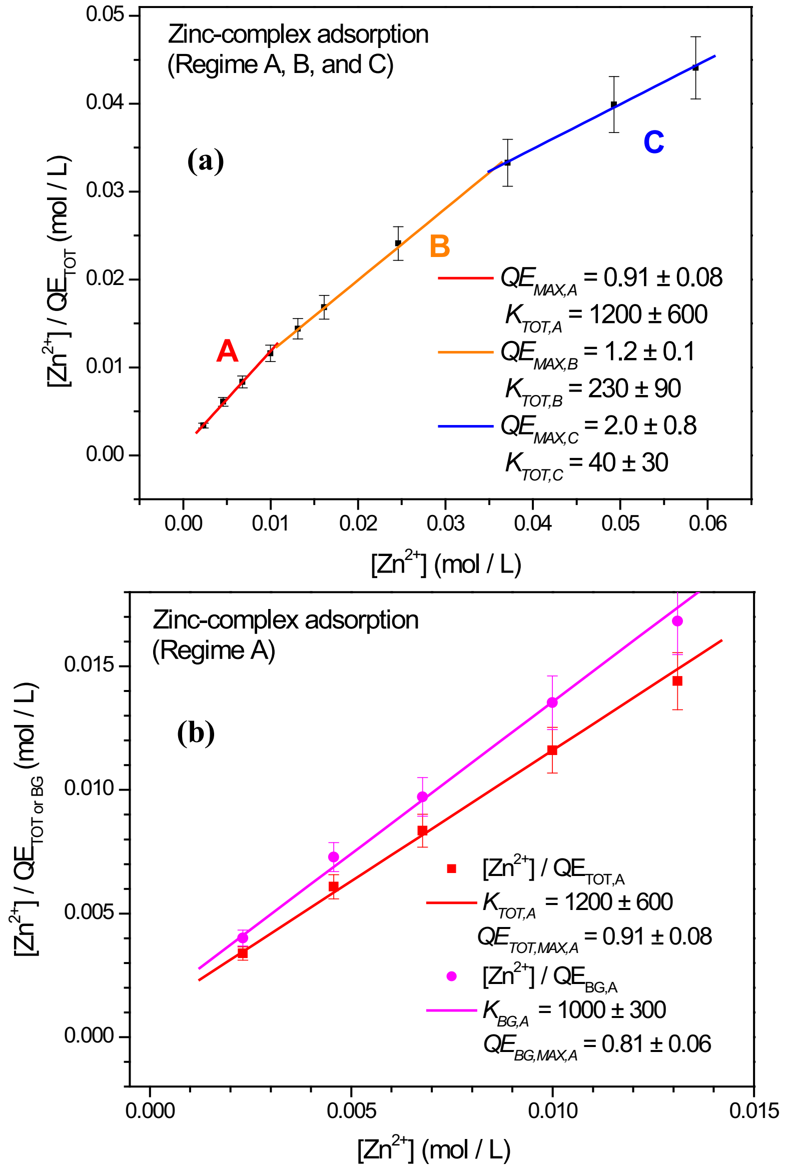

Figure 4.8 Zn adsorption fittings by Langmuir equation. (a) The C/QE_{TOT} fitting at low concentration (regime-A), medium concentration (regime-B), and high concentration (regime-C). (b) Explanation of regime A with separate fits for data derived from total and band-gap PL.

$$\frac{C}{QE} = \left(\frac{1}{KQE_{\max}}\right) + \left(\frac{1}{QE_{\max}}\right)C \qquad (4.2)$$

Clearly, the data plotted in Figure 4.8 (a) are not well fit by a single line, and three linear regimes (A-C) are suggested, corresponding to different regimes of ZND concentration. The low-concentration regime A is re-plotted in Figure 4.8 (b) separately for total QE (QE_{TOT}) and band-gap QE (QE_{BG}). The two isotherms are very similar, as suggested in Figure 4.7. The equilibrium constants were extracted for the total and band-gap data (see eq. 4.2). The values for K_{TOT} (1200 ± 600 $L\cdot mol^{-1}$) and K_{BG} (1,000 ± 300 $L\cdot mol^{-1}$) were within error of one another, suggesting two observations. First, similar adsorption energy (ΔH = -RT*lnK*) was released to enhance total PL and band-gap PL by ZND adsorption. Second, the sites passivated in the low-concentration regime-A are apparently similar.

At higher concentrations of ZND, the adsorption behavior changed. Apparent slope changes occurred at the concentration points of 0.01 $mol\cdot L^{-1}$ and 0.035 $mol\cdot L^{-1}$, respectively. The slope changes also affected the equilibrium constants. The equilibrium constants computed were 230 ± 90 $L\cdot mol^{-1}$ (regime B), and 40 ± 30 $L\cdot mol^{-1}$ (regime C), as plotted in Figure 4.8 (a). A decreasing equilibrium constant also reflected decreasing adsorption energy for the zinc complex onto CdTe QWs. The results suggested the presence of three groups of adsorption sites on the QW surface having different adsorption energies.

The data in Figure 4.7 were also well fit by a Brunauer-Emmett-Teller (BET) isotherm, which is a multilayer (rather than monolayer) adsorption model. This fit found a QE_{max} of similar magnitude as that obtained from the adapted Langmuir model described above. However, the BET model brought no additional insights, and is not presented in detail here. We believe that a monolayer (rather than a multilayer) adsorption model is more scientifically reasonable because of the expected affinity of the expected of the Zn^{2+} centers for surface Te atoms and thiolate groups.

Therefore, the adapted Langmuir model suggested three types of binding site on thiolate-exchanged CdTe QW surface as shown in Scheme 4.3. Unoccupied Te (α) sites on the surface were likely the strongest binding. Thiol-passivated Cd (β) sites were likely the next strongest sites for zinc complex adsorption. Smaller adsorption heat (ΔH) and a lower equilibrium constant (K) from this weaker interaction were also expected. The weakest binding sites are proposed to be TOP-passivated Te (γ) sites. This binding involved the dissociation of TOP and another association process of zinc complex onto the Te site. The adsorption energy to form Zn-Te bond had to be large enough to compensate the dissociation energy to break P-Te bond from the surface. Therefore, we would expect the γ site adsorption to occur only when the concentration of zinc complex was highest. The proposal in Scheme 4.3 is consistent with the adsorption data.

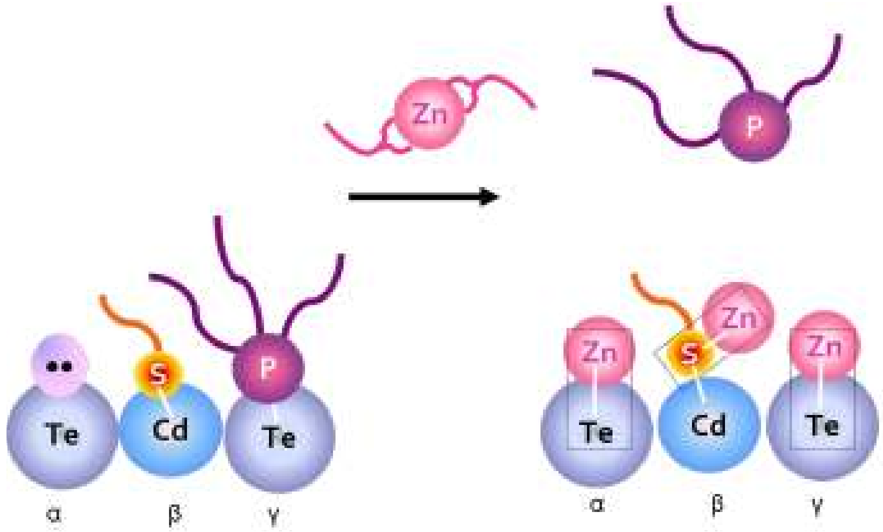

Scheme 4.3 Three proposed binding sites (α, β, and γ sites) for zinc complex adsorption.

4.2.3 Other agent passivation of CdTe QWs

In addition to thiol and zinc complexes, there were other passivating agents available for PL enhancement. Cadmium acetate and water were also passivating agents, but were not as effective as zinc complex and thiol. In this section, a series of experiments were conducted by using cadmium complex and water to enhance the CdTe QW PL.

A $Cd(OAc)_2(octylamine)_2$ complex was prepared by dissolving cadmium acetate into octylamine (concentration of 0.15 mol/kg), and then added to an as-made CdTe QW solution in toluene with stirring. In Figure 4.9 (a), the Cd complex enhanced the CdTe QW PL (green curve) soon after N_2-purging. In a control experiment, octylamine did not enhance the QW PL (red curve). This confirmed that the PL was enhanced by the Cd complex, but not by octylamine Passivation of the surface trap sites (such as Te sites with dangling bonds) was the probable pathway to PL enhancement.

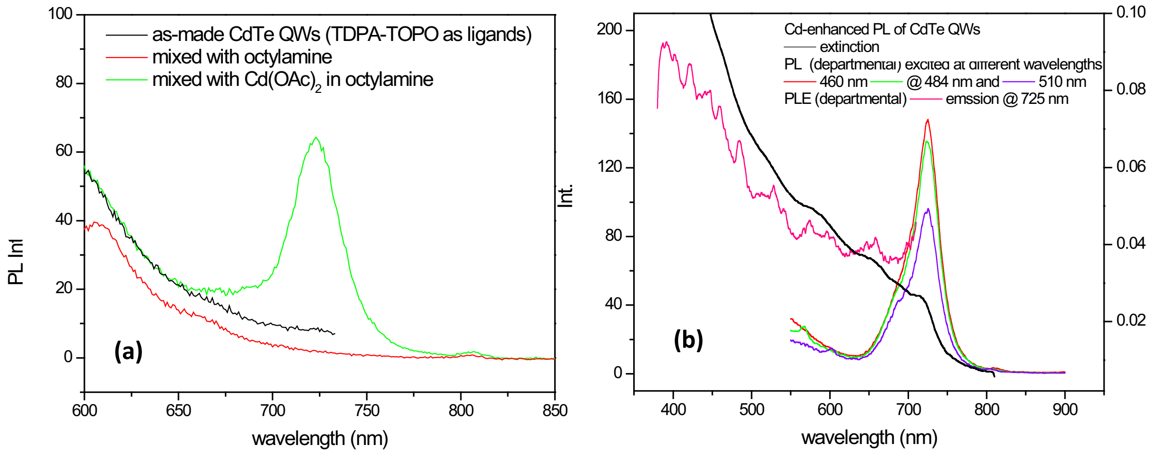

Figure 4.9 PL enhancements by a Cd complex (cadmium acetate in octylamine). (a) PL of as-made CdTe QWs (black), octylamine (OA)-added CdTe QWs (red), and $Cd(OAc)_2(OA)_2$-passivated CdTe QWs (green). (b) The absorption (black), PL (three colors) and PLE (pink) of CdTe QWs after $Cd(OAc)_2(OA)_2$ solution was added.

In Figure 4.9 (b), intense PL with resolved PLE fine structure indicated well passivated surfaces and a decrease in nonradiative recombination. PL emissions by several excitation wavelengths were plotted in different colors. Switching the excitation wavelength from 460 nm to 510 nm lowered PL intensity, which agreed with a smaller cross-section at 510 nm in absorption and PLE spectroscopy.

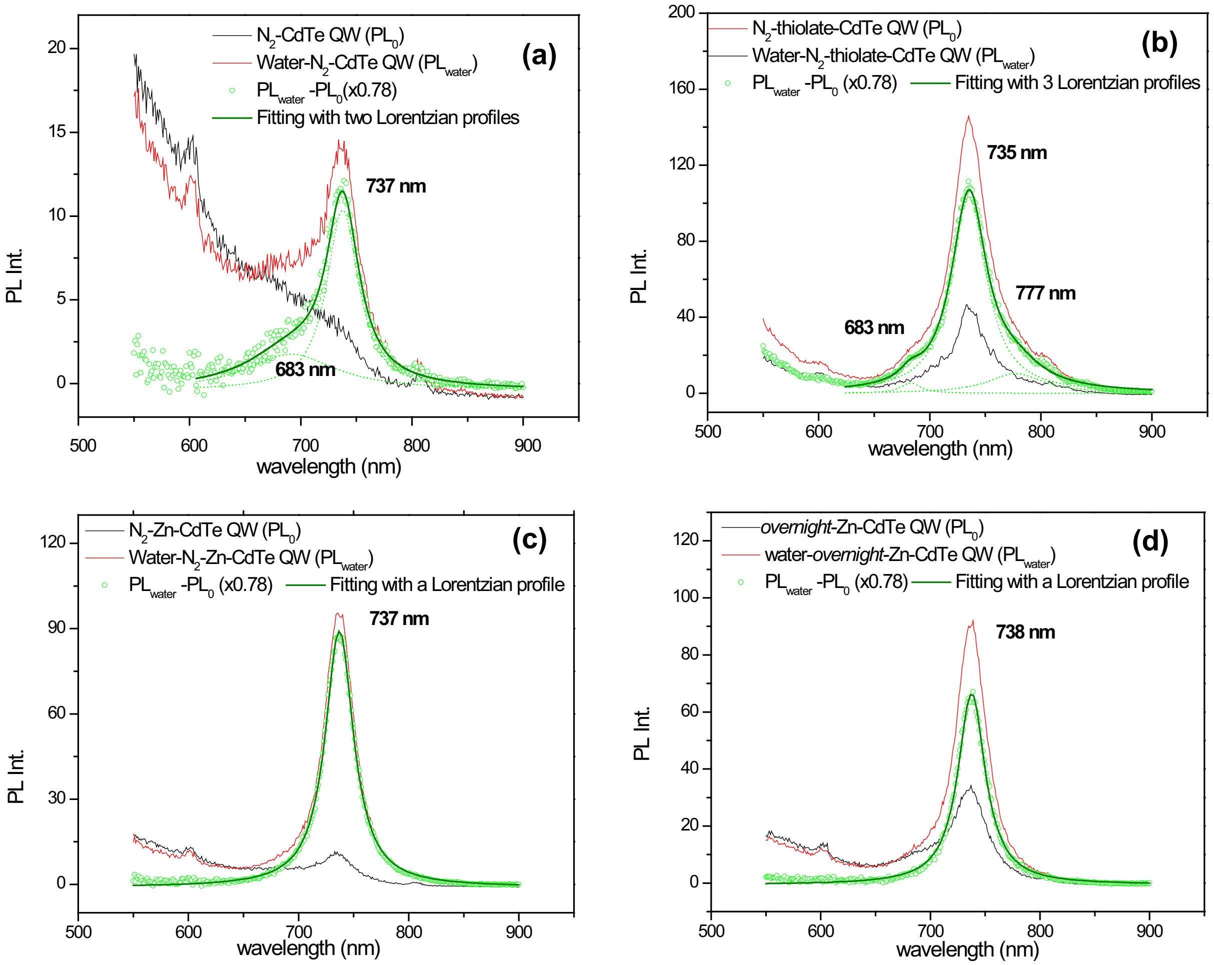

Figure 4.10 PL spectra of CdTe QWs before and after water passivation by air. (a) PL spectrum of N_2-purged CdTe QWs. (b) PL spectrum of N_2-purged thiolate-exchanged CdTe QWs. (c) PL spectrum of N_2-purged ZTT-passivated CdTe QWs. (d) PL spectrum of overnight-ZTT-passivated CdTe QWs. All green dotted curves were fitted by Lorentzian profiles.

Water also enhanced the QW PL. All CdTe QWs were irradiated under an incandescent (tungsten) lamp for 3 h, and then purged with N_2 (at least 40 min) prior to an introduction of water vapor. The CdTe QWs without ligand exchange was denoted as N_2-purged CdTe QWs; the ligand-exchanged CdTe QWs in ethanethiol solution was denoted as N_2-purged thiolate-exchanged CdTe QWs; the zinc-adsorbed CdTe QW in zinc complex (ZTT: diethylzinc-TOP/toluene) solution was denoted as N_2-purged ZTT-passivated CdTe QWs. In the control experiment, the N_2-purged ZTT-passivated CdTe QW standing overnight on the bench prior to the water enhancement was denoted as overnight N_2-purged ZTT-passivated CdTe QWs. In this experiment, water vapor was carried by air flow (O_2 /N_2, v/v = 20/80) and conducted directly in to the QW solution.

Before water/air purging, N_2-CdTe QW exhibits marginally detectable PL, while N_2-thiolate-CdTe QWs and N_2-Zn-CdTe QWs showed some initial weak PL (black curves in Figure 4.10 a-d). After water/air purging for 17 min, the PL of all CdTe QWs was enhanced by different intensity levels (red curve). Water enhancement was assessed by the PL intensity difference ($PL_{water} - PL_0 * 0.78$) in green circles. In Figure 4.10 (a) and (b), 2-3 different Lorentzian profiles (green dot curves) were added-up (as olive color bold curves) to fit the PL intensity difference. In Figure 4.0 (c) and (d), one Lorentzian profile was required to fit the PL intensity difference of N_2-Zn-CdTe QW and overnight-Zn-CdTe QW after water passivation.

The N_2-CdTe QWs and thiolate-CdTe produced PL shoulders after water enhancement. In Figure 4.10 (a), the water-passivated N_2-CdTe QW showed an asymmetric PL shape with shorter wavelength emission (683 nm). However, the water-enhancement was not always observed in N_2-CdTe QWs. As a fact of the difficulty of controlling and measuring water amount on CdTe QW surface, this irreproducibility might be due to the deposition of different amount of water onto the QW. In Figure 4.10 (b), the water-enhanced thiolate-CdTe QW showed both shorter wavelength (683 nm) and longer wavelength emission (777 nm). Thiol and water are Lewis bases, which may passivate the same type of trapping sites on the CdTe QW surface. After water enhancement, the water-thiolate-CdTe QWs showed two side-band emissions, at longer and shorter wavelengths, which were not observed in other water-passivated CdTe QWs.

In Figure 4.10 (c) and (d), the N_2- and overnight Zn-CdTe QW after water enhancement showed mostly symmetrical PL shapes, which were fitted by a single Lorentzian profile. Water vapor carried by air might partially hydrolyze the CdS surface to form CdO shell.[18] Both CdO shell and zinc ion have been found to eliminate the non-radiation recombination of charge carriers on colloidal semiconductors. [18, 16] As a result, zinc-complex passivated QWs gave the best result for water enhancement.

The PL quantum efficiencies were not measured quantitatively in the cadmium-enhancement and water enhancement systems. As noted above, the enhancements with water were highly variable. The enhancements with the cadmium complex were more robust; however, the PL intensities were observed to be an order magnitude lower than in the zinc and thiol enhancement systems. Consequently, neither enhancement strategies were pursued.

4.2.4 Photo-enhancement of CdTe QWs in TOP

TDPA (or ODPA) and TOPO were the original surface ligands of the CdTe QWs. In our strategy, the surface ligands were first exchanged with ethanethiol (ET), and then the thiolated-exchanged QWs were transferred to TOP solution for further photo-annealing. The photo-annealing was initially used to expedite the thiolate exchange or zinc passivation of CdTe QWs. In a subsequent step, another photo-annealing in tri-octylphosphine (TOP) further enhanced the PL intensity of the thiolate-exchanged or zinc-passivated CdTe QWs. Prior to thiol exchange or zinc passivation processes, TOP scarcely enhanced the PL of the as-made CdTe QWs. The thiolate-exchanged QWs demonstrated a non-linear enhancement correlation in TOP solution with the photo-annealing time, as showed in Figure 4.11.

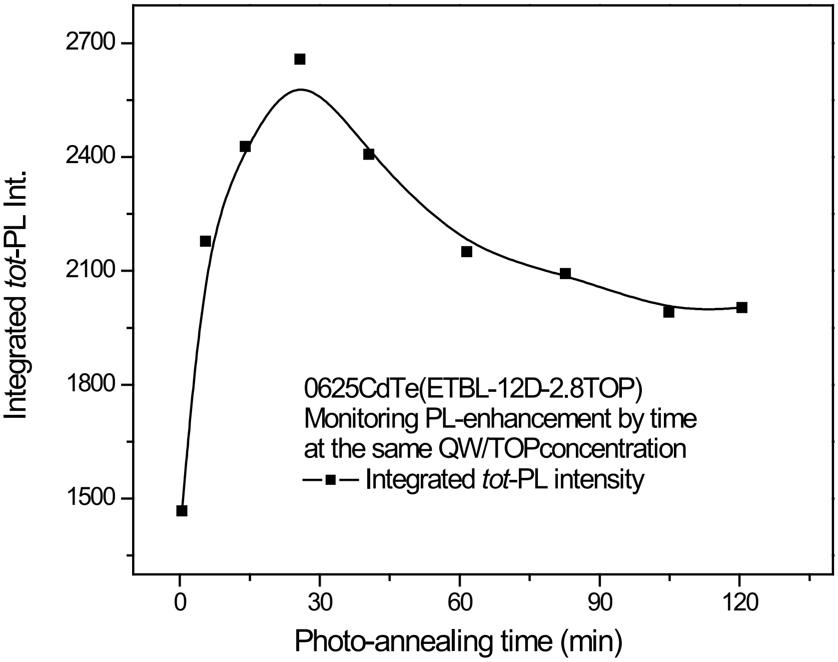

Figure 4.11 Photo-enhancement by a 100-W incandescent bulb of TOP-thiolate-exchanged CdTe QW PL as a function of time.

The first question was how quickly photo-enhancement was completed in TOP solution. We began experiments with a TOP-toluene solution (2.8 % w/w) to monitor photo-enhancement as a function of time. In Figure 4.11, the QE of an as-mixed thiolate-CdTe QW in TOP solution was 0.91 %, which always depended on the TOP concentration. During the photo-annealing, the integrated PL intensity increased more than 80 % (~1500→ ~2700) within the first 30 min, and then gradually decreased to a stable level after 120 min. We assumed that absorption cross-section of TOP-thiolate-CdTe QW remained unchanged during the photo-annealing process. Therefore, the QE enhancement should be equal to the PL intensity area ratio (η) of the photo-annealed *tot*-PL over the original *tot*-PL_0. The photo-enhancement ratio at 30-min (η_{30} = *tot*-PL_{30} / *tot*-PL_0 =1.81) was significantly larger than the enhancement ratio at 120-min (η_{120} = *tot*-PL_{120} / *tot*-PL_0 =1.36). Longer photo-annealing time actually bleached some enhanced PL.

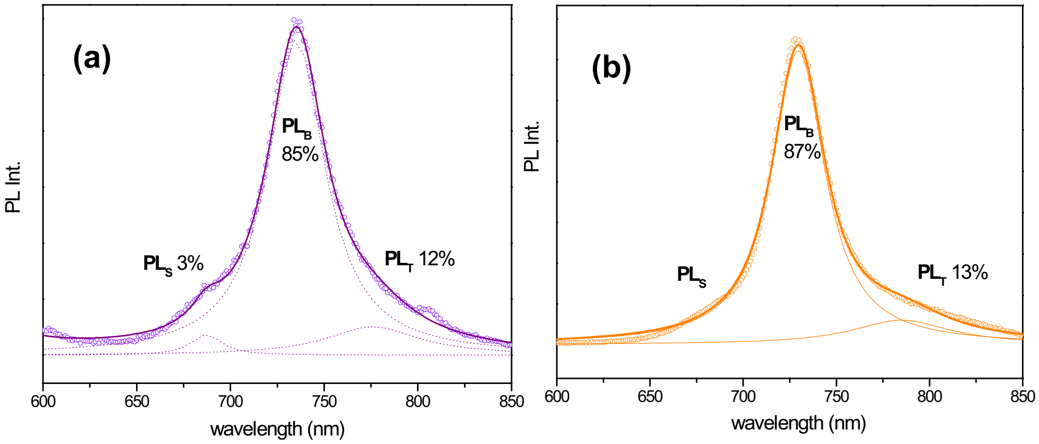

Figure 4.12 The de-convolution of CdTe QW PL emissions. (a) Thiolate-exchanged CdTe QWs. (b) Photo-annealed TOP-thiolate-exchanged CdTe QWs. The dotted curves were Lorentzian fittings for band-gap emission (PL_B), shorter wavelength emission (PL_S) and longer wavelength emission (PL_T).

Generally speaking, the shapes of the PL features of thiolate-exchanged CdTe QWs and photo-annealed TOP-thiolate-exchanged CdTe QW were quite similar. In Figure 4.12, the PL emission of thiolate-exchanged CdTe QWs was fitted with three Lorentzian functions at 731 nm (PL_B, 85 %), 770 nm (PL_T, 12 %) and 680 nm (PL_S, 3 %), which were correspondingly observed in photo-annealed thiolate-exchanged CdTe QW PL spectra.

Another interesting question was how the total emission intensity (*tot*-PL) and the band-gap emission intensity (PL_B) responded to the photo-enhancement. The study was conducted with thiolate-exchanged CdTe QWs and photo-enhanced TOP-thiolate-exchanged CdTe QWs in TOP solution. During short time period of the spectroscopy measurement, a significant PL enhancement was observed. Both *tot*-PL and PL_B were also normalized to their initial PL intensity and plotted as a function of PL-measurement time. In Figure 4.13 (a), the red dots represented the PL_B, and green circles represented the *tot*-PL of the as-mixed thiolate-exchanged CdTe QWs in TOP solution. Each PL-measurement took 105 sec with a break time of 70 sec. Therefore, the interval time between two consecutive scans was 185 s (= 105 s + 70 s). Based on the 1st and 2nd enhanced PL intensities, the *tot*-PL increased 7% and the PL_B increased 9%. Both *tot*-PL and PLs kept gradually increasing during these PL measurements. After the 7th run of PL measurement, the *tot*-PL increased 26% and the PL_B increased 31%. This enhancement was quite impressive since we did not expect such significant enhancement in a short time period.

Similar experiments were conducted to the "photo-enhanced" TOP-thiolate-CdTe QWs in the TOP solution. In Figure 4.13 (b), the orange dots represented the PL_B, and purple circles represented the *tot*-PL of the photo-annealed TOP-thiolate-exchanged CdTe QWs in TOP solution. Based on the 1st and 2nd enhanced PL intensities, the *tot*-PL increased 9 % and the PL_B increased 12 %. Both *tot*-PL and PLs kept gradually increasing during these PL measurements.

After the 8th run of PL measurement, the *tot*-PL increased nearly 33% and the PL$_B$ increased 40%.

The experiments suggested that PL of TOP-thiolate-exchanged CdTe QW was enhanced by photo-annealing from few minutes up to two hours. The TOP-thiolate-exchanged CdTe QW reached its optimized PL intensity at 30 min, and gradually bleached in the following 1.5 hours. Both *tot*-PL and PL$_B$ possessed similar enhancement kinetics. All experiments were conducted at the same TOP concentration. Using different TOP concentrations might accordingly change the PL intensities and corresponding quantum efficiencies.

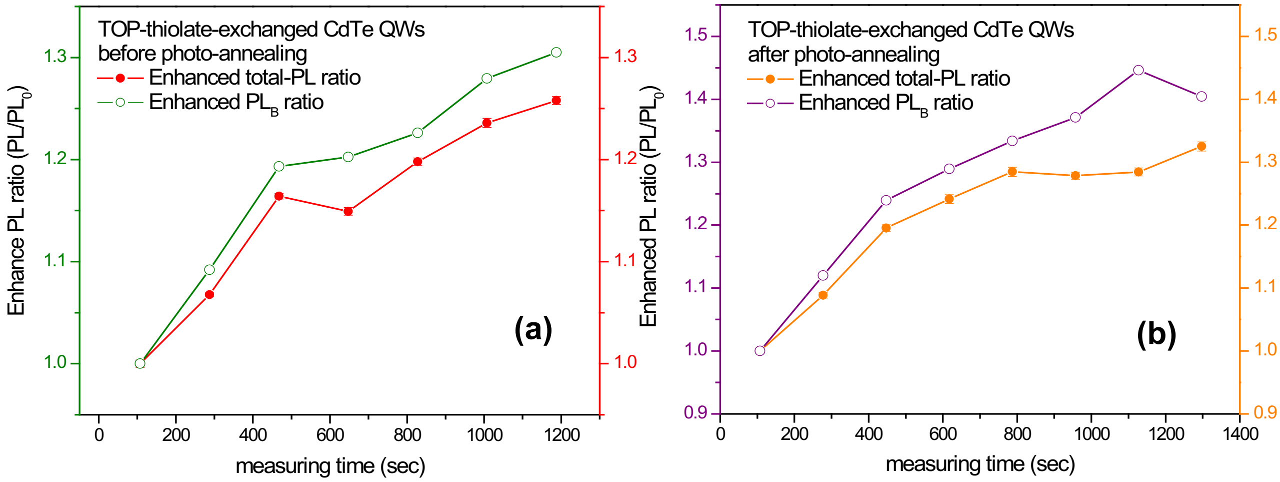

Figure 4.13 Photo-enhancement during the PL measurement (a) Photo-enhancement ratios of *tot*-PL (red dots) and PL$_B$ (green circles) for as-mixed thiolate-exchanged CdTe QWs in TOP solution. (b) Photo-enhancement ratios of *tot*-PL (orange dots) and PL$_B$ (purple circles) for the "photo-annealed" TOP-thiolate-exchanged CdTe in TOP solution.

TOP was used commonly in every step of the passivation process. First, a TOP solution was used to purify the thiolate-exchanged QWs by removing excess thiol from the solution. Second, TOP maintained high PL with longer shelf lives by reacting with O_2 and other possible quenchers. Most importantly, TOP successfully enhanced the PL of the thiolate-passivated CdTe QWs to a significant QE of ~8 % (see below). The QE measurements were individually conducted by using TPP (QE ~ 7%) and Rhodamine 6G (QE = 95 %) as the standard references. The Rhodamine 6G calibrations for CdTe QWs and the QE measurements were conducted by Jessica Hoy, whom we thank.

4.2.6 Photoluminescence of passivated CdTe QWs

Thiols, TOP and zinc complexes demonstrated a cumulative PL enhancement of CdTe QWs. An optimized PL enhancement was conducted by a sequence of thiol-exchange, TOP photo-annealing and zinc-complex passivation processes. The original PL of the TOP-thiolate-exchanged CdTe QWs was fitted with two emissions peaked at 728 nm (band-gap, PL_B) and 681 nm (short-wavelength, PL_S) by Lorentzian profiles in Fig 4.14 (a). The Lorentzian profiles quantitatively produced effective emission percentage (χ equaled to PL_S or PL_B emission intensity over the total PL intensity) for TOP-thiolate-exchanged CdTe QWs. After zinc complex (ZND, zinc *neo*-decanoate) was added, the total PL increased. The enhanced total PL intensities were primarily given by the enhanced band-gap emission (PL_B), as shown by the increment between the purple and green dotted curves centered at 728 nm. Little enhancement was also given by the shorter wavelength emissions (PL_S). However, the origin of the PL_S (670-690 nm) has not been determined.

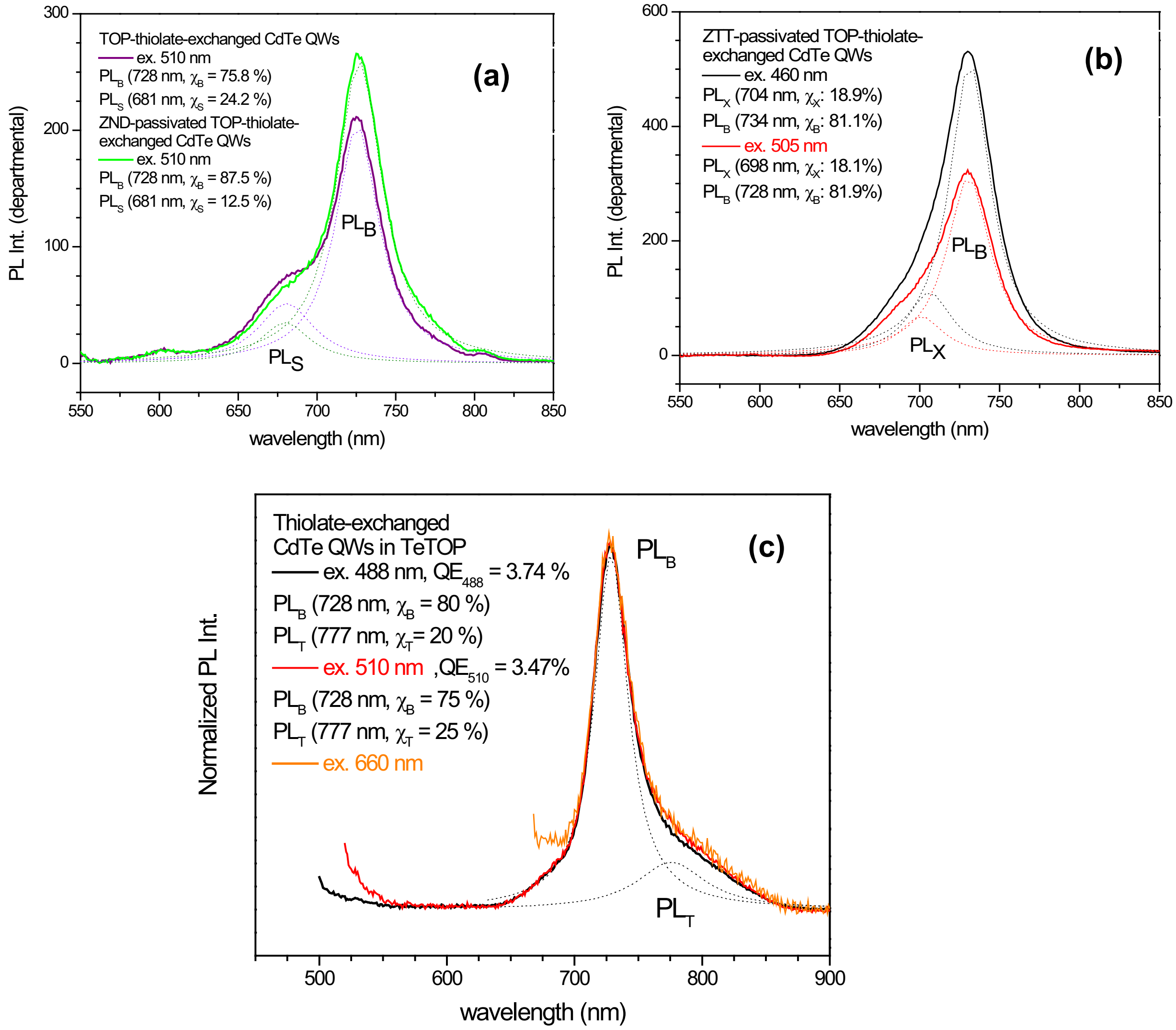

Figure 4.14 PL spectra of passivated CdTe QWs with Lorentzian fittings. (a) PL spectrum of thiolate-exchanged CdTe QWs before and after ZND-passivation. (b) PL spectrum of ZTT-passivated thiolate-exchanged CdTe QWs, conducted by excitation wavelengths of 460 and 505 nm. (c) PL spectrum of thiolate-exchanged CdTe QWs in TeTOP, conducted by excitation wavelengths of 488, 510 and 660 nm.

Diethyl zinc in TOP-toluene (ZTT) gave a slightly different PL enhancement. Another shorter-wavelength emission (PL_X) was observed in ZTT-passivated TOP-thiolate-exchanged CdTe QWs in Figure 4.14 (b). This PL_X emission (690-710 nm) was even closer to the band-gap emission (PL_S). The effective emission percentage (χ_S, 81.1-81.9 %) of PL_S did not change by changing excitation wavelength (460 and 505 nm). The same percentage (χ_B) indicated that the exciton recombined in the same pathway, regardless of the kinetic energies coming from different excitation photon energies.

The PL emission shapes excited at different excitation wavelengths were compared after the intensity normalization. In Figure 4.14 (c), three excitation wavelengths (488, 510, and 660 nm) gave nearly identical PL shapes for thiolate-exchanged CdTe QWs in TeTOP. The effective emission percentage (χ_B) of PL_B and the total quantum efficiency (QE) were 80 % and 3.74 %, conducted by 488 nm excitation wavelength. The effective emission percentage (χ_B) of PL_B and the total quantum efficiency (QE) were 75 % and 3.47 %, conducted by 510 nm excitation wavelength. All values were reasonably close to each other.

During our investigation on the emission shoulders, Ms. Jessica Hoy revealed an instrumental calibration issue in the departmental fluorimeter. To verify this issue, she conducted the PL measurements of the same sample in the departmental fluorimeter, the home-built fluorimeter (Prof. Loomis' Laboratory), and in another commercial fluorimeter (Prof. Holton's laboratory). Surprisingly, three PL shapes were still not the same, specifically the intensity distribution at the longer wavelength tail regime (> 750 nm).

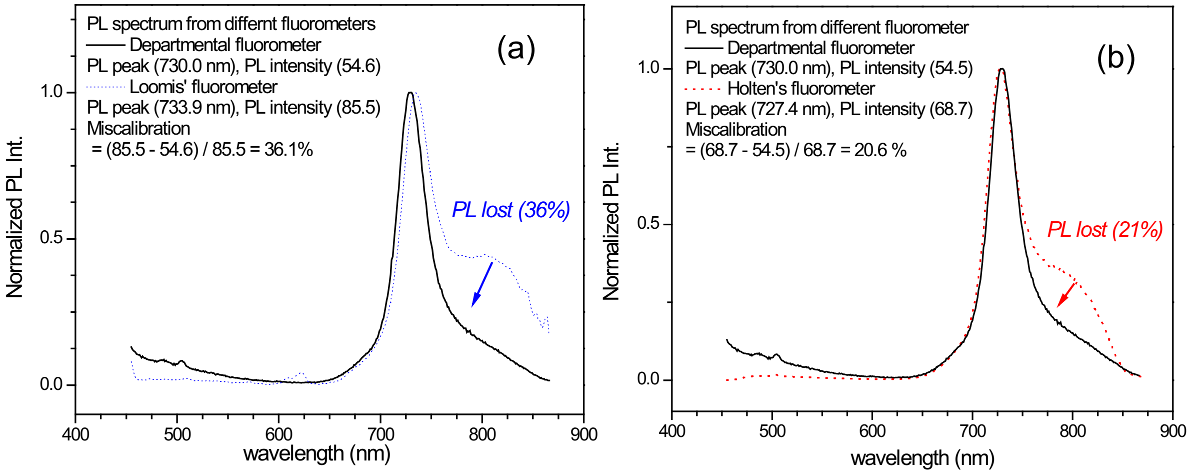

Figure 4.15 PL discrepancies in longer-wavelength emission (PL_T) for TOP-thiolate-exchanged CdTe QWs in TOP. (a) PL spectra collected by the departmental fluorimeter (Varian) and the home-built fluorimeter in Prof. Loomis's lab (taken by Jessica). (b) PL spectra collected by the departmental fluorimeter (Varian) and by another commercial fluorimeter in Prof. Holten's lab (taken by Jessica).

Such a PL discrepancy was due to the miscalibration of the detector response. The departmental fluorimeter seemed to give the lowest response intensity at the longer wavelength shoulder. As shown in Figure 4.15 (a) and (b), the PL collected in the departmental fluorimeter lost 21 % of the total intensity, compared to the PL measurement in Prof. Holton's fluorimeter, or lost 36% of the total intensity, compared to the PL measurement in Prof. Loomis' home-built fluorimeter. This lost intensity was significantly important for the TOP-thiolate-exchanged CdTe QW samples which possessed a large amount of longer wavelength (PL_T) intensity. PL_T formation was related to TOP. During the passivation process, TOP significantly increased PL_T intensities in both CdSe QB and CdTe QW PL emissions.

4.2.7 Epifluorescence of passivated CdTe QWs

These experiments were conducted by Virginia Wayman, whom we thank. In this section, emissions from a single wire or a QW cluster are compared and analyzed with Lorentzian and Gaussian profiles. The PL emission from the confocal experiment shows very similar results to the PL emission from the ensemble experiments. An advantage of the confocal experiments is the collection of emission from individual QW clusters of varying brightness. For an example, whole-bright (*type-A*) and partially-bright (*type-B*) QW-clusters were found in the sample batch. In Figure 4.16, the Lorentzian profile fitted the *type-A* QW emission better than the Gaussian profile, for the peak intensity and shoulder tailing. The peak was fitted at 1.705(8) eV by Lorentzian profile and 1.705(2) by Gaussian profile.

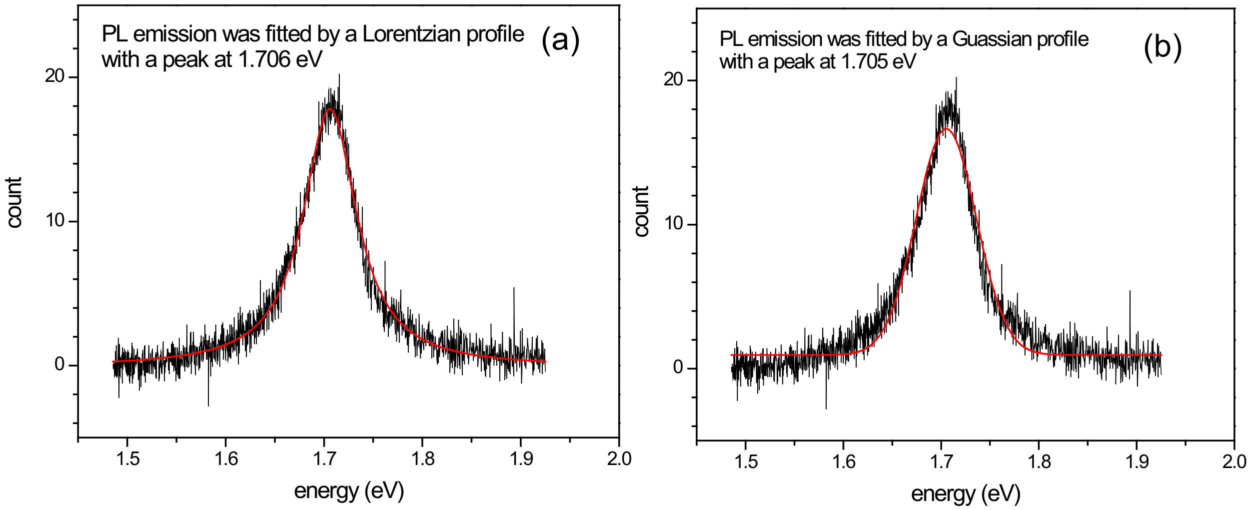

Figure 4.16 Single-wire emission of fairly bright TOP-thiolate-exchanged CdTe QWs (type-A, whole wire emission) collected by a confocal microscope. (a) A Lorentzian fitting curve. (b) A Gaussian fitting curve.

In Figure 4.17 (a), both Gaussian and Lorentzian profiles closely fitted *type-B* QW emissions. Lorentzian fitting showed three peaks at 1.797 eV, 1.699 eV (PL_B) and 1.599 eV.

The energy difference between two adjacent emissions was 98 meV and 100 meV, as re-plotted in Figure 4.17 (c). In Figure 4.17 (b), Gaussian fitting showed three peaks at 1.796 eV, 1.700 eV (PL_B) and 1.603 eV, as re-plotted in Figure 4.17 (d). The energy difference between two adjacent emissions was 96 meV and 97 meV. The PL emissions from both QW-clusters were normalized and re-plotted in Figure 4.17 (c-d). Notice that a little PL_B red shift (~ 5 meV) from the *type-A* QW to the *type-B* QW. Two side-band emission features became dominant in the total PL emission of *type-B* QW.

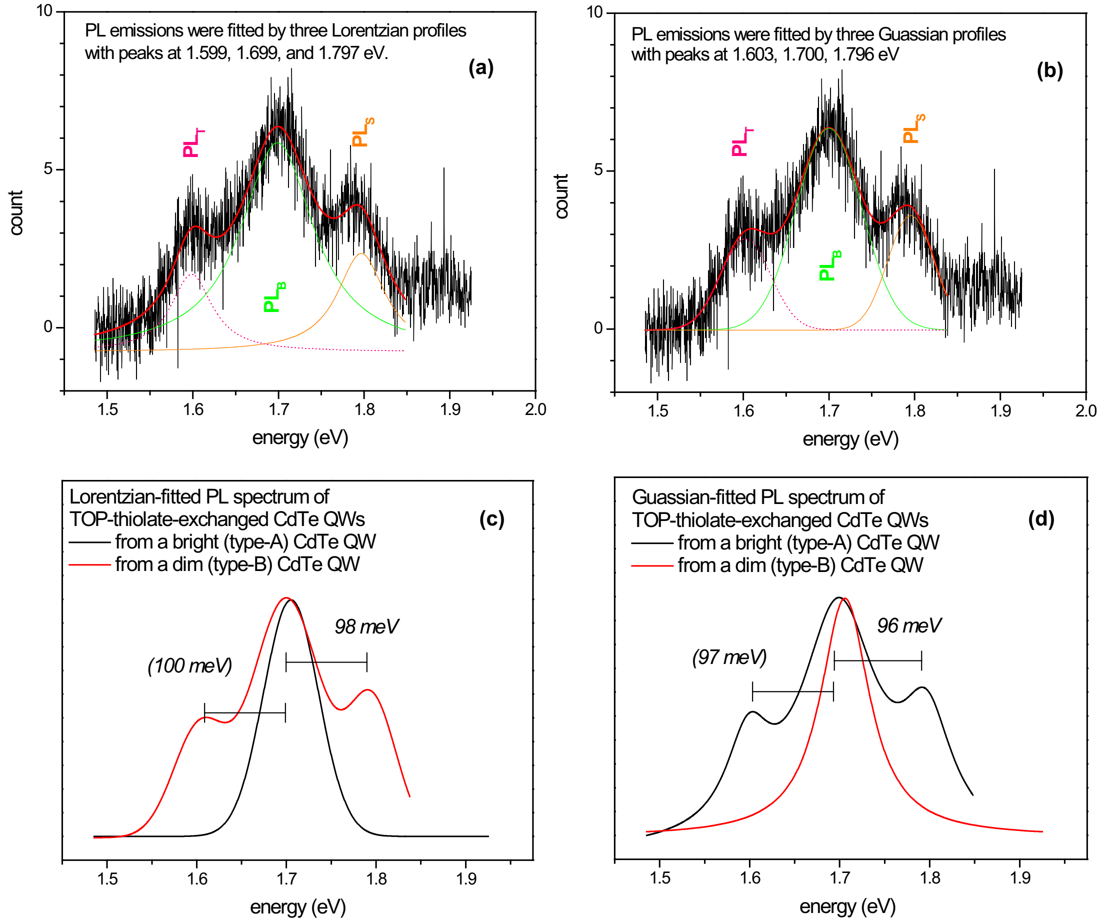

Figure 4.17 Single-wire emissions of dim TOP-thiolate-exchanged CdTe QWs (type-B, partially bright) collected by a confocal microscope. (a) Lorentzian fitting curves. (b) Gaussian fitting curves. The emission comparisons between the whole-bright (*type-A*, black curve) and the partially-bright (*type-B*, red curve) CdTe QWs from epi-fluorescence. (c) Both emissions are fitted with Lorentzian profiles. (d) Both emissions are fitted with Gaussian profiles.

Both types of CdTe QW images and emissions were observed in the same sample. *Type-A* QWs, as in Figure 4.18 (a), behave like a whole-bright emitters. The energy profile taken from the top of the wire looks very similar to the energy profile from the bottom of the wire. The homogeneity of the emission energy was due to the delocalization of the exciton recombination. *Type-B* QWs, as in Figure 4.18 (b), behave like partially-bright emitters. The energy profile taken from the top of the wire (orange curve) was slightly blue shifted to the energy profile taken from the bottom of the wire (green curve), and also possessed a shoulder at the high energy side. In addition, there was a distinct intensity discontinuity at the middle of the wire, indicating the boundary of the delocalized recombination.

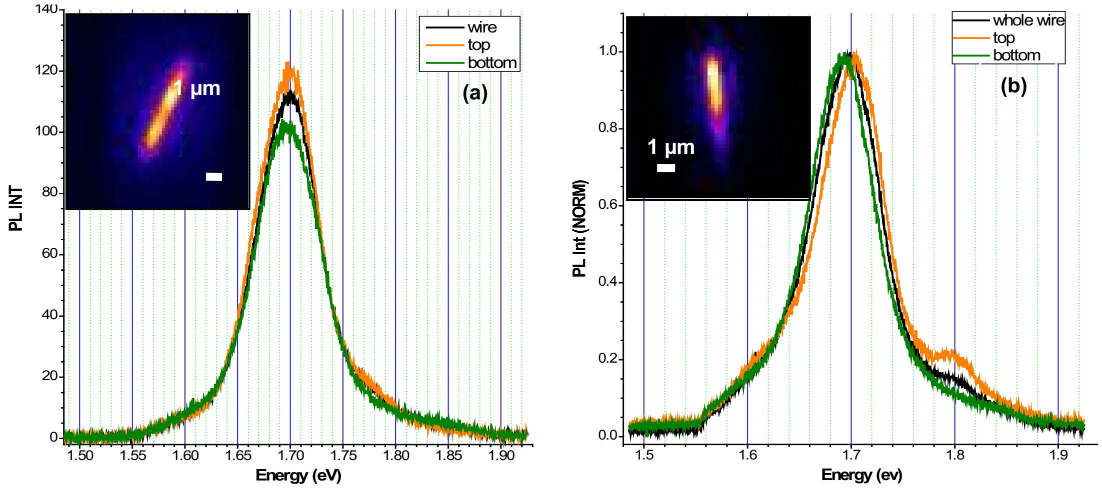

Figure 4.18 The epi-fluorescence emissions with images of TOP-thiolate-exchanged CdTe QWs. (a) Type-A CdTe QW: a delocalized emission of the whole QW. (b) Type-B CdTe QW: localized emission of the whole QW.

The passivation with thiol, TOP and zinc complex was conducted in a homogenous solution, which should give a uniformly passivated QW surface. For type-B QWs, the high energy feature indicated an additional localized confinement regime underlying the bright band-gap emission, which may not be correlated to the surface passivation. Therefore, I propose that the high-energy shoulder was due to the transverse recombination from the ZB/WZ segment alternations in CdTe QWs.[15] In other words, the distinct intensity discontinuity revealed the beginning of the ZB/WZ alternations at the middle of the wire.

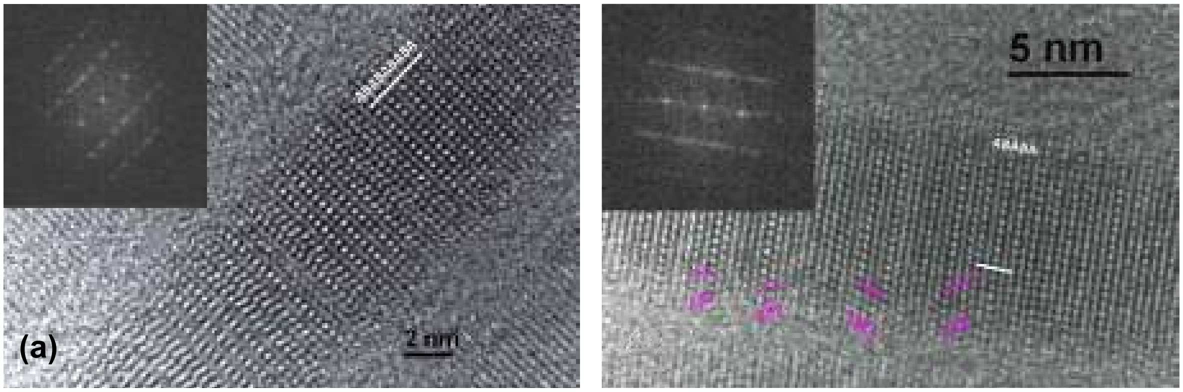

Figure 4.19 Representative HRTEM images of CdTe QWs of 7.39 nm. (a) Most wurtzite structure. (b) Wurtzite and zinc blend alternation. These HR-TEM images were collected by Dr. Fudong Wang, whom we thank.

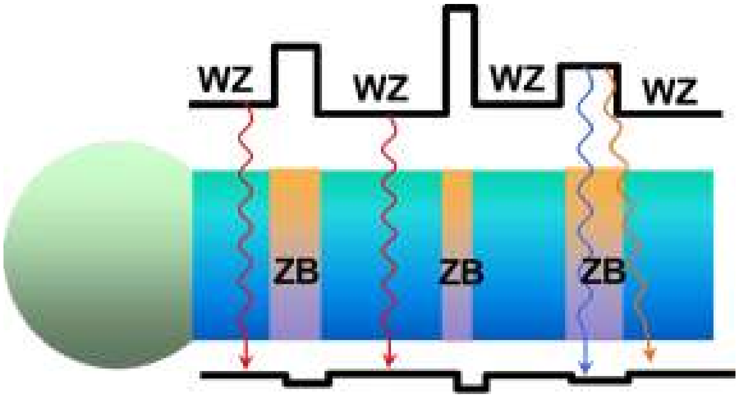

Scheme 4.4 A schematic of band-gap variation caused by crystal phase alternation in a CdTe QW. Three possible recombination mechanisms: direct recombination within WZ domain (red) or within ZB domain (blue), and transverse recombination between ZB CB-level and WZ VB-level.[20-21]

Representative HR-TEM images of 7.39 nm CdTe QWs are shown in Figure 4.19. The diameter distribution was in the range of 7-13%, which is narrow for semiconductor QWs grown by the SLS mechanism. The lattice alternation of two crystal phases (WZ/ZB) were herein observed in HR-TEM images, as analyzed by Dr. Fudong Wang. Based on 18 wires, Dr. Wang reported that the average WZ and ZB lengths for CdTe QWs were 7.0 ± 5.6 nm and 1.9 ± 1.6 nm, respectively, which gave a volume WZ/ZB ratio = 3.7 ± 4.3. The structural analysis results have no major difference from those of CdSe QWs previously published: [19] average WZ lengths (7.0 ± 4.2 nm), ZB lengths (2.7 ± 1.6 nm) and the volume WZ/ZB ratios (2.6 ± 2.2) of CdSe QWs. Such WZ/ZB alternation is common in semiconductor QWs.[19] The phenomenon of shoulder emission is fundamentally interesting. These shoulder emissions may originate as shown in Scheme 4.4.

At the interface of WZ/ZB alternations, electrons confirmed in zinc blende segments can recombine radiatively with holes in adjacent wurtzite regions of a QW, in a transverse recombination.[20-21] The CdTe wurtzite structure has band-gap energy of 1.65(3) eV at 2 K and 1.47(3) eV at 300 K (Scheme 4.5). Surprisingly, the CdTe zinc blende structure has smaller band-gap energy of 1.60(6) at 2K, but larger band-gap energy of 1.51(4) eV at 300 K (Scheme 4.4). The transverse energy difference is 41-53 meV (or ~24 nm) at 300 K.[22-24]

We propose that the electrons and holes in wurtzite segments recombine radiatively in CdTe QWs to produce the primary band-gap emission (Scheme 4.5). Recombination in the ZB segments will be shifted to high energy at room temperature. Similarly, a ~100 meV blue-shift from the band-gap emission of CdTe QWs might come from the transverse recombination pathway (Scheme 4.4). Thus, the high energy shoulder may be due to some combination of ZB-

ZB and ZB-WZ recombination. The low energy shoulder may be due to trap emission, or some other origin.

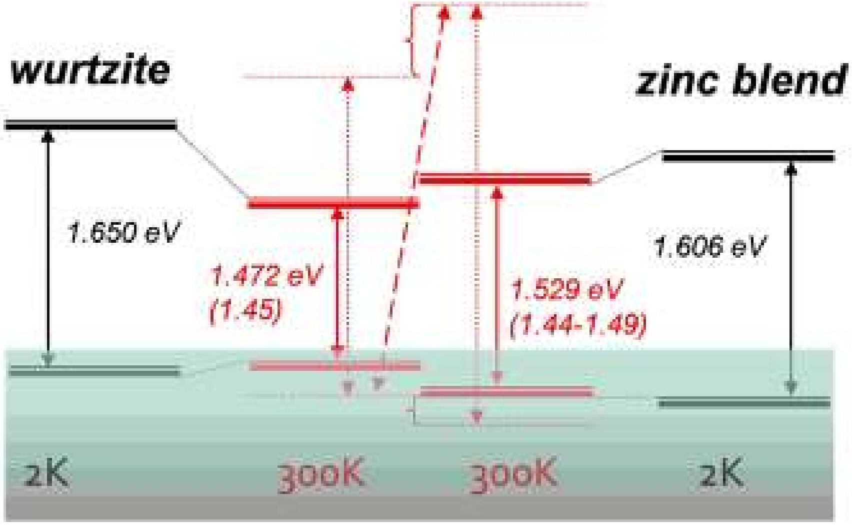

Scheme 4.5 A schematic band-gap levels of wurtzite and zinc blend CdTe structures at 2k and 300K. At 300K, different quantum confinement energy levels (dot-levels) were qualitatively estimated for wurtzite and zinc blend CdTe QWs, corresponding to a smaller Bohr radius (6.8 nm) for zinc blend CdTe and larger Bohr radius (7.5 nm) for wurtzite CdTe.

4.2.7 Photoluminescence excitation (PLE) of passivated CdTe QWs

The PLE resolution was primarily determined by passivating agents, but not necessarily by a high QE. TOP-thiolate-exchanged and zinc-passivated CdTe QWs with fair QE (0.5-2 %) were used in the PLE experiments. In Figure 4.20 (a), there was no observable PLE features for as-made CdTe QWs. After adding the thiols, the thiolate-exchanged CdTe QWs were gradually precipitated from the solution with an appreciable QE (0.5-1 %) and PL/PLE features. Further enhancement by photo-annealing was conducted in a TOP-toluene solution (1-20 %, w/w). After photo-annealing, the QE of the passivated CdTe QWs increased to a larger value (> 2 %). In

Figure 4.20 (b), a significant improvement in the resolution of the PLE features was observed. The position of these features compared favorably to the position of the corresponding features in the absorption spectrum.

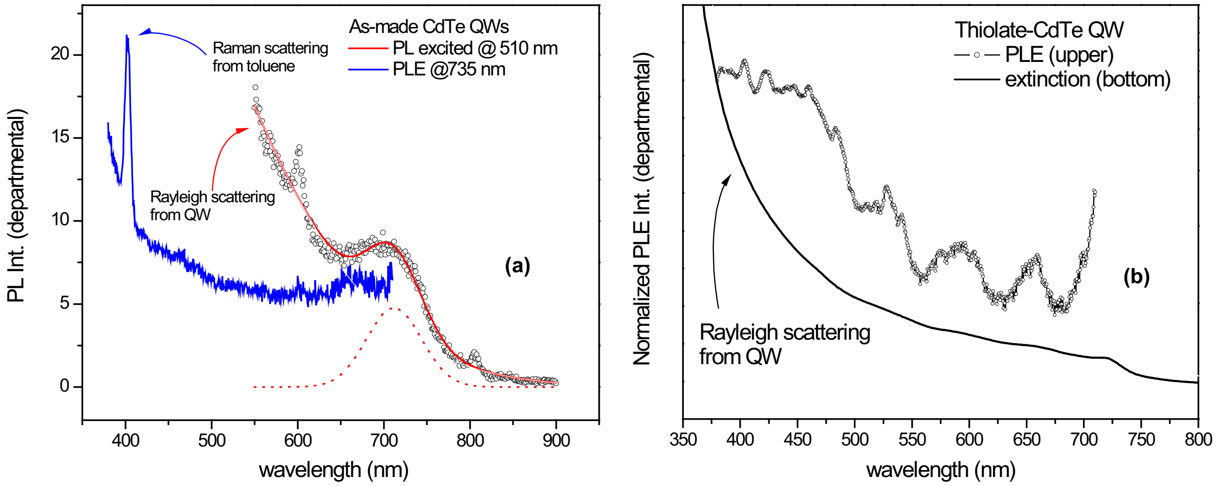

Figure 4.20 PL, PLE, and absorption spectra of CdTe QWs (a) As-made CdTe QWs in toluene. (b) TOP-thiol-exchanged CdTe QWs in TOP-toluene.

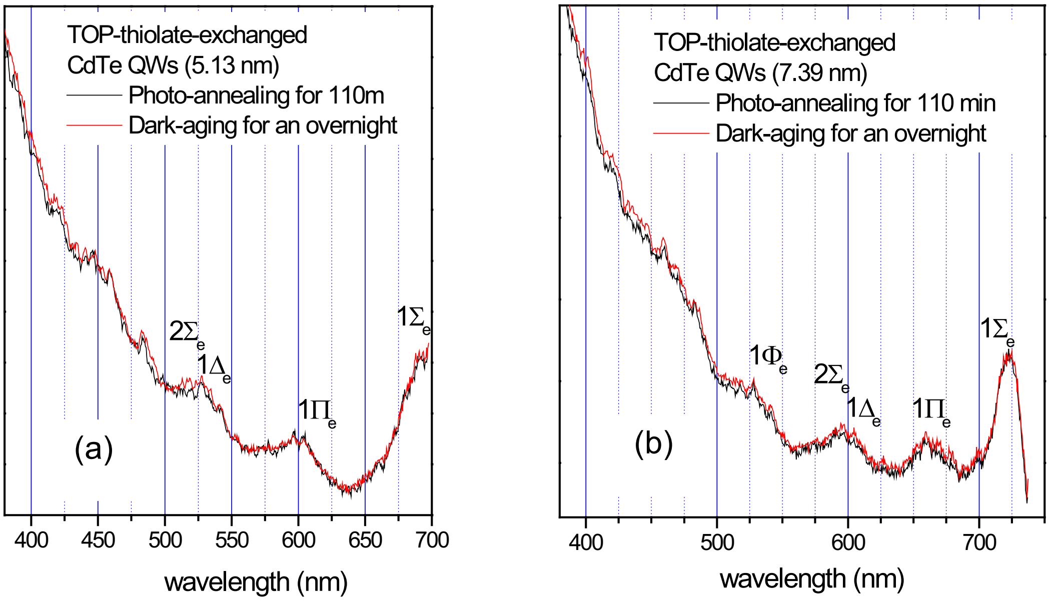

Figure 4.21: PLE spectra of TOP-thiolate-exchanged CdTe QWs of (a) diameter 5.13 nm, and (b) 7.39 nm, in TOP before and after standing overnight in the dark.

The TOP-thiolate-exchanged CdTe QWs of two diameters were also compared in Figure 4.21. In both cases, the QWs were enhanced by photo-annealing in TOP (90%) for 110 min prior to the PLE measurements. Peak features in PLE spectra maintained their original intensities after an overnight dark-aging under air. Multiple electronic transitions were observed in a wavelength sequence of $1\Sigma_e$, $1\Pi_e$, $1\Delta_e$, $2\Sigma_e$, and $1\Phi_e$, from lower to higher energy.[7] The first five transitions were observed in the 7.39 nm QW, but only the first four transitions were observed in 5.13 nm QW.

In Figure 4.22 (a), as-made CdTe QWs showed only a toluene scattering peak (405 nm) in the PLE spectrum. This indicated that surface-trapping sites hindered the exciton radiative recombination, and the PLE features were of insufficient intensity for observation. After introduction of $ZnEt_2$ in a TOP-toluene solution (ZTT), the PLE features and intensities (red curve in Figure 4.22a) were significantly enhanced from the originally dim QWs.

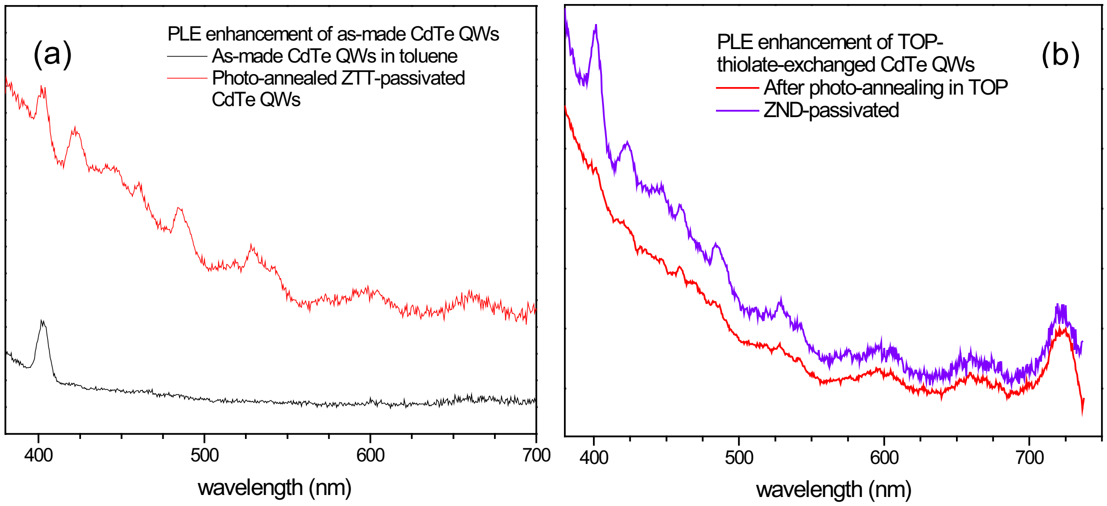

Figure 4.22 PLE enhancements by passivating reagents. (a) The as-made CdTe QWs (N_2-purged) and the ZTT (diethyl zinc)-passivated CdTe QWs (photo-annealed). (b) The photo-annealed TOP-thiolate-exchanged CdTe QWs in TOP (red curve) and after addition of ZND (zinc *neo*-decanoate) toluene solution (violet curve).

Addition of a zinc complex also enhanced the ligand-passivated CdTe QWs. Electron- and hole-trap sites were expected on the CdTe QW surface. After the thiolate-exchange and TOP photo-annealing processes, an enhanced PL might be due to a reduction of electron-trap sites. Since an introduction of zinc complex continued to enhance the QW QE, I expected that hole-trap sites were alternatively passivated by the zinc complexes. In Figure 4.23 (b), the TOP-thiolate-exchanged CdTe QWs were used to examine the PLE enhancement. The zinc complex noticeably enhanced the PLE features. A somewhat noisy baseline was commonly observed in zinc-passivated QWs, especially after photo-annealing.

Well-resolved electronic transitions were observed in ZTT-passivated (Figure 4.23a) and ZND-passivated (Figure 4.23b) TOP-thiolate-exchanged CdTe QWs. The PLE was re-plotted on an energy scale and offset to its 1st excited-state energy corresponding to the band-gap emission. At least 5-6 electronic-transition clusters were clearly observed. Later, these resolved electronic transition features will be compared to these theoretically calculated.[7]

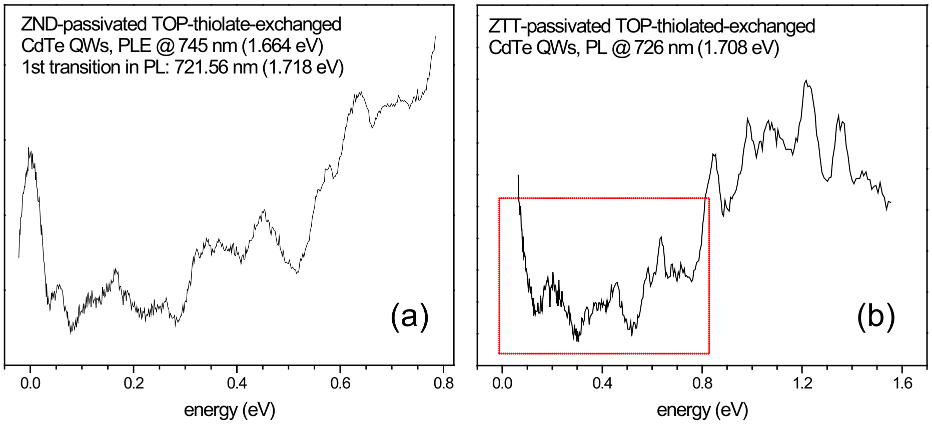

Figure 4.23 Electronic transitions of zinc-passivated TOP-thiolate-exchanged CdTe QW obtained by PLE spectroscopy. The transition energy was offset by its lowest band-gap emission. Two different zinc complexes were used, zinc neo-decanoate (ZND) for (a), and $ZnET_2$-TOP-toluene (ZTT) for (b). The red box in (b) indicated the same range as in (a).

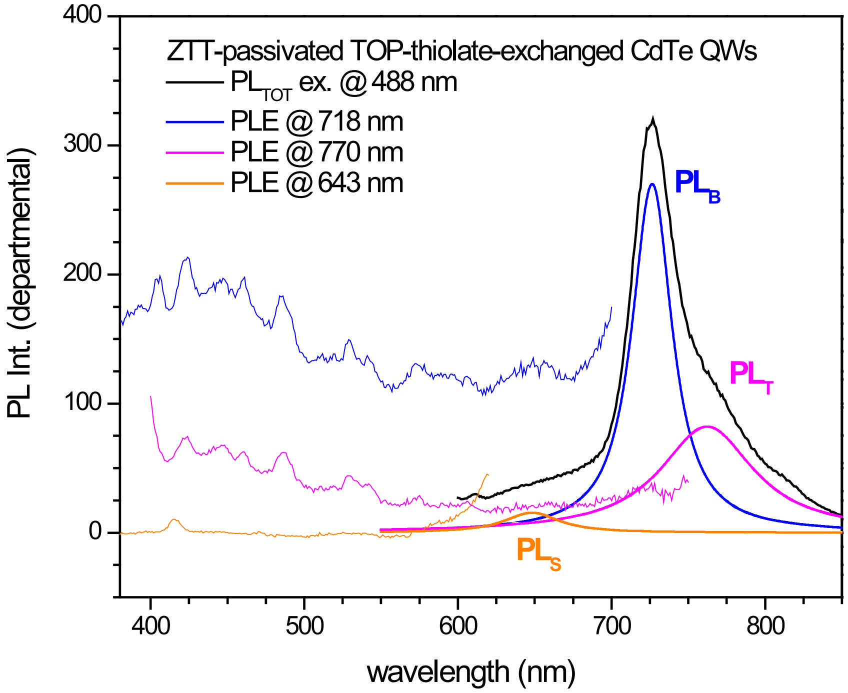

Figure 4.24 Selective PLE measurements of ZTT-passivated TOP-thiolate-exchanged CdTe QWs. Three different emission wavelengths for PLE spectra were peaked at 643, 718, and 777 nm, which were marginally closed to PL$_S$ (648 nm, 4.4 %), PL$_B$ (726 nm, 55.4 %) and PL$_T$ (762 nm, 40%), fitted by three Lorentzian profiles.

Zinc complex (ZTT) was added to further enhance the PL of the TOP-thiolate-exchanged CdTe QWs. The PL intensity increased immediately after adding the zinc-complex solution into the TOP-thiolate-CdTe QW solution. An optimized QE of 3.1% was obtained. The PL (black curve in Figure 4.24) of ZTT-passivated TOP-thiolate-exchanged CdTe QWs consisted of more than one emission. Each emission was accordingly fitted with a Lorentzian profile and three distinct emission regimes were found: shorter-wavelength emission (PL$_S$ < 680 nm), band-gap emission (PL$_B$ = 725-733 nm), and longer-wavelength emission (PL$_T$ > 760 nm). The effective emission percentage (χ) for each fitted peak was 4.4% for PL$_S$, 40% for PL$_T$, and 55% for PL$_B$ in this sample.

According to our observation, the zinc complex significantly reduced the PL_T intensity. There are three possible origins proposed for PL_T. First, a longer wavelength emission (lower energy) was conventionally regarded as trap-site recombination which dissipated the exciton energy and resulted in longer recombination lifetimes. Second, an electron wave-function in a QW might overlap with the adjacent wave-function in an extended-sized QW superlattice.[25] Therefore, the longer wavelength emission might be related to the superlattice (or bundling) of the QWs. Last, the longer wavelength emission might be due to trion emission which was previously observed by Wang et al.[26] However, the origin of the longer wavelength emission (PL_T) is uncertain. The longer wavelength emission (PL_T) was commonly observed in TOP-thiolate-exchanged CdTe QWs and Zn-passivated CdTe QWs. In the previous section, PL_S emission was assigned to a transverse exciton recombination due to the wurtzite and zinc blende alternation in the QWs.[20-21]

In Figure 4.24, three PLE spectra were collected at emission wavelengths of 643 nm (orange curve), 718 nm (magenta curve) and 770 nm (blue curve), individually. Both the blue-curve (collected near PL_B) and magenta-curve (collected near PL_T) showed similarly resolved PLE features with different intensities. However, the PLE collected near the shorter wavelength emission (PL_S, orange curve) did not contain any significant PLE structure, with a noticeable toluene scattering peak around 420 nm. The PLE spectrum of the orange-curve suffered from its low intensity. A low intensity indicates a weaker recombination probability, consistent with a transverse exciton recombination.

A Stokes shift was obtained by comparing well-resolved PLE and PL spectra. In Figure 4.24, the band-gap features were found at 721.6 nm, in comparison to the PL emission at 726.9 nm. The Stokes shift was only 5.3 nm or 13 meV.

An experiment was conducted to determine the possible influence of Te (in the form of TeTOP) on the PL and PLE spectra of the CdTe QWs. In Figure 4.25, a partially resolved PLE spectrum was observed for the TOP-thiolate-exchanged CdTe QWs (black curve) with QE > 1%. After adding zinc-complex (diethyl zinc in TOP-toluene, ZTT) in the QW solution and allowing the sample to stand an overnight on a bench, the QE increased to ~2% without increasing resolution in the PLE spectrum (violet curve). Further photo-annealing did not further enhance the PLE resolution, but slightly bleached the PL intensity. A TeTOP solution was then added. Figure 4.25 (orange curve) shows that the addition had no effect on the PLE spectrum. Similarly, no effect was observed in the PL spectrum of the QWs.

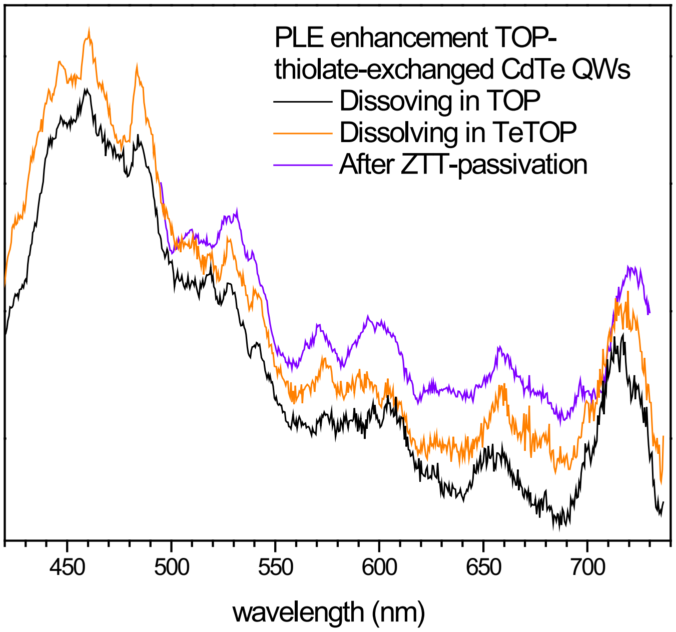

Figure 4.25 PLE spectra of TOP-thiolate-exchanged CdTe QWs (black curve). The PLE spectrum after re-dissolving in TeTOP solution (orange curve). The PLE spectrum after successive passivation with ZTT-complex (diethyl zinc in TOP-toluene, violet curve).

The influence of the various passivating agents on the spectroscopic properties of the CdTe QWs is summarized as follows. Both ethanethiol and a zinc complex individually enhance PL QE and PLE intensity. The zinc complex as $ZnEt_2$ and ZND were similarly effective, but ZND was more convenient to handle. TOP alone did not enhance either PL or PLE, but did further improve PL QE in conjunction with ethanethiol or a zinc complex. The addition of TOP with ethanethiol or a zinc complex did not produce similar improvement in PLE resolution. The largest PL enhancements were achieved by adding the passivating agents in the sequence of ethanethiol, and then concentrated TOP (90%). The best PL QE achieved in this manner was 8%. This issue is further developed in the Discussion section.

4.3 Discussion

4.3.1 Surface passivation strategies for CdTe QWs

In the Results section, several chemicals agents have been proven to successfully passivate CdTe QWs. In Scheme 4.6, two passivation strategies, A and B, are obtained as combinations of successive chemical passivation steps. An optimized QE of ~3% was achieved by strategy A while higher QE of 5-8% was achieved by strategy B. By using these passivation strategies, the CdTe QWs maintain their high QEs with appreciable shelf lives in the atmosphere, which are significantly desirable for QW applications. In the following section, I discuss each passivation process and explain how it affects surface passivation.

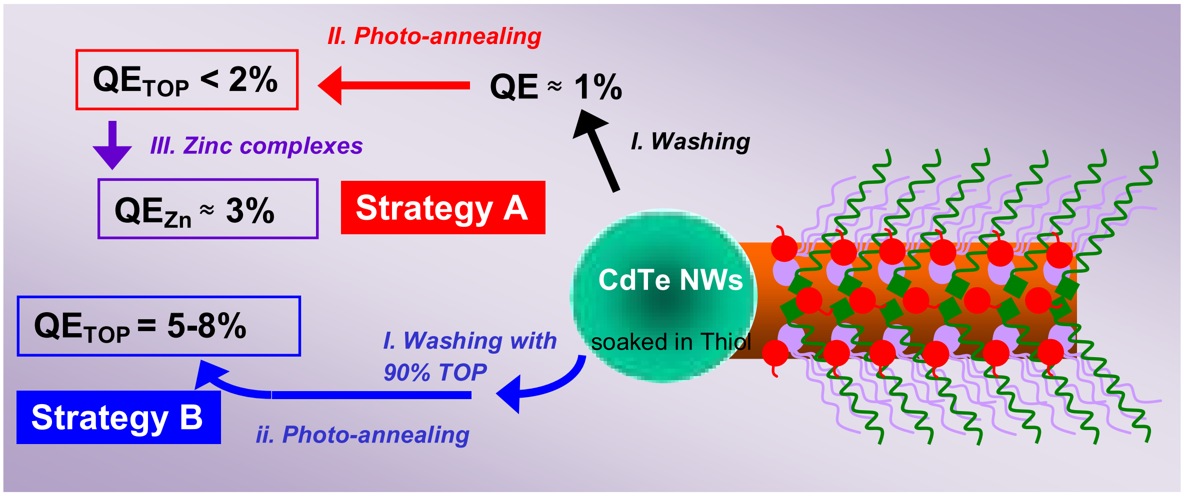

Scheme 4.6 Schematic strategies to passivate CdTe QWs with successive passivating chemicals.

As-made QWs, ligated with TDPA and TOPO, showed marginally detectable PL in toluene with QE lower than 0.1 % (in Figure 4.26a).[20] I suspected that the low QE might be attributed to O_2 adsorption, which generated trap sites and quenched the PL. Oxygen was proposed as one of the photoluminescence (PL) quenchers for as-made CdTe QDs.[27-30] Furthermore in Dr. Jianwei Sun's dissertation, weak PL emission was occasionally observed in the spectra of the as-made CdTe QWs of the smaller diameters (5.4 nm). I suspected that the unexpected diameter-dependent PL efficiency was a coincidence of oxygen dissolution in the QW solution. Therefore, the first step prior to passivation is to avoid O_2 exposure. By appropriately storing CdTe QWs in an inert atmosphere (like N_2), the O_2 quenching issue was completely resolved. A 6-month old CdTe QW sample under N_2 was still active for surface passivation. After appropriate passivation, the QW PL efficiency became less sensitive to O_2 exposure.

CdTe materials have been known as fluorescent sensors to probe oxygen molecules in the air or solution.[27] The triplet state of an O_2-CdTe complex was observed by EPR at room temperature, indicating binding between oxygen and CdTe QDs.[28] ZnTe shells have been reported to effectively eliminate non-radiative recombination in CdTe QDs.[29] However, the zinc-passivated CdTe QWs were still sensitive to O_2 in a TOP-toluene solution. In Fig 4.26 (d), the enhanced PL was quickly quenched by O_2 after a short exposure (few seconds) to the air, and the PL was retrieved after purging with N_2 for a longer time (2-24 h, Figure 4.26 d-f). This phenomenon indicated a reversible PL quenching caused by a reversible adsorption of O_2.[30] Consequently, the zinc passivation was not effective enough to protect the QW surface from O_2 quenching.

Ligand exchange may considerably help to passivate the CdTe QW surface. The literature reported that some CdTe QDs with high QE originally were made in aqueous conditions, in which exposure to O_2 occured.[31-33] Mercapto-based ligands (thiols) were commonly used as surfactants to synthesize these CdTe QDs.[31-33]According to Akamatsu, alkyl thiols may also substantially passivate the CdTe QD surface and protected the QDs from O_2 quenching.[14,34] In a similar manner, an introduction of thiol into the as-made CdTe QW solution indeed increased the QE up to 0.5-1 %. In addition, thiol gives other bonuses for the CdTe QW passivation. First, thiol flocculates as-made CdTe QWs and separates the precipitates from the byproducts after centrifugation. Second, thiol directly enhances PLE intensities. Finally, the thiol-exchanged CdTe QWs become less air sensitive. The slow passivation kinetics (> 12 h) at room temperature was the only concern for thiol exchange, which was expedited by photo-annealing to 30-120 min. After photo-annealing, the thiolate-exchanged CdTe QWs possess a QE of 1-1.5 %. In addition, our study indicates that methanol and *i*-propanol quench the PL as quickly as O_2. Alcohols are frequently used flocculation agents. Fortunately, ethanethiol can replace these flocculation agents, as well as passivate the QW surface in a one-step process.

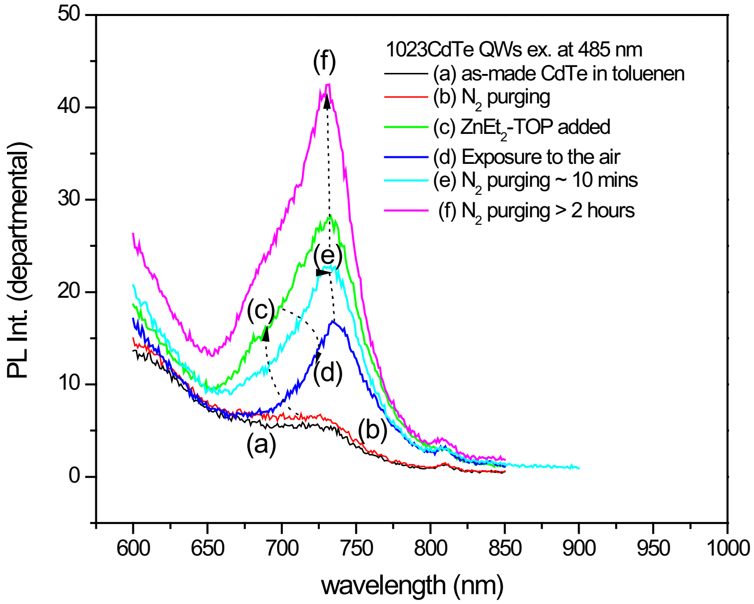

Figure 4.26 PL responses to the environment changes. (a) Original PL spectra of as-made CdTe QWs in toluene. (b) PL spectra of N_2-purged CdTe QWs in toluene. (c) PL spectra of ZTT ($ZnEt_2$-TOP-toluene)-passivated CdTe QWs. (d) PL spectra of ZTT ($ZnEt_2$-TOP-toluene)-passivated CdTe QWs after a short exposure to the air (few seconds). (e) PL spectra after N_2-purging for 10 min; (f) PL spectra after N_2-purging for 2 hours.

In strategy B, the CdTe QWs were passivated with thiol and TOP *without* zinc complex. Higher concentrations of the passivating agents and photo-annealing were both required to optimize the QE. Similar to the thiol passivation in the strategy A, the as-made CdTe QWs were enhanced by soaking as-made QWs in ethanethiol solution, then aging by dark-annealing overnight, or photo-annealing for 2 h. The annealing process allows a reaction time for a completion of thiolate exchange. The thiolate-exchanged CdTe QWs were washed with TOP (90 %) 2-3 times to remove unwanted byproduct. An optimized QE of 5-8 % required an additional photo-annealing step (120 min) in the same TOP solution (90%).

CdTe QW PL QE for two diameters has been successfully enhanced by strategy B. The QW surface was exchanged with ethanethiol and TOP after photo-annealing. In Figure 4.27, the QE of the TOP-thiolate-CdTe QWs was optimized to 5.85 % for 5.13 nm QWs, and 6.30 % (the best QE > 8 %) for 7.39 nm QWs. The TOP-thiolate-exchanged CdTe QW has narrow and strong PL emission, with fairly well resolved PLE features. The band-gap emissions (PL_B) of TOP-thiolate-exchanged CdTe QWs were at 704.5 nm for 5.13-nm QWs, and at 729.6 nm for 7.39-nm QWs. Due to the high PL_B intensity, we observed a longer wavelength emission (PL_T), but not the shorter wavelength emission (PL_S), after Lorentzian profile fits.

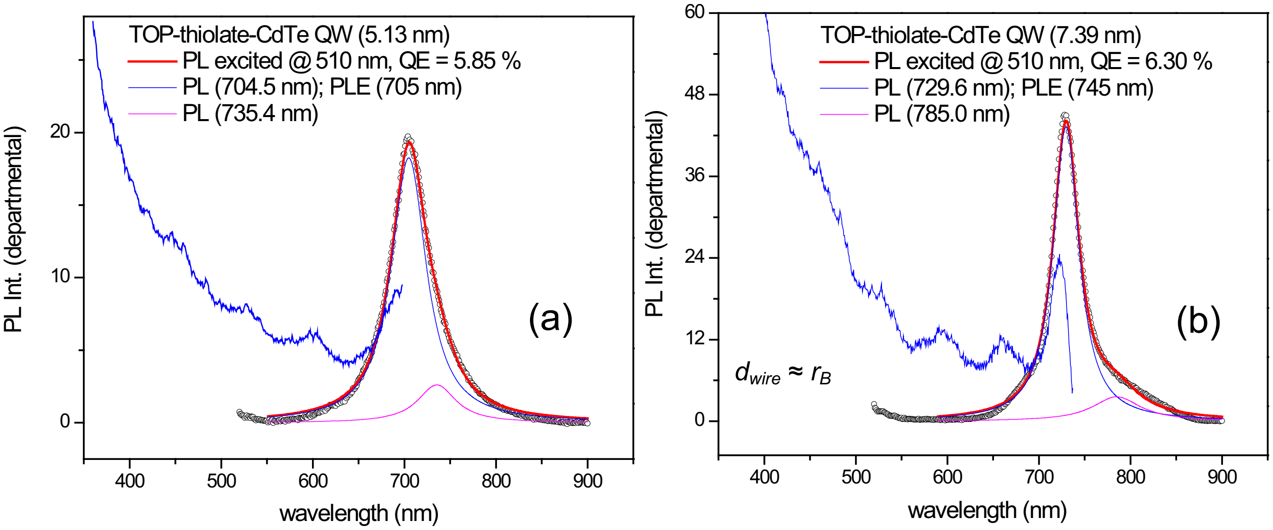

Figure 4.27 PL and PLE spectra of TOP-thiolate-CdTe QWs from strategy B with optimized QE for (a) CdTe QW of 5.13 nm, and (b) CdTe QW of 7.39 nm.

The enhanced CdTe QW PL usually consisted of more than one emission. Each emission was closely fitted by a Lorentzian or a Gaussian profile. There are various kinds of broadening mechanisms affecting the peak width homogeneously and inhomogeneously. The Gaussian profile corresponded to an inhomogeneously broadened line shape. The homogeneously broadened emission line will have a Lorentzian profile. In theory, the QW emission should look like a combination of a Gaussian profile at the higher energy side, and Lorentzian profile at the lower energy side of the peak. However, the shape of the QW emission was also affected by the high- and low-energy shoulders on the band-gap emission. In our previously described experimental results, a Lorentzian profile nicely fitted both single-wire and ensemble emissions of passivated CdTe QWs (Figure 4.17). In this section, we discuss the emission fits of the ensemble emission, in comparison with the single-wire emission from the confocal microscope.

Lorentzian and Gaussian profiles may affect the fitting results in the peak position and the intensity area. In Fig 4.28, the PL of TOP-thiolate-exchanged CdTe QWs was fitted with a Lorentzian profile in wavelength (a) and in energy (b) scales, as well as fitted with a Gaussian profile in wavelength (c) and in energy (d) scales. The tot-PL maxima (728.0 nm) was very close to the band-gap emission peak fitted by both Lorentzian profile (728.7 nm) and Gaussian profile (728.2 nm). However, a large uncertainty of a peak position was left for the longer wavelength emission peak (PL_T) when a Lorentzian profile (776.7 nm) or a Gaussian profile (749.6 nm) was used to fit.

The area under each fitting profile also produced another uncertainty. The PL_T intensity area indicated that some excitons experienced a possible trap-site emission. The PL_T fitted by a Lorentzian function resulted in 20 % for the trap emission when the emission was plotted in wavelength, or 13 % when plotted in energy. Similar uncertainty was also applied to the intensity area fitted with different profiles. The PL_T fitted by a Gaussian function resulted in 56% of the effective emission when the emission was plotted in wavelength, or 60% when plotted in energy. Such a huge discrepancy between Lorentzian and Gaussian fitting results revealed the importance of using an appropriate profile to fit. According to previous results, a Lorentzian was a more reliable profile to comprehensively fit the single-wire PL emission (Figure 4.17a).

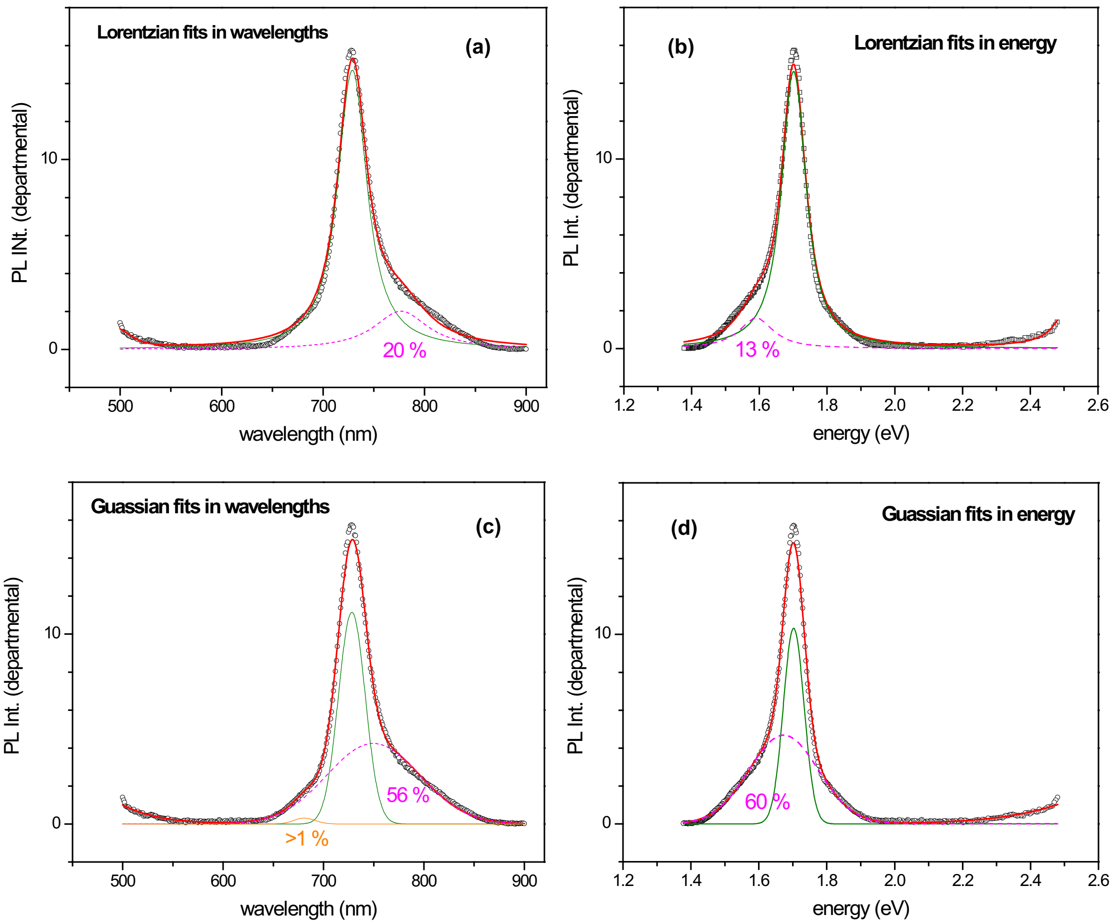

Figure 4.28 Fitting of photo-enhanced TOP-thiolate-CdTe QW PL in TeTOP. (a) Fitted with two Lorentzian functions at 728.7 nm and 776.7 nm. (b) Fitted with two Lorentzian functions at 1.701 eV (728.9 nm) and 1.591eV (779.4 nm). (c) Fitted with three Gaussian functions at 728.2 nm, 680.8 nm and 749.6 nm. (d) Fitted with two Gaussian functions at 1.703 eV (728.0 nm) and 1.673 eV (741.1 nm).

In Figure 4.28 (c), a small area (< 1%) was also occasionally fitted at the shorter wavelength emission (PL_S). This emission had been previously assigned to the exciton transverse recombination between the WZ/ZB alternations.[21] However, this intensity area was negligibly small, in comparison PL_B and PL_L of TOP-thiolate-exchanged CdTe QWs.

4.3.2 Problem of determining reliable QE using extinction data

Various strategies were employed to passivate the CdTe QW surface and to remove the surface trapping sites (or minimum-energy states). The well-passivated CdTe QW surface should result in discrete electronic transitions in the PLE spectrum corresponding to the quantum-confinement energy levels in the QW. A photoluminescence excitation (PLE) spectrum resembles an absorption spectrum, but is generally better resolved. Also, significant Rayleigh scattering occurred at shorter wavelengths (proportionally to λ^{-4}) in the absorption spectrum.

In Figure 4.29, the extinction spectrum showed broad features, while the PLE contained better resolved features. Each feature in the PLE spectrum can be identified as one or more electronic transitions to discrete energy levels in the conduction and valance bands due to quantum confinement. The intensity of each PLE feature also corresponded to the QW absorption cross-section area at its excitation wavelength. If the quantum efficiency (QE) was a fixed value, the PL emission intensity should change proportionally to the absorption cross-section, as shown in Eq. 4.3.

$$QE = \frac{I_\lambda}{A_\lambda} = \left[\frac{\text{PL-intensity}}{\text{cross-section}}\right] \qquad (4.3)$$

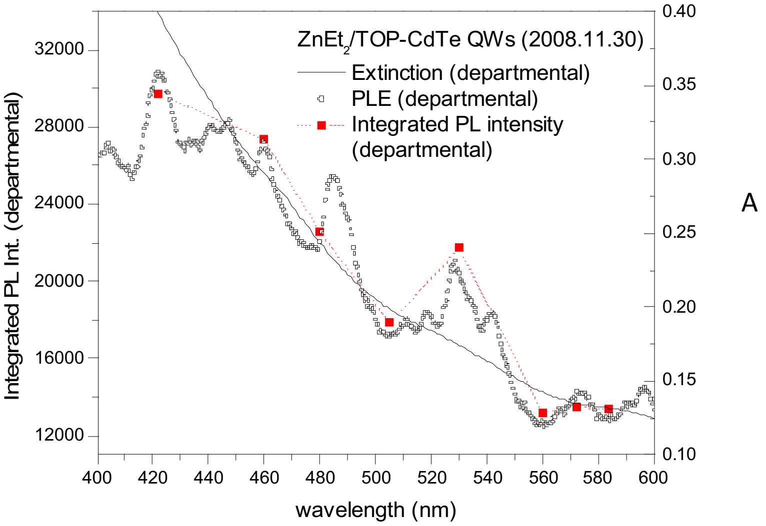

Figure 4.29 Comparisons of PLE and extinction collected at room temperature (~300K). The extinction (black line) of Zn-passivated TOP-thiolate-exchanged CdTe QW was collected in the departmental spectrometer. The PLE (black circles) was collected in the departmental fluorimeter. The integrated PL intensity (red squares) was collected in the departmental fluorimeter with changes of excitation wavelengths.

Equation 4.3 suggests that QE should be independent of the excitation energy. However, in my experience with CdTe QWs, the apparent QE was found to vary with excitation energy by as much as 40%, which seems unreasonably large. I believe this variation was due to the use of incorrect absorption values (cross-sections) obtained from the extinction spectrum. The following experiment was undertaken to demonstrate this problem.

PL measurements were conducted on a QW specimen passivated by strategy A (to ensure the best-resolved PLE spectrum). PL data were collected at excitation wavelengths ranging from 420 to 585 nm. The total integrated PL intensity was background corrected (see Experimental section) and re-plotted in Figure 4.26, along with the extinction and PLE spectra. The three sets of data were vertically scaled to provide the best mutual agreement (overlap). The plot reveals that the PL and PLE data track closely together, but deviate significantly at many wavelengths from the much broader extinction curve. I contend that the extinction spectrum is too poorly resolved to provide accurate absorption values, and that the true absorption cross-sections are much more accurately depicted by the PLE intensities.

Other problems with the quantitative use of extinction data existed. The extinction was significantly increased by Rayleigh scattering at higher energy. Additionally, at higher energy absorption by ligands and passivating agents contributed significantly to the extinction. These issues combined to make the extinction data poor indicators of the true absorption cross-section of the semiconductor core of the QW structure. Consequently, I report QE values obtained at a single extinction wavelength of 510 nm, where the extinction, PL, and PLE data are in closest agreement in Figure 4.29. In my opinion, this condition is most likely to produce reliable QE values.

4.3.3 Electronic structures of passivated CdTe QWs

The size-dependent electronic structures of CdTe QW previously were determined by density functional theory (DFT) using the local density approximation (LDA+C) with a band-corrected pseudo-potential method.[35-36] The absorption features observed experimentally are not discrete transitions but rather clusters of closely spaced transitions. Studies of the electronic structure of semiconductor QDs have compared calculated energy levels with spectroscopic data generally from obtained PLE spectroscopy.[35-36] We herein compare the calculated electronic transitions at the Γ point with experimentally resolved PLE spectra of CdTe QWs.

In the PLE spectra, we monitored the emission wavelength slightly above the lowest band-gap emission. Therefore, the PLE features should correlate to band information of the semiconductor-core wurtzite structure. In Figure 4.30, experimental PLE spectra of 5.13-nm and 7.39-nm diameter CdTe QWs were compared. The arrows indicate clusters of transitions to several excited electron levels. In the PIC model, the electron CB-state energies $E_{n,l}$ are expressed by eq 4.4, where d is the QW diameter, m^*_e is the electron effective mass, and $E_{g,bulk}$ is the bulk CdTe band-gap.[1]

$$E_{n,l} = \frac{h^2k^2}{8\pi^2 m_e^*} + E_{g,bulk} \qquad (4.4)$$

By using the particle-in-a-cylinder (PIC) model, the energies of the CB states relative to the top of the bulk VB can be fitted to a quadratic equation as follows.[7] Non-parabolicity (α) in the conduction band may be addressed by expanding the *k*-space dispersion relation with a fourth-order term in *k* (eq. 4.5). The coefficient α is the isotropic non-parabolicity constant. eq. 4.5 can be rewritten to express a diameter dependence by the substitution $k = 2\varphi_{n,l}/d$ (eq. 4.6).

$$E_{n,l} = \frac{h^2k^2}{8\pi^2 m_e^*} + \alpha k^4 + E_{g,bulk} \qquad (4.5)$$

$$E_{n,l} = \frac{h^2\phi_{n,l}^2}{2\pi^2 m_e^* d^2} + \frac{16\alpha\phi_{n,l}^4}{d^4} + E_{g,bulk} \qquad (4.6)$$

In eq 4.6, $\varphi_{n,l}$ is the nth root (zero) of the cylindrical Bessel function of order l [$J_l(x)$]. The number of the zero, n, functions as a principal (radial) quantum number. The order, l, functions as an angular-momentum quantum number. For the spherical symmetry of QDs, the values $l = 0, 1, 2, 3, 4$, etc. are assigned the conventional symmetry labels *S*, *P*, *D*, *F*, *G*, etc., respectively. However, for the cylindrical symmetry of QWs, these labels are converted to their Greek counterparts: Σ, Π, Δ, Φ, Γ, etc., respectively. Because the CB state energies vary with $\varphi_{n,l}{}^2$, the sequence of CB states follows the sequence of $\varphi_{n,l}$ values, in increasing order of, $1\Sigma_e$ (2.4048) < $1\Pi_e$ (3.8317) < $1\Delta_e$ (5.1356) < $2\ \Sigma_e$ (5.5201) < $1\Phi_e$ (6.3802) < $2\Pi_e$ (7.0156) < $1\Gamma_e$ (7.5883) < …

The theoretical calculations were based on CdTe QWs of 5.3 nm and 7.3 nm.[7] From the experimental synthesis, CdTe QWs of two different diameters of 5.13 nm and 7.39 nm were made (diameter distribution was in the range of 7-13%). CdTe QWs of 5.13 nm were passivated by strategy B (no zinc complex) while CdTe QWs of 7.39 nm were passivated by strategy A (with zinc complex). Both samples showed well-resolved PLE features in Figure 4.30(a) and (b). By fitting several CB-state energies with $\varphi_{n,l}{}^2$, both m^*_e and α are extracted from the coefficients in the quadratic equation (eq. 4.6).

The first black arrow in Figure 4.30 a and b corresponded to the transitions to $1\Sigma_e$ states from three closely spaced hole states. The red arrow indicates the transitions to the $1\Pi_e$ state level. The black and red sets of peaks are consistent with the results of the previous LDA+C calculations of transitions in CdTe QWs as plotted in Figure 4.30 (c) and (d).[7] For 5.13-nm CdTe QW, the hole-level energy difference has been previously calculated to allow subtraction of the hole-level energy from the transition (PLE) energy in Figure 4.30 (a). Consequently, the first three sets of experimental CB-state transitions to $1\Sigma_e$, $1\Pi_e$, $1\Delta_e$ and $2\Pi_e$ satisfactorily matched the theoretical ones in Figure 4.30 (c). A small deviation began from the 4th set of transitions which were indicated by a blue arrow.

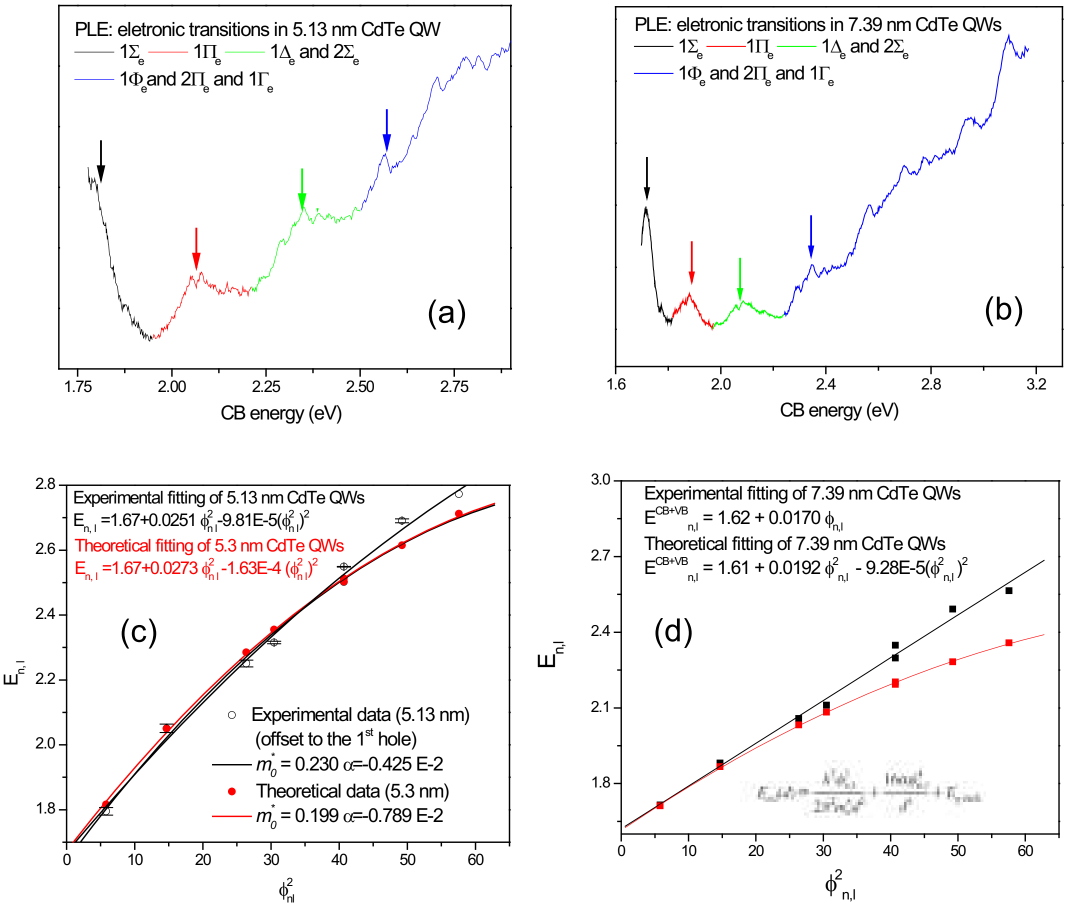

Figure 4.30 Comparisons of the experimentally resolved PLE of (a) 5.13 nm CdTe QWs and (b) 7.39 nm CdTe QWs. (c) Plots of experimental (black squares) and theoretical (red dots) CB-states energy of CdTe QWs of 5.13 nm at the point Γ vs $\varphi^2_{n,l}$. (d) Plots of experimental (black squares) and theoretical (red dots) CB+VB-states energy of CdTe QWs of 7.39 nm at the point Γ vs $\varphi^2_{n,l}$.

For 7.39-nm CdTe QW, the hole-level energy difference was not conveniently available to offset the CB-transition energy. Therefore, only the first two sets of CB-states transitions to

$1\Sigma_e$ and $1\Pi_e$ matched closely between the experimental and the theoretical results in Figure 4.30 (d). This indicates that the hole-level energy difference may be negligible in the first two sets of the CB-transitions. Large deviation began at the 3rd set transition that was indicated by a green arrow in Figure 4.30 (b).

Both m^*_e and α are diameter-dependent, as shown in Table 4.1. Effective mass (m^*_e) increases as the diameter decreases. This explains why experimental m^*_e for 5.13 nm CdTe is slightly larger than theoretical m^*_e. The isotropic non-parabolicity constant (α) also changes with diameter. The absolute α value increases as the diameter becomes larger. The major difference between experimental α and theoretical α was associated with the fitting curvature which was manly determined by the transition energies of higher CB-states.

Table 4.1 Diameter dependence of m^*_e and α from theoretical and experimental data.

$d_{calc.}$ (nm)	m_e^* (m_0)	α (eV nm^4)	d_{exp} (nm)	m_e^* ($m0$)	α (eV nm^4)
5.3	0.199	-0.804×10^{-2}	5.13 ± 0.68 nm	0.230	-0.442×10^{-2}
7.3	0.157	-1.65×10^{-2}	7.39 ± 0.51 nm	0.152	-1.33×10^{-2}

4.4 Conclusion

CdTe quantum wires (QWs) of 5.1 and 7.4 nm diameters were passivated with thiols, TOP, and zinc complexes, to partially eliminate surface trap sites. By manipulating two passivation strategies, significant CdTe QW PL quantum efficiency of 3% is obtained in strategy A, and 5-8 % in strategy B. Photoluminescence (PL) spectra demonstrate a strong band-gap emission with longer and shorter wavelength shoulders. Epifluorescence experiments also reveal the existence of shoulder emissions in a partial-wire image, but band-gap emission only in a whole-wire image. Multiple high-energy transitions in the photoluminescence excitation (PLE) spectra implicate highly passivated QW surfaces with resolved electronic transitions. By comparing the effective mass (m_e*) and isotropic nonparabolicity constant (α), the experimental results compare well to previously determined theoretical values. This ability to passivate the CdTe QW surface not only opens a new avenue for directly probing QW band structures, but also enhances the quantum efficiency for practical applications.

4.5 Experimental

4.5.1 Materials

Cadmium oxide (CdO, 99.99+%), Tellurium powder (Te, -5+50 mesh, 99.99%), trioctylphosphine (TOP, tech., 90%), trioctylphosphine oxide (TOPO, tech., 90%), diethyl zinc ($ZnEt_2$, min. 52.0 wt. %), were purchased from Aldrich and used as received except for TOPO, which was distilled before use. 2-propanol (99.5%, HPLC grade) from Aldrich and toluene from Sigma-Aldrich (CHROMASOLV®, for HPLC, ≥ 99.9%), were purged with dry N_2 for at least 1 h and stored under N_2 prior to use. *n*-Octadecylphosphonic acid (ODPA) and *n*-tetradecylphosphonic acid (TDPA) were purchased from PolyCarbon Industries and stored under N_2. Ethanethiol (97%) and zinc *neo*-decanoate (ZND, Zn 17.9-18.2%) were purchased from Alfa Aeaser and used as received. CdTe QWs were prepared by a literature method.[6]

4.5.2 Surface passivation and purification of CdTe QWs.

All synthetic procedures were conducted under dry N_2. N_2-purged toluene (≥ 20 mL) was transferred to a Schlenk flask containing a CdTe QWs-TOPO solution soon after the QW synthesis (~6 g). A continuous flow of N_2 was bubbled through the solution for at least 1h prior to transferring into a glove box. At this stage, no purification process was conducted.

An aliquot of the CdTe QW suspension (0.5 g, 8 μmol Cd, 2 μmol Te) prepared by the synthetic procedure above was transferred to a septum-capped vial, and the vial was removed from the glove box. A solution of ethanethiol (1 mL, 13 mmol) in a syringe was injected, and the vial was shaken vigorously a few times. After the injection, the CdTe QWs were gradually flocculated from the suspension. At this point, the CdTe QWs already showed weak photoluminescence (PL) peak(s) with a quantum yield around 0.1-0.5%, indicating the beginning of the ligand exchange process. In order to expedite the PL enhancement, the vial was placed 5-cm distance from a 100-W tungsten light bulb for photo-annealing. The process was usually conducted for 0.5-2 h. During this period most of the QWs settled to the bottom third of the vial as a cloudy suspension. After the photo-annealing, the thiolate-exchanged CdTe QWs shows stronger photoluminescence (PL) peak(s) with quantum yield around 0.5-1 %. For the completeness of passivation, the vial was allowed to stand on the bench top overnight.

After this period, most of the dark-black precipitate was settled at the bottom of the vial. The upper clear solution (yellow-to-colorless) was removed by syringe and discarded. The thiolate-exchanged CdTe QWs and residual solution were transferred into a glove box. The purification procedure was continued by centrifugation and addition of another portion of TOP-toluene stock solution (1 mL, 1-20 %, w/w) to the remaining QW suspension in the vial.

The vial was shaken vigorously a few time and allowed to stand on the shelf for 0.5-1 h until most of the black precipitates were settled to bottom third of the vial. The upper two-thirds of colorless supernatant was carefully removed by a pipette and the vial was refilled the TOP-solution (1 mL). The vial was again shaken vigorously a few times was allowed to stand on the shelf for 0.5-1 h until most of the black precipitates were settled to bottom third of the vial. After TOP-toluene purification process, the QWs were re-dispersed in TOP (1 mL, 90%). The vial was taken away from the glove box and put 5-cm under a 100-W incandescent lamp. A 100-W incandescent lamp provided a light source for photo-annealing, which was conducted on a bench top at room temperature. After photo-annealing for 0.5-1 h, the TOP-thiolate-exchanged CdTe QWs showed even stronger photoluminescence (PL) peak(s) with quantum yield over 5%.

The resulting TOP-thiolate-exchanged CdTe QWs were used for spectroscopic analysis on the same day to retain a high PL quantum yield. Dilution of the precipitate with TOP (90%, 10-20 mL) afforded a clear, pale yellowish brown dispersion of TOP-thiolate-exchanged CdTe QWs. The passivated CdTe QWs in TOP can be stored under N_2 (or in a glove box) for 10 months with PL quantum yield varying between 5-8%.

2.5.3 Zinc-complex adsorption of CdTe QWs

Zinc *neo*-decanoate (ZND) was used for zinc adsorption experiments. ZND (0.52 g, 1.5 mmol) was dissolved in N_2-purged toluene (17.9 g), affording a colorless zinc solution (81 mmol/kg). The concentration was expressed in molality (mmol/kg), which was ultimately converted to molarity (mol/L) by using the density of toluene (d = 0.87 g/mL, or 0.87 kg/L). The ZND stock solution was more commonly used for zinc passivation and zinc adsorption experiments by adding it directly into a purified TOP-thiolate-exchanged CdTe QW solution. ZND solution was delivered by weight (g) which was recorded by an electronic balance with a minimal increment of 0.001 g. The zinc concentration in the QW solution was calculated by the dilution factor of mass (g/g) and then converted to molarity (mol/L).

Diethylzinc ($ZnEt_2$) solution was prepared, stored, and used in a glove box due to its high flammability in air. Diethylzinc (0.297 g, 1.25 mmol) was delivered to N_2-purged TOP-toluene solution (12.7 g, 3.25 %, w/w), affording a colorless ZTT solution (97 mmol/kg). Diethylzinc formed smoke, indicating an oxidation process, even in a glove box. Therefore, the actual zinc concentration might be lower than the calculated value (97 mmol/kg). The ZTT solution was also delivered into as-made or TOP-thiolate-exchanged CdTe QW solution by weight. After the ZTT was added into QW solution in a cuvette, the capped cuvette was removed from the glove box and was ready for further photo-annealing and spectroscopic analyses.

4.5.4 Photo-annealing of CdTe QWs

In a generic process, incandescent light (tungsten bulb; 100 W) was used for photo-annealing. A cuvette or vial containing a CdTe QW solution was placed 5-cm under the 100-W bulb. During the process, observation of precipitation and gas formation (only in thiol solution) indicated changes of surface properties. QW flocculation was one of the purposes for photo-annealing, and the precipitation of the QW precipitates indicated solubility decreased due to a bundling. Gas formation in small bubbles also indicated surface-property change. Irradiation was conducted for 0.5-2 h.

4.5.5 Absorption spectroscopy

Most spectroscopic analyses of CdTe QWs were conducted in toluene, TOP-toluene solution (1-20 %, w/w), or TOP (90 %). A passivated CdTe QW suspension was first centrifuged in a bench-top centrifuge for 3-5 min to produce a black QW precipitate. The black precipitate was shaken and redispersed in the same mixture, followed by a subsequent centrifugation to remove excess ligands in the solution. This cycle was repeated 1-2 times with re-dispersion in the same mixture for the absorption measurement.

Absorption spectra were collected at room temperature using a Varian Cary 100 Bio UV-visible spectrophotometer. The sample absorbance was adjusted to 0.05-0.15 at 510 nm. In each

UV-vis spectroscopic analysis, the same background solution, toluene or a TOP or TOP-toluene solution, was used for the reference and sample. A baseline correction was also applied to account for cuvette absorption. TOP and TeTOP have a strong absorption bands below 350 nm and 450 nm, respectively, which appeared in the spectra if the TOP or TeTOP concentrations in the sample and reference cuvettes were imbalanced, or if the baseline was inadequately corrected. In addition, cuvettes in the fluorimeter holder should be placed to the same direction all the times

4.5.6 Photoluminescence (PL) and photoluminescence excitation (PLE) spectroscopies

Spectroscopic analysis of CdTe QWs were conducted in toluene, TOP-toluene (1-20 %, w/w), or TOP (90%). For each absorption spectrum, three sample cuvettes (quartz) of different concentrations and two blank cuvettes (quartz) of dispersion solution were prepared in the glove box. Two blank cuvettes were used for reference and one for the sample. The cuvette filling process was conducted under N_2 to avoid any oxidization to TOP and CdTe QWs.

A baseline correction of the dispersion solutions was applied to account for cuvette absorption. TOP has a very strong and sharp absorption band below 350 nm, which appeared in the spectra if the reference cuvettes were imbalanced or contained organic residues on the cuvette faces. Any possible contamination pathway, such as bare-hand handing or standing in dirty holder, would cause the misalignment for the baseline correction. Moreover, the solution amount was adjusted to fill 80-90 % of the maximum cuvette volume (4 mL or 3.5 g toluene). Lesser amount caused additional scattering which imbalanced the baseline.

1.5.8 Transmission electron microscopy (TEM)

For analysis of as-made and passivated CdTe QWs, an aliquot from the suspension of QWs (ca. 0.1 mL) was diluted into toluene (1 mL) in air. The mixture was shaken a few times and centrifuged in a bench-top centrifuge for 5 min. This gave a black precipitate and a nearly colorless supernatant. The supernatant was discarded, and the QW precipitate was re-diluted into toluene (1 mL). The mixture was shaken and then centrifuged as above. The supernatant was again discarded and the black QW precipitate was dispersed in toluene (1 mL) to yield a pale yellow dispersion for subsequent TEM analysis.

A drop of the appropriate CdTe QW dispersion was transferred onto a carbon-coated Cu grid (Ted Pella, PELCO® 300 Mesh Grids, product #: 1GC300). The solvent on the Cu grid was evaporated in the ambient atmosphere. This process was usually repeated twice to load enough CdSe NCAs onto the grid (concentration dependent). TEM images of CdTe QWs were collected using a JEOL 2000 FX microscope with an acceleration voltage of 200 kV. HRTEM was conducted on a JEOL-2100F using TEM grid with holey-carbon film (Ted Pella, Ultra-thin Carbon Film on Holey Carbon Support Film, 400 mesh, Copper, product #: 01824).

4.6 References

1. Lide, D. R. *Handbook of Chemistry and Physics*; 88th ed; CRC press: Boca Raton, 2007.
2. Yuhas, B.D.; Yang, P.; *J. Am. Chem. Soc.* **2009**, *13*1, 3756-3761.
3. Weintraub, B.; Wang, Z.L. *Angew. Chem. Int. Ed.* **2009**, *48*, 8981-8985.
4. Lim, Y.T.; Kim, S.; Nakayama, A.; Stott, N.E.; Bawendi, M.G.; Frangioni, J.V. *Mol. Imaging* **2003**, *2*, 50-64.
5. Michalet, X.; Pinaud, F.F.; Bentolila, L.A.; Tsay, J.M.; Doose, S.; Li, J.J.; Sundaresan, G.; Wu, A.M.; Gambhir, S.S.; Weiss, S. *Science*, **2005**, *307,* 538-544.
6. Sun, J.; Wang, L.W.; Buhro, W. E. *J. Am. Chem. Soc.* **2008**, *130*, 7997-8005.
7. Sun, J.; Buhro, W. E.; Wang, L.W.; Schrier, J. *Nano. Lett.* **2008**, *8*, 2913-2919.
8. Protasenko, V.V.; Hull, K.L.; Kuno, M. *Adv. Mater.*, **2005**, *17*, 2942-2949.
9. Hines, M. A.; Guyot-Sionnest, P. *J. Phys. Chem.* **1996**, *100*, 468-471.
10. Peng, A.; Schlamp, M.C.; Kadavanich, A.V.; Alivisatos, A. P. *J. Am. Chem. Soc.* **1997**, *119*, 7019-7029.
11. Bussian, D.A.; Crooker, S. A.; Yin, M.; Brynda, M.; Efros, A. L.; Klimov, V.I. *Nat. Mater.* **2009**, *8*, 35-40.
12. Tian, J.; Liu, R.; Zhao, Y.; Peng, Y.; Hong, X.; Xu, Q.; Zhao, S. *Nanotechnology*, **2010**, *21*, 305101.
13. Kim, S.; Sim, W.; Seo, H.; Bae, J.H.; Sung, J.; Choi, S.H.; Moon, W.K.; Lee, G.; Lee, B.; Kim, S.-W. **2009**, *Chem. Commun. 1267-1269.*

14. Akamatsu, K.; Tsuruoka, T.; Nawafune, H. *J. Am. Chem. Soc.* **2005**, *127*, 1634-1635.

15. Kitauchi, Y.; Kobayashi, Y.; Tomioka, K.; Hara, S.; Hiruma, K.; Fukui, T.; Motohisa, J. *Nano. Lett.* **2010**, *10*, 1699-1703.

16. Li, J; Bao, D.; Hong, X.; Li, D.; Li, J.; Bai, Y.; Li, T. *Colloids and Surface A: Physicochem. Eng. Aspect* **2005**, *257-258*, 267-271.

17. Morrison, S.R. *The Chemical and physics of Surface*; 2nd ed; Plenum press: New York, 1990.

18. Spanhel, L.; Haase, M.; Weller, H.; Henglein, A. *J. Am. Chem. Soc.* **1987**, *109*, 5649-5655.

19. Wang, F.; Buhro, W.E. *Small*, **2010**, *6*, 573-581.

20. Protasenko, V.V.; Hull, K.L.; Kuno, M. *Adv. Mater.* **2005,** *17*, 2942-2949.

21. Akopian, N.; Patriarche, G.; Liu, L.; Harmand, J.-C.; Zwiller, V. *Nano. Lett.* **2010**, *10*, 1198-1201.

22. Zhang, S.B.; Wei, S.-H. *Phys. Rev. B* **2000**, *62*, 6944-6947.

23. Datta, S.; Saha-Dasgupta, T.; Sarma. D.D. *J. Phys.: Condens. Mater.* **2008**, *20*, 445217.

24. Gorkavenko, T.V.; Zubkova, S.M.; Makara, V.A.; Rusina, L.N. *Semiconductors*, **2007**, *41*, 886-896.

25. Golovach, V.M.; Zegrya, G.G.; Makhanets, A.M.; Pronishin, I.V.; Tkach, N.V. *Semiconductors*, **1999**, *33*, 564-568.

26. Wang, X.; Ren, X.; Kahen, K.; Hahn, M.A.; Rajeswaran, M.; Maccagnano-Zacher, S.; Silcox, J.; Cragg, G.E.; Efros, A.L.; Krauss, T.D. *Nature*, **2009**, *459*, 686-689.

27. Xia, Y.; Zhang, T.; Diao, X.; Zhu, C. *Chem. Lett.* **2007**, *36*, 242-243.

28. Shi, L.; Hernandez, B.; Selke, M. *J. Am. Chem. Soc.* **2006**, *128*, 6278-6279.

29. Law, W.C.; Yong, K.T.; Roy, I.; Ding, H.; Hu, R.; Zhao, W.; Prasad, P.N. *Small* **2009**, *11*, 1302-1310.

30. Wang, X.-D.; Chen, X.; Xie, Z.-X.; Wang, X.-R. *Angew. Chem. Int. Ed.* **2008**, *47*, 7450-7453.

31. Zhang, H.; Wang, D.; Yang, B.; Möhwald, H. *J. Am. Chem. Soc.* **2006**, *128*, 10171-10180.

32. Wuister, S.F.; Swart, I.; van Driel, F.; Hickey, S.G.; de mello Donegá, C. *Nano. Lett.* **2003**, *3*, 503-507.

33. Rogach, A.L.; Franzl, T.; Klar, T.A.; Feldmann, J.; Gaponik, N.; Lesnyak, V.; Shavel, A.; Eychmüller, Rakoich, Y.P.; Donega, J.F. *J. Phys. Chem. C* **2007**, *111*, 14628-14637.

34. Koole, R.; Schapotschnikow, P.; de Mello Donegá, C.; Vlugt, T.J.H.; Meijerink, A. *ACS Nano* **2008**, *2*, 1703-1714.

35. Osovsky, R.; Kloper, V.; Kolny-Olesiak, J.; Sashchiuk, A.; Lifshitz, E. *J. Phys. Chem. C* **2007**, *111*, 10841-10847.

36. Zhong, H.; Nagy, M.; Jones, M.; Scholes, G.D. *J. Phys. Chem. C* **2009**, *113*, 10465-10470.